MODULATION SPECTROSCOPY OF SEMICONDUCTOR MICROSTRUCTURES

by

Wojciech Krystek

A dissertation submitted to the Graduate Faculty in Physics in partial fulfillment of the requirements for the degree of Doctor of Philosophy, The City University of New York

1996

This manuscript has been read and accepted for the Graduate Faculty in Physics in satisfaction of the dissertation requirement for the degree of Doctor of Philosophy.

SEPT. 4, 1996
Date

Fred H Pollak
Distinguish Professor Fred H. Pollak
Chair of Examining Committee

Sept 4, 1996
Date

Joseph B. Krieger
Professor Joseph B. Krieger
Executive Officer

Professor Godfrey Gumbs

Professor Ken Miyano

Professor Dragana Popovic

Professor Maria Tamargo

Supervisory Committee

THE CITY UNIVERSITY OF NEW YORK

Abstract

MODULATION SPECTROSCOPY OF SEMICONDUCTOR MICROSTRUCTURES

by

Wojciech Krystek

Advisor: Distinguished Professor Fred H. Pollak

With modern thin film growth techniques, such as molecular beam epitaxy, one can design new, complex semiconductor microstructures with almost arbitrary potential profiles. The investigation of the properties of these artificially structured crystals is of considerable interest from both fundamental and applied perspectives. In this thesis we have studied several very important semiconductor microstructures with photoreflectance (PR), contactless electroreflectance (CER) and piezoreflectance modulation spectroscopy techniques.

We have measured the temperature dependence of the direct gaps of ZnSe and $Zn_{0.56}Cd_{0.44}Se$ in the temperature range $25K < T < 400K$ using CER. The quantities that describe the temperature dependence of the energy (including thermal expansion effects) and broadening function of the band gaps were evaluated. Comparison has been made with corresponding parameters of several other II-VI and III-V materials.

Using CER at 300K we have characterized the potential profile of a pseudomorphic 0.98 μm InGaAs/GaAs/GaAlAs graded index of refraction separate confinement heterostructure laser. Signals were detected from all three relevant portions of the sample. To identify spectral features we have performed computer calculation

based on the envelope function approximation, including the effects of strain and electric field. From the period of the observed Franz-Keldysh oscillations from the graded GaAlAs region we have evaluated directly the built-in electric field in the structure.

We have presented the contactless determination of the time constants of the equivalent circuits of both the GaAs collector and GaAlAs emitter portions of a GaAs/GaAlAs heterojunction bipolar transistor (HBT) structure using the modulation frequency dependence ($2\ \text{Hz} < \Omega_m < 100\ \text{kHz}$) of the in-phase and quadrature PR signals. An analysis of the collector time constant has revealed that the recombination mechanism in the collector-base region is dominated by the hole current and is due to midgap trap states.

We have also presented new results on the illumination dependence of the electric fields deduced from the PR spectra of this GaAs/GaAlAs HBT structure. We have found that doping levels in the emitter/base and collector/base regions can be obtained from the illumination dependence of the observed fields, while the fields themselves can be used to evaluate variations in the doping levels.

Dedication

To My Parents

Acknowledgements

I wish to express my greatest appreciation to my thesis advisor, Distinguished Professor Fred H. Pollak. Without his guidance, support, and encouragement, this dissertation would have been impossible. His enthusiasm and creativity in exploring and understanding physics, its theoretical foundation as well as experimental part, were an inspiration. He has introduced me to the scientific community and provided me with the opportunity to participate in its different endeavors. His kind assistance in all aspects of my studies and his constant interest in my progress has given me more than one could possibly expect from a mentor.

I would like to express my deep gratitude to the other members of my thesis advisory committee, Professor Godfrey Gumbs of Hunter College, Professor Ken Miyano of Brooklyn College, Professor Dragana Popovic of NHMFL of Florida State University, and Professor Maria Tamargo of City College, for agreeing to serve on my committee, for their careful reading of this manuscript and helpful advice. I want to especially thank Professor Godfrey Gumbs, who was our collaborator in part of the work on this thesis, for his many, valuable discussions with me. I also want to thank Professor Maria Tamargo, who grew II-VI epilayers used in our studies, not only for very good quality samples and showing me her laboratory, but also for her encouragement and friendliness.

I am deeply indebted to my colleagues at Brooklyn College for their support, encouragement, and friendship. In particular I want to thank Dr. Dong Yan, who taught me many aspects of experimental physics and provided me with a lot of help during the

years of my graduate study.

Special thanks are due to Mr. Louis Tundis of the Central Machine Shop of Brooklyn College for his excellent assistance in making the components of the experimental setup, which is essential for successful experiments.

I always greatly appreciate the effort of my parents who encouraged me to study from my earliest years.

TABLE OF CONTENTS

ABBREVIATIONS

1D	one-dimensional
2D	two-dimensional
3D	three-dimensional
BZ	Brillouin zone
CER	contactless electroreflectance
EER	electrolyte electroreflectance
EM	electromodulation
ER	electroreflectance
FKOs	Franz-Keldysh Oscillations
FDGP	first-derivative of a Gaussian profile
FDLP	first-derivative of a Lorentzian profile
GRINSCH	graded index of refraction separate confinement heterostructure
HBT	heterojunction bipolar transistor
HH	heavy-hole
HJ	heterojunction
LH	light-hole
LMF	low modulation field
LO	longitudinal optical
MBE	molecular beam epitaxy
MOCVD	metal-organic chemical vapor deposition
MQW	multiple quantum well
PR	photoreflectance
PzR	piezoreflectance
QW	quantum well
SCR	space-charge region
SL	superlattices
SQW	single quantum well
SRH	Shockley-Read-Hall

LIST OF TABLES

LIST OF FIGURES

Chapter 1. INTRODUCTION

With modern thin film growth techniques such as molecular beam epitaxy (MBE) and metal-organic chemical vapor deposition (MOCVD), one can design new, complex semiconductor microstructures with almost arbitrary potential profiles. These methods make it possible to control materials composition, layer thickness, doping levels, etc. on an atomic scale. Heterojunctions (HJs), either lattice-matched or strained layer, can be used to construct configurations such as quantum wells (QWs), multiple quantum wells (MQWs), superlattices (SLs), etc. Also built-in electric fields can be produced by means of appropriate doping of either homo- or HJs. The reduced dimensionality in such systems alters the behavior of electrons and holes at the quantum mechanical level, bringing about a large number of phenomena that are not available in the natural bulk semiconductors. These new semiconductor microstructures not only display a wide variety of interesting new transport and optical phenomena but also form the basis of important novel semiconductor devices such as QW lasers, heterojunction bipolar transistors (HBTs), high electron mobility transistors, etc.

The investigation of the properties of these artificially structured crystals is of considerable interest from both fundamental and applied perspectives. Modulation spectroscopy is one of the most powerful methods to study the optical properties related to the quantum effects and potential profiles in these microstructures. Modulation spectroscopy is an analog method for taking the derivative of the optical spectrum of a material by the periodic modification of the measurement conditions. This procedure

gives rise to sharp, differential-like spectra in the region of interband (intersubband) transitions. One of the most important advantages of modulation spectroscopy is the ability to perform detailed lineshape fits to extract important parameters such as interband (intersubband) energies, broadening parameters, etc.

. A particularly useful form of modulation spectroscopy is electromodulation (EM) since it is sensitive to surface/interface electric fields and can be performed in contactless modes that require no special mounting of the sample. Under certain conditions EM can display an oscillatory behavior above the band gap called Franz-Keldysh oscillations (FKOs), whose period is a direct measure of the built-in electric field. In addition EM can be performed over a wide temperature region $10K < T < 500K$.

Using this method we have investigated three different semiconductor microstructures. We have measured temperature dependence of energy gaps and broadening parameters for ZnCdSe and ZnSe epilayers which are promising materials for blue-green semiconductor lasers. We have fit these experimental results to Varshni and Bose-Einstein type expressions. We have studied the quantum transitions from a pseudomorphic InGaAs/GaAs/GaAlAs symmetric QW structure with a graded index of refraction separate confinement heterostructure (GRINSCH) configuration, consisting of a small InGaAs well inside a larger GaAs well. Even at 300 K we have observed rich spectra originating in the various regions of the sample. In order to identify the origins of the various spectral features we have performed a theoretical computer calculation based on the envelope function approximation, including the effects of strain and electric field. Also, we have determined the time constants of the equivalent circuits of both the

GaAs collector and GaAlAs emitter portions a GaAs/GaAlAs HBT. We have investigated the PR spectra from a GaAs/GaAlAs HBT structure as a function of the intensity of both the probe and pump beams and we have presented new results on the illumination dependence of the electric fields deduced from the PR spectra.

This thesis consists of six chapters. In Chapter 2 the principles and techniques of modulation spectroscopy are discussed. We start with the connection between optical properties of semiconductors and fundamental quantum mechanics, consider lineshape and functional form of dielectric function, and finally describe instrumentation. In Chapter 3 we report studies of temperature dependence of energy gaps and broadening parameters of ZnCdSe and ZnSe epilayers. First we discuss the theoretical background of this temperature dependence, including Bose-Einstein theory and Varshni formulation and then we provide experimental details and results. In Chapter 4 we present work on 0.98μm InGaAs/GaAs/GaAlAs GRINSCH laser structure. In addition to experimental details and results we review some theoretical aspects of QW structures such as envelope function calculation of quantum levels in these structures, strain effects, and Quantum Confined Stark Effect. Investigation of GaAs/GaAlAs HBT is described in Chapter 5. The first part deals with Equivalent Circuit Analysis and in the second one we report studies of the illumination dependence of the electric fields, in GaAs collector and GaAlAs emitter regions, deduced from the PR spectra and we discuss a significance of a photovoltaic contribution to the PR signals. A summary and conclusions are given in Chapter 6.

Chapter 2. BACKGROUND OF MODULATION SPECTROSCOPY

Since its inception in 1964 modulation spectroscopy has proven to be a powerful experimental technique for studying and characterizing the properties of bulk semiconductors, reduced dimensional systems (surfaces, interfaces, heterostructures, etc.), actual device structures and growth/processing. The basic idea of modulation spectroscopy is a very general principle of experimental physics. Instead of directly measuring an optical spectrum, the derivative with respect to some parameter is evaluated. This can easily be accomplished by periodically modulating some parameter applied to the sample ("external" modulation) such as electric field (EM), heat pulse (thermomodulation), or stress (piezomodulation). The change may also occur in the measuring system itself ("internal" modulation), e.g., the wavelength or polarization conditions can be modulated or the sample reflectance (transmittance) can be compared to a reference sample. The observed normalized changes are usually small so that the difference signals are closely related to a derivative of the absolute spectrum with respect to the modifying parameter. The derivative nature of modulation spectra suppresses uninteresting background effects and often enhances weak features that may not have been seen in the absolute spectra. Because of this derivative-like nature a large number of sharp spectral features can be observed, even at room temperature. In addition, "external" modulation is an ac method which represents the optical response of the system to the modulating parameter. Thus, there is also important information in other modulating variables such as phase, modulation frequency, modulation amplitude, pump

wavelength, etc.

As an example of the power of modulation spectroscopy, shown in Figure 1 is a comparison of the reflectivity (R) and electric-field modulated [electroreflectance (ER)] spectra of bulk GaAs at 300K [1]. While the reflectivity is characterized by broad features, the ER trace has zero as a base and is dominated by a series of very sharp, derivative-like features corresponding to specific transitions in the Brillouin zone (BZ).

The ability to perform a lineshape fit is one of the great advantages of modulation spectroscopy. Since for the modulated signal the features are localized in photon energy it is possible to account for the lineshapes to yield accurate values of energies and broadening parameters of interband transitions. For example, it is possible to determine the energies of the E_0, $E_0+\Delta_0$, E_1 and $E_1+\Delta_1$ peaks in Figure 1 to within a few meV, even at room temperature. Thus, the effects of static external perturbations such as electric and magnetic fields, temperature, hydrostatic pressure, uniaxial stress, composition, etc. can be conveniently studied.

Research efforts in the first decade were focused on the properties of bulk semiconductors. The results have been reviewed by Cardona [2,3], Hamakawa and Nishino [4], Aspnes [5] and Pollak [1]. One can also find valuable references in Vol. 9 of Semiconductor and Semimetals, eds. R. L. Willardson and A. C. Beer (Academic, New York 1972) and in the Proceedings of the First International Conference on Modulation Spectroscopy, published as Vol. 37 of Surface Science (1973).

In the 1980's modulation spectroscopy enjoyed a renaissance. It was shown that the same advantages long exploited for bulk studies also were evident in the artificial

semiconductor microstructures fabricated by modern thin film methods such as MBE or MOCVD [6-10]. The important work of Glembocki *et al.* [9,10] demonstrated that a

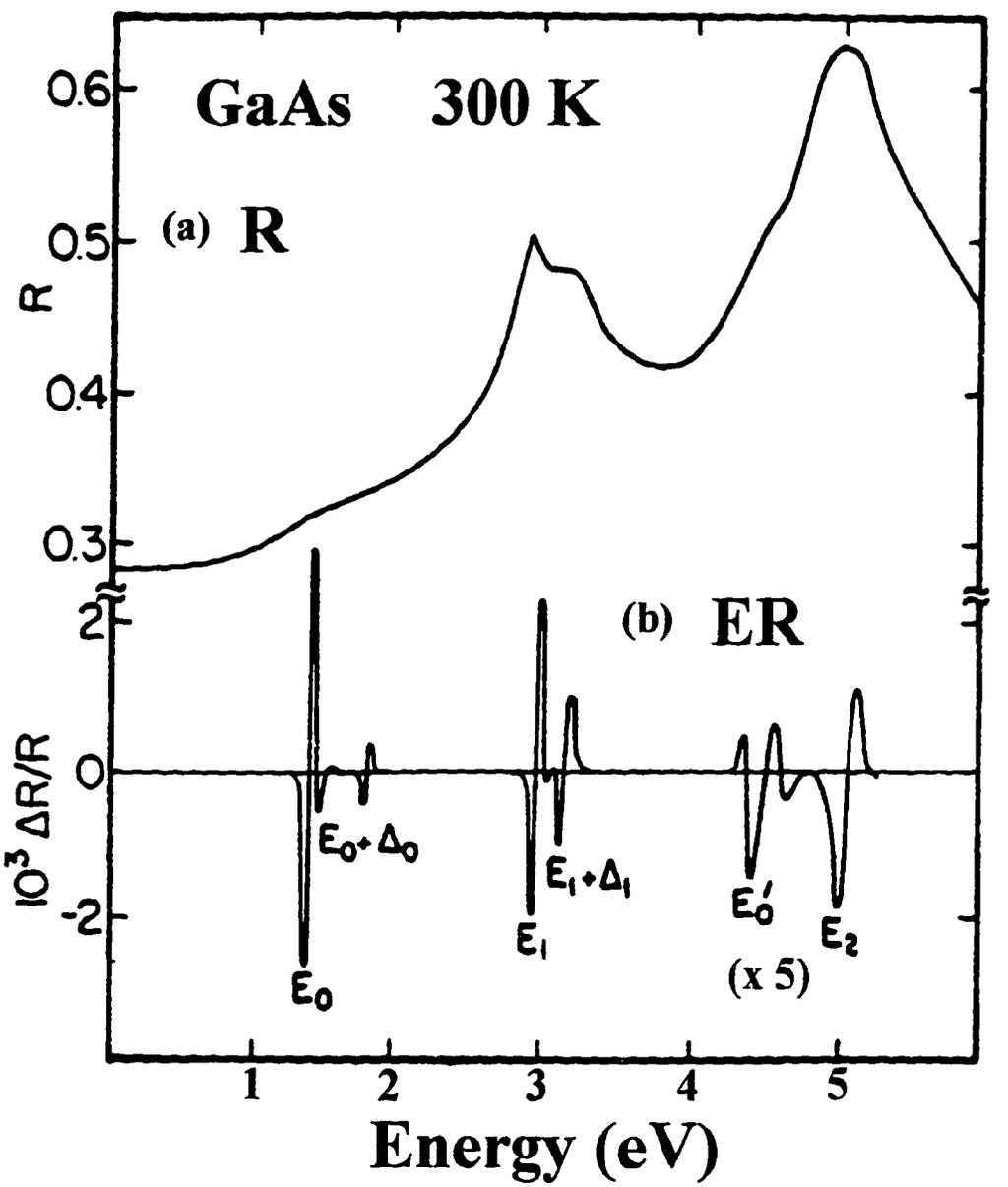

Figure 1. Comparison of room temperature reflectivity and electric-field modulated reflectivity (electroreflectance) of GaAs [1].

large number of intersubband transitions in a MQW could be observed at room temperature using the contactless EM method of photoreflectance (PR). Thus, the rich modulated spectra from microstructures could be used to probe the "band structure" of reduced dimensional systems just as this optical method was employed for bulk material.

These advances have stimulated a considerable amount of activity in experimental and theoretical areas as well as the development of new instrumentation, particularly contactless modes. Not only is work being carried out on the fundamental aspects of a large variety of reduced dimensional systems such as single quantum wells (SQWs), MQWs, SLs, HJs and surfaces/interfaces, but the properties of bulk material again are being revisited. The effects of various external perturbations also are being explored.

In order to present the mechanism of modulation spectroscopy in detail, below we discuss the connection between optical properties of semiconductors and fundamental quantum mechanics.

2.1 Dielectric function

2.1.1 Transition probability

The effect of a electromagnetic field on the electronic states in crystal can be described by a standard quantum mechanical formalism. The kinetic energy of an electron in the presence of such a field is given by [11]:

$$\frac{1}{2m_0}(\mathbf{P}+\frac{e\mathbf{A}}{c})^2 \qquad (1)$$

where m_0 is the free electron mass, $\mathbf{P}$ is the momentum, e is the electron charge, and

A is the vector potential associated with the photon (electromagnetic field).

We can rewrite this equation as follows:

$$\frac{1}{2m_0}\mathbf{P}^2+\frac{e}{2m_0c}\mathbf{A}\cdot\mathbf{p}+\frac{e}{2m_0c}\mathbf{p}\cdot\mathbf{A}+\frac{e^2}{c^2}\mathbf{A}^2 \qquad (2)$$

Since we do not discuss here non-linear optical effects we can neglect the term in $\mathbf{A}^2$. The interaction Hamiltonian of an electron and photon is given by:

$$H_{e\text{-}p}=\frac{e}{m_0c}\mathbf{A}\cdot\mathbf{P} \qquad (3)$$

$H_{e\text{-}p}$ can be treated as a time dependent perturbation on the electronic states of the crystal. This time dependent term is responsible for electron transitions between bands.

The probability of a transition per unit time between initial ($|i>$) and final ($|f>$) states is:

$$P_{i\to f}=\frac{2\pi}{\hbar}|<f|H_{e\text{-}p}|i>|^2\delta(E_f-E_i\mp\hbar\omega) \qquad (4)$$

where E_i and E_f are the energies of the initial and final states, respectively.
The perturbation $H_{e\text{-}p}$ can induce transitions with either absorption (minus sign) or emission (plus sign) of the photon. The probability of transition $P_{i\to f}$ between valence band Ψ_{v,k_i} and conduction band Ψ_{c,k_f} induced by the radiation field $A_0\hat{e}e^{i(k\cdot r-\omega t)}+c.c.$ can then be expressed as:

$$P_{i\to f}=\frac{2\pi}{\hbar}\left(\frac{eA_0}{m_0c}\right)^2|<\Psi_{c,k_f}|e^{ikr}\hat{\epsilon}\cdot\mathbf{p}|\Psi_{v,k_i}>|^2\delta(E_f-E_i-\hbar\omega)+c.c. \quad (5)$$

where $\hat{\epsilon}$ is the polarization vector in the direction of electric field, $\mathbf{k}$ is the wave vector and c.c. is the complex conjugate of the previous term. The matrix $<\Psi_{c,k_f}|e^{ikr}\hat{\epsilon}\cdot\mathbf{p}|\Psi_{v,k_i}>$ is equal zero unless:

$$\mathbf{k}_f=\mathbf{k}_i+\mathbf{k} \quad (6)$$

The range of variation of $\mathbf{k}_i$ (or $\mathbf{k}_f$) is π/a_d with lattice constant, a_d, usually of the order of a few angstroms. For typical photon the wavelength is of the order of 10^4Å, so its momentum $k=2\pi/10^4$ Å^{-1}. Therefore $k\ll k_i$ (or k_f) and only the "vertical" transitions are possible:

$$k_f\approx k_i \quad (7)$$

Equation (5) can be written as:

$$P_{i\to f}=\frac{2\pi}{\hbar}\left(\frac{eA_0}{m_0c}\right)^2|\hat{\epsilon}\cdot\mathbf{M}_{cv}(k)|^2\delta(E_f-E_i-\hbar\omega) \quad (8)$$

where

$$\hat{\epsilon}\cdot\mathbf{M}_{cv}(k)=<\Psi_{c,k_f}|e^{ikr}\hat{\epsilon}\cdot\mathbf{p}|\Psi_{v,k_i}>=\hat{\epsilon}\cdot\int_{\text{crystal volume}}\Psi_c(k,r)(-i\hbar\nabla)\Psi_v(k,r)d^lr \quad (9)$$

where l is the dimension ($l=1$, 2, or 3).

Finally to obtain the number of transitions $W(\hbar\omega)$ per unit time per unit volume one has to sum Eq.(8) over all possible states in the unit volume:

$$W(\hbar\omega)=\frac{2\pi}{\hbar}\left(\frac{eA_0}{m_0c}\right)^2\sum_{v,c}\int_{BZ}\frac{2d^lk}{(2\pi)^l}|\hat{\epsilon}\cdot\mathbf{M}_{cv}(k)|^2\delta(E_f-E_i-\hbar\omega) \quad (10)$$

2.1.2 Optical constants

The fundamental quantity which describes the optical response of the material is the complex dielectric function:

$$\varepsilon(\omega)=\varepsilon_1(\omega)+i\varepsilon_2(\omega) \tag{11}$$

Alternatively, one can use the concept of the complex index of refraction:

$$N(\omega)=n(\omega)+i\kappa(\omega) \tag{12}$$

where n is the real refraction index and κ is known as the extinction coefficient. The quantities ε and N are connected by the relation:

$$\varepsilon=N^2 \tag{13}$$

which can be rewritten separately for real and imaginary parts:

$$\varepsilon_1=n^2-\kappa^2 \tag{14}$$

$$\varepsilon_2=2n\kappa \tag{15}$$

The absorption coefficient α can be expressed in terms of above quantities as follows:

$$\alpha=2\kappa\frac{\omega}{c}=\frac{\omega}{nc}\varepsilon_2 \tag{16}$$

The average energy density , u, in a medium of a radiation field, described by the vector potential **A** is given by:

$$u=\frac{n^2A_0^2\omega^2}{2\pi c^2} \tag{17}$$

The absorption coefficient is defined as the energy absorbed per unit time per unit

volume divided by the energy flux:

$$\alpha(\omega)=\frac{\hbar\omega W(\omega)}{uc/n} \tag{18}$$

Thus we have the absorption coefficient for vertical transitions:

$$\alpha(\omega)=\frac{4\pi^2e^2}{ncm_0^2\omega}\sum_{v,c}\int_{BZ}\frac{2d^lk}{(2\pi)^l}|\hat{\epsilon}\cdot\mathbf{M}_{cv}(k)|^2\delta(E_f-E_i-\hbar\omega) \tag{19}$$

And using Eq.(16) we can express the quantity ε_2 as follows:

$$\varepsilon_2(\omega)=\frac{4\pi^2e^2}{m_0^2\omega^2}\sum_{v,c}\int_{BZ}\frac{2d^lk}{(2\pi)^l}|\hat{\epsilon}\cdot\mathbf{M}_{cv}(k)|^2\delta(E_f-E_i-\hbar\omega) \tag{20}$$

Having $\varepsilon_2(\omega)$, the expression for $\varepsilon_1(\omega)$ can be obtained by Kramers-Kronig relationships:

$$\varepsilon_1(\omega)=1+\frac{2}{\pi}P\int_0^\infty\omega'\varepsilon_2(\omega')\frac{1}{(\omega')^2-\omega^2}d\omega' \tag{21}$$

$$\varepsilon_2(\omega)=-\frac{2\omega}{\pi}P\int_0^\infty\frac{\varepsilon_1(\omega')}{(\omega')^2-\omega^2}d\omega' \tag{22}$$

where P indicates the principal part.

In many cases the matrix element $|\hat{\epsilon}\cdot\mathbf{M}_{cv}(k)|^2$ is only a weak function of $\mathbf{k}$ and we can remove it from the integral:

$$\varepsilon_2(\omega)=\frac{4\pi^2e^2}{m_0^2\omega^2}\sum_{v,c}|\hat{\epsilon}\cdot\mathbf{M}_{cv}(k)|^2\int_{BZ}\frac{2d^lk}{(2\pi)^l}\delta(E_f-E_i-\hbar\omega) \tag{23}$$

If we define interband joint density of states as:

$$J_{cv}(\omega)=\int_{BZ}\frac{2d^lk}{(2\pi)^l}\delta(E_f-E_i-\hbar\omega) \tag{24}$$

then $\varepsilon_2(\omega)$ can be written as:

$$\varepsilon_2(\omega)=\frac{4\pi^2e^2}{m_0^2\omega^2}\sum_{v,c}|\hat{\epsilon}\cdot\mathbf{M}_{cv}(k)|^2J_{cv} \tag{25}$$

For a three-dimensional (3D) case we can rewrite J_{cv} as:

$$J_{cv}(E)=\frac{2}{(2\pi)^3}\int_E\frac{dS}{|\nabla_k[E_c(k)-E_v(k)]|} \tag{26}$$

where dS represents an element of surface in **k** space on the surface defined by

$$E_c(k)-E_v(k)=E \tag{27}$$

The joint density of states has singularities when:

$$\nabla_k[E_c(k)-E_v(k)]=0 \tag{28}$$

These are called van Hove singularities and they are responsible for the structure in ε_2 and the optical spectra of semiconductors. Equation (28) is satisfied when:

$$\nabla_kE_c(k)=\nabla_kE_v(k)\equiv 0 \tag{29}$$

or

$$\nabla_kE_c(k)\equiv\nabla_kE_v(k)\neq 0 \tag{30}$$

Eq.(29) occurs at high symmetry points. For Eq.(30) bands are parallel and singularities are "accidental".

For the critical points defined by Eq.(29) we can usually replace the actual complicated variation $E_{cv}(k)$ $[=E_c(k)-E_v(k)]$ with a simple, local, parabolic form:

$$E_{cv}(k)=E_g+\frac{\hbar^2}{2}\left(\frac{k_x^2}{\mu_{xx}}+\frac{k_y^2}{\mu_{yy}}+\frac{k_z^2}{\mu_{zz}}\right) \tag{31}$$

Thus the band structure is represented locally by four parameters: the energy gap E_g, and the three components of the effective, reduced mass tensor μ_{xx}, μ_{yy}, and μ_{zz}.

Performing the calculation explicitly for one, two, or three dimensions, and introducing the broadening parameter Γ, $\varepsilon_2(E,\Gamma)$ can be obtained. For example, for critical point M_0:

$$\varepsilon_2(E,\Gamma) \sim \begin{cases} \frac{1}{E^2}|\hat{\epsilon}\cdot\mathbf{M}_{cv}|^2(E_g-E+i\Gamma)^{-\frac{1}{2}} & \text{1D critical point} \\ \frac{1}{E^2}|\hat{\epsilon}\cdot\mathbf{M}_{cv}|^2\ln(E_g-E+i\Gamma) & \text{2D critical point} \\ \frac{1}{E^2}|\hat{\epsilon}\cdot\mathbf{M}_{cv}|^2(E_g-E+i\Gamma)^{\frac{1}{2}} & \text{3D critical point} \end{cases} \tag{32}$$

2.1.3 Modulation spectroscopy

Differential changes in the reflectivity can be related to the perturbation of the complex dielectric function [$\varepsilon(=\varepsilon_1+i\varepsilon_2)$] expressed as [2,3,5]:

$$\Delta R/R = a(\varepsilon_1,\varepsilon_2)\Delta\varepsilon_1+b(\varepsilon_1,\varepsilon_2)\Delta\varepsilon_2 \tag{33}$$

where a and b are the Seraphin coefficients, related to the unperturbed dielectric function, and $\Delta\varepsilon_1$ and $\Delta\varepsilon_2$ are the changes in the complex dielectric function due to the perturbation. The Seraphin coefficients a and b can be written as:

$$a=\frac{1}{R}\frac{\partial R}{\partial \varepsilon_1}; \quad b=\frac{1}{R}\frac{\partial R}{\partial \varepsilon_2} \tag{34}$$

Near the fundamental gap of bulk materials, $b \approx 0$ [5], so that $\Delta R/R \approx a\Delta\varepsilon_1$ is the only significant term. However, in multilayer structures interference effects are important so that the Seraphin coefficients are modified, and both $\Delta\varepsilon_1$ and $\Delta\varepsilon_2$ may have to be considered. The quantities $\Delta\varepsilon_1$ and $\Delta\varepsilon_2$ are related by a Kramers-Kronig inversion. The functional form of $\Delta\varepsilon_1$ and $\Delta\varepsilon_2$ can be calculated for a given perturbation provided that the dielectric function and critical point are known.

2.2 Lineshape Considerations

2.2.1 Electromodulation

EM is a particularly useful form of modulation spectroscopy since it often yields the sharpest structure and is sensitive to surface or interface electric fields. It is also the most complex form since, in certain cases (bulk materials, SLs), the perturbation can destroy the translational symmetry of the material.

EM can be classified into two categories, i.e., low-, and high-field regimes depending on the relative strengths of certain characteristic energies [4,5]. In the first range $|\hbar\theta| \leq \Gamma$, where Γ is the broadening parameter and $\hbar\theta$ is the electro-optic energy given by:

$$(\hbar\theta)^3 = q^2\hbar^2F^2/2\mu_{\parallel} \tag{35}$$

In Eq.(35), **F** is the electric field and $\mu_{\parallel}$ is the reduced interband mass in the direction of the field. In the high-field case $|\hbar\theta| \gtrsim \Gamma$, but $qFa_d << E_g$, where a_d is the lattice

constant (or an appropriate periodic length in microstructures) and E_g is the band gap. In this situation, the band structure is unchanged. For the very high-field the electro-optic energy is much greater than the broadening but $eFa_d \sim E_g$ and the Stark shifts are produced [12]. We are not interested in such a very high-field regime and it will be ignored in the following discussions.

2.2.1.1 Low Field Regime

In the case of bulk materials and SLs, EM can destroy the translational symmetry of the material, and hence, can accelerate unbound electrons and/or holes.

The time dependent Schrödinger equation for an electron with mass m in a crystal in the presence of a uniform electric field F can be written as [5]:

$$(H_0 + e\mathbf{F}\cdot\mathbf{r})\psi = i\hbar\frac{\partial\psi}{\partial t} \tag{36}$$

where the crystal Hamiltonian H_0, with crystal potential V(r), is:

$$H_0 = \frac{p^2}{2m_0} + V(r) \tag{37}$$

The time evolution of the wave function, which at the time t=0 is the Bloch function $\psi_n(k_0,r)$ is given by:

$$\psi_n(k,r,t) = \exp[-i\frac{(H_0 + e\mathbf{F}\cdot\mathbf{r})t}{\hbar}]\psi_n(k_0,r) \tag{38}$$

The main effect of the electric field on a periodic system is to change the wave vector from **k** to $\mathbf{k}-e\mathbf{F}t/\hbar$. As a result, states with **k** vector along the field direction are mixed. The solution of the time dependent Schrödinger equation can be approximately

written as:

$$\psi_n(\mathbf{k},\mathbf{r}) = \exp[-\frac{i}{\hbar}\int E_n(\mathbf{k})dt]\psi_n(\mathbf{k},\mathbf{r}) \tag{39}$$

where $\mathbf{k}(t)$ is given by:

$$\mathbf{k}(t)=\mathbf{k}_0-\frac{e\mathbf{F}t}{\hbar} \tag{40}$$

Now we can determine the optical constants in the presence of an electric field, using Eq.(23). By taking into account the time dependence of $\mathbf{k}$, and the broadening parameter Γ, for the imaginary part of the dielectric function we obtain:

$$\varepsilon_2(\omega)=\frac{4\pi^2e^2}{m_0^2\omega^2}\sum_{v,c}\int_{BZ}\frac{2d^3k}{(2\pi)^3}|\hat{\epsilon}\cdot\mathbf{M}_{cv}(\mathbf{k})|^2\delta[E_{cv}(\mathbf{k}-\frac{e\mathbf{F}t}{\hbar})+i\Gamma-\hbar\omega] \tag{41}$$

This can be rewritten as [5]:

$$\varepsilon_2(\omega)=\frac{4\pi e^2}{m_0^2\omega^2}\sum_{v,c}\int_{BZ}\frac{2d^3k}{(2\pi)^3}|\hat{\epsilon}\cdot\mathbf{M}_{cv}(\mathbf{k})|^2\int dt\ \exp\{-i[E_{cv}(\mathbf{k}-\frac{e\mathbf{F}t}{\hbar})-i\Gamma+\hbar\omega]t\} \tag{42}$$

Since we consider here the low field regime, we can expand $E_{cv}(\mathbf{k})$ in terms of the field and retain terms only to second-order:

$$\varepsilon_2(\omega)=\frac{4\pi e^2}{m_0^2\omega^2}\sum_{v,c}\int_{BZ}\frac{2d^3k}{(2\pi)^3}|\hat{\epsilon}\cdot\mathbf{M}_{cv}(\mathbf{k})|^2\int dt\ \exp\{-i[E_{cv}(\mathbf{k})-i\Gamma+\hbar\omega]t-i\frac{(\theta t)^3}{12}\} \tag{43}$$

where $\hbar\theta$ is the electro-optic energy.

If the field is small or the broadening Γ large, such that $\Gamma >> \hbar\theta$, we can expand the exponent as follows: $\exp[-i(\theta t)^3/12] \approx 1-i(\theta t)^3/12$ and obtain an expression for ε_2 in the low field limit:

$$\varepsilon_2(E,F,\Gamma)=\varepsilon_2(E,0,\Gamma)+\frac{(\hbar\theta)^3}{12}E^2\frac{\partial^3}{\partial E^3}[E^2\varepsilon_2(E,0,\Gamma)]+\cdots \quad (44)$$

where t is operationally equivalent to $[i\hbar(\partial/\partial E)]$ in quantum mechanics.

Using the Kramers-Kronig relation, it also possible to obtain ε_1 in the presence of this weak electric field F:

$$\varepsilon_1(E,F,\Gamma)=\varepsilon_1(E,0,\Gamma)+\frac{(\hbar\theta)^3}{12}E^2\frac{\partial^3}{\partial E^3}[E^2\varepsilon_1(E,0,\Gamma)]+\cdots \quad (45)$$

Therefore change in the complex dielectric function in the presence of a weak electric field is given by:

$$\Delta\varepsilon=\frac{(\hbar\theta)^3}{12E^2}\frac{\partial^3}{\partial E^3}[E^2\varepsilon(E,\Gamma)] \quad (46)$$

As can be seen, the low field modulation ($|\hbar\theta| \leq \Gamma$) from flatband, i.e. no built-in dc field gives a third derivative spectroscopy. The more general situation when a built-in electric field can be present in a sample will be discussed later.

2.2.1.2 High Field Regime (Franz-Keldysh Oscillations)

For the unbound situation, in the event that the low-field criterion is not satisfied, then a full quantum mechanical treatment must be used. Several different but equivalent methods have been reported in the literature to calculate the dielectric function in the presence of the electric field [13-15]. We present only the simplest, i.e., the stationary state approach in the effective mass approximation [5].

The calculation starts with the center-of-mass problem of the electron and hole:

$$[(\frac{\hbar^2}{2\mu})\frac{\partial^2}{\partial z^2}+eFz+W_i]\phi_i(z)=0 \tag{47}$$

where μ is the effective reduced mass.

The convergent solution of Eq.(47) is given by:

$$\phi_i(z)=\frac{\sqrt{eF}}{\hbar\theta}Ai(\frac{eFz-W_i}{\hbar\theta}) \tag{48}$$

with eigenvalue W_i, with the z-axis parallel to F, $\hbar\theta$ electro-optic energy and Ai is the Airy function. The imaginary part of the dielectric function in the zero broadening limit is:

$$\varepsilon_2(E)=(\Xi/E^2)\sum_i |\phi_i(0)|^2\delta(W_i-E) \tag{49}$$

where $\Xi=(2e^2\hbar^2/m^2) \mid \hat{\epsilon}\cdot\mathbf{M}_{cv} \mid ^2 (2\mu/\hbar)^{3/2}$.

By substituting $\Phi_i(0)$ from Eq.(48) into Eq.(49), we obtain:

$$\varepsilon_2(E,F)=\frac{\Xi}{E^2}(\hbar\theta)^{\frac{1}{2}}\pi[Ai'^2(\eta)-\eta Ai^2(\eta)] \tag{50}$$

Using this result and its Kramers-Kronig transform, for a 3D critical point the dielectric function in the presence of a uniform field F (neglecting Γ) can be written as [5]:

$$\begin{aligned}\varepsilon(E-E_g,F) &= 1+\left[\frac{C\sqrt{\hbar\theta}}{E^2}\right]\{G(\eta)+iF(\eta)\} \\ &\quad + D\left(2\sqrt{E_g}-\sqrt{E_g+E}\right)/E^2\end{aligned} \tag{51}$$

where

$$F(\eta)=\pi[Ai'^2(\eta)-\eta Ai^2(\eta)]-(-\eta)^{\frac{1}{2}}H(-\eta) \tag{52}$$

$$G(\eta)=\pi[Ai'(\eta)Bi'(\eta)-\eta Ai(\eta)Bi(\eta)]+\eta^{\frac{1}{2}}H(\eta) \tag{53}$$

with

$$\eta=\frac{E_g-E}{\hbar\theta} \tag{54}$$

The quantities $G(\eta)$ and $F(\eta)$ are referred to as the electro-optic functions while $Ai(\eta)$, $Ai'(\eta)$, $Bi(\eta)$ and $Bi'(\eta)$ are Airy functions and their derivatives and $H(-\eta)$ is the unit step function [5]. The parameters *C* and *D* are related to matrix element effects and can be considered constants over the vicinity of the critical point.

Plotted by the solid line in Figure 2a is $\varepsilon_2(E\text{-}E_g, F)$, the imaginary part of Eq.(51). The dotted line is $\varepsilon_2(E\text{-}E_g,0)$. It can be seen that the field produces FKOs that are superimposed on top of the $(E\text{-}E_g)^{1/2}$ dependence of $\varepsilon_2(E\text{-}E_g,0)$ for a 3D M_0 critical point. In Figure 2b is a plot of the expression:

$$\begin{aligned}\Delta\varepsilon_2(\eta) &= \Delta\varepsilon_2(E-E_g,F)\\ &= \varepsilon_2(E-E_g,F)-\varepsilon_2(E-E_g,0) = C\frac{\sqrt{\hbar\theta}}{E^2}F(\eta)\end{aligned} \tag{55}$$

The curve in Figure 2b shows an exponential tail for $\eta>0$ and an oscillatory function for $\eta<0$. The position of the N^{th} extrema (E_N) in the FKOs are given by:

$$N\pi = (4/3)[(E_N-E_g)/\hbar\theta]^{3/2}+\chi \tag{56}$$

where E_N is the photon energy of the N^{th} extrema and χ is an arbitrary phase factor [5,16,17]. A plot of $(4/3)(E_N\text{-}E_g)^{3/2}$ vs the index number N will yield a straight line with

slope $(\hbar\theta)^{3/2}$. Therefore, the electric field, F, can be directly obtained from the period of FKOs if μ_l is known. Or conversely μ_l can be measured if the field is known.

In the presence of Lorentzian broadening (Γ) the field-induced change in the dielectric function $\Delta\varepsilon(E,F,\Gamma)$ can be obtained from the unbroadened change $\Delta\varepsilon(E,F,0)$, using [18]:

$$\Delta\varepsilon(E,F,\Gamma) = 1/\pi \int_{-\infty}^{\infty} \frac{\Delta\varepsilon(E',F,0)\Gamma}{(E-E')^2+\Gamma^2} dE' \tag{57}$$

A contour integral of Eq.(57) yields:

$$\Delta\varepsilon(E,F,\Gamma) = \Delta\varepsilon(E+i\Gamma,F) \tag{58}$$

Although the exact form of $\Delta R/R$ for the intermediate-field case with broadening is quite complicated, Aspnes and Studna [19] and Aspnes [16] have written down a relatively simple expression (for $E > E_g$):

$$\frac{\Delta R}{R} \propto \frac{1}{E^2(E-E_g)} \exp\left[-\frac{2\Gamma\sqrt{E-E_g}}{(\hbar\theta)^{3/2}}\right] \times \cos\left[(4/3)\left[\frac{E-E_g}{\hbar\theta}\right]^{3/2} + \chi\right] \tag{59}$$

To illustrate the effects of broadening Eq.(59) is plotted for values of the Γ=1.0, 1.5 and 2.0 in units of $\hbar\theta$ [18] in Figure 3. For the smallest Γ it is still possible to observe eight or nine FKOs. The effects of Γ becomes quite evident above about $-\eta$=8 in relation to the undamped case (see Figure 2b). Only two or three FKOs can still be seen for Γ=1.5 while Γ=2.0 the FKOs are completely damped out. In this case the EM

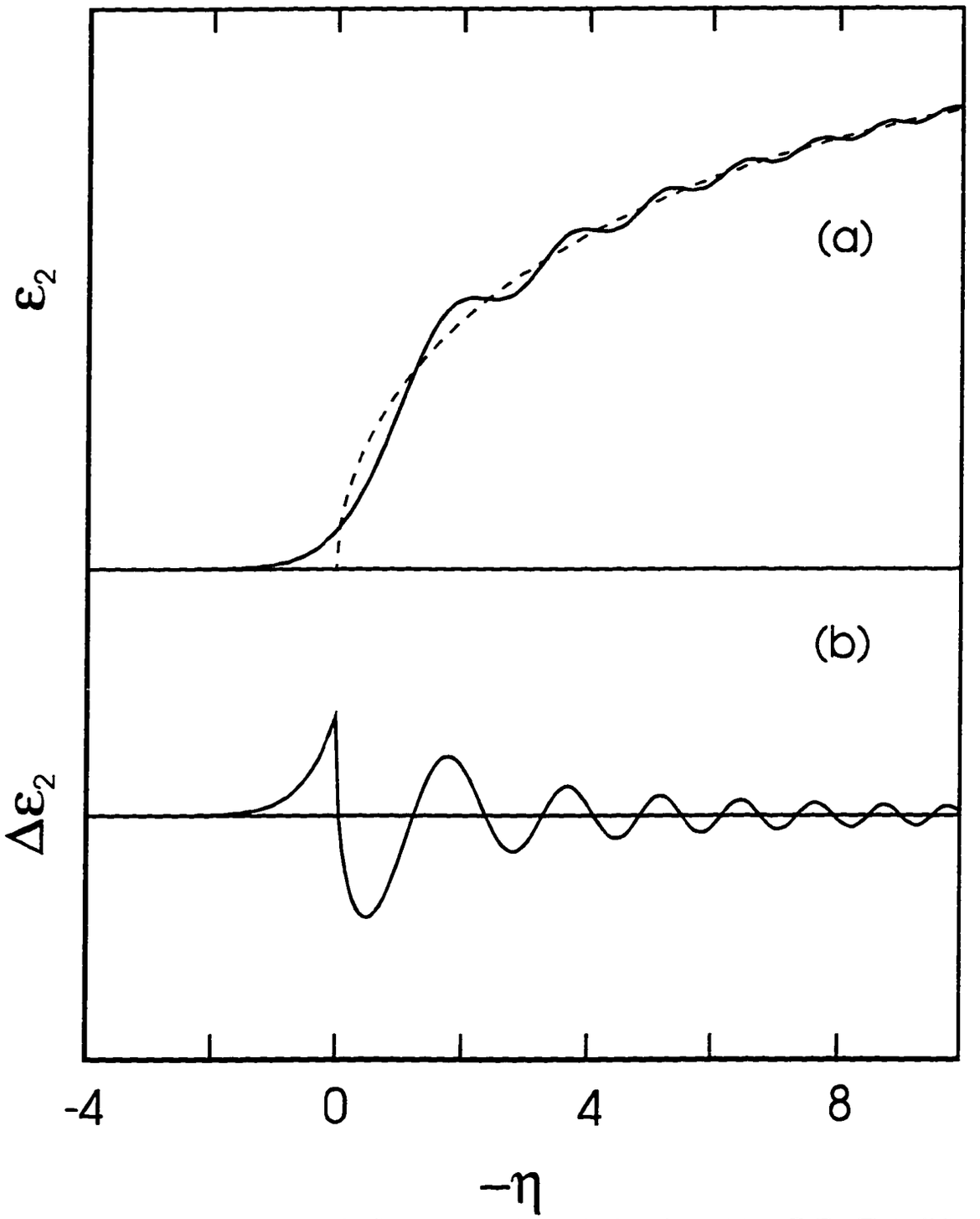

Figure 2. The effects of electric field on the dielectric function. (a) $\varepsilon_2(E-E_g, F)$ (solid) and $\varepsilon_2(E-E_g, 0)$ (dotted); (b) $\Delta\varepsilon_2=\varepsilon_2(E-E_g, F) - \varepsilon_2(E-E_g, 0)$.

is in the third-derivative regime discussed in Sec. 2.2.1.1 [5,16].

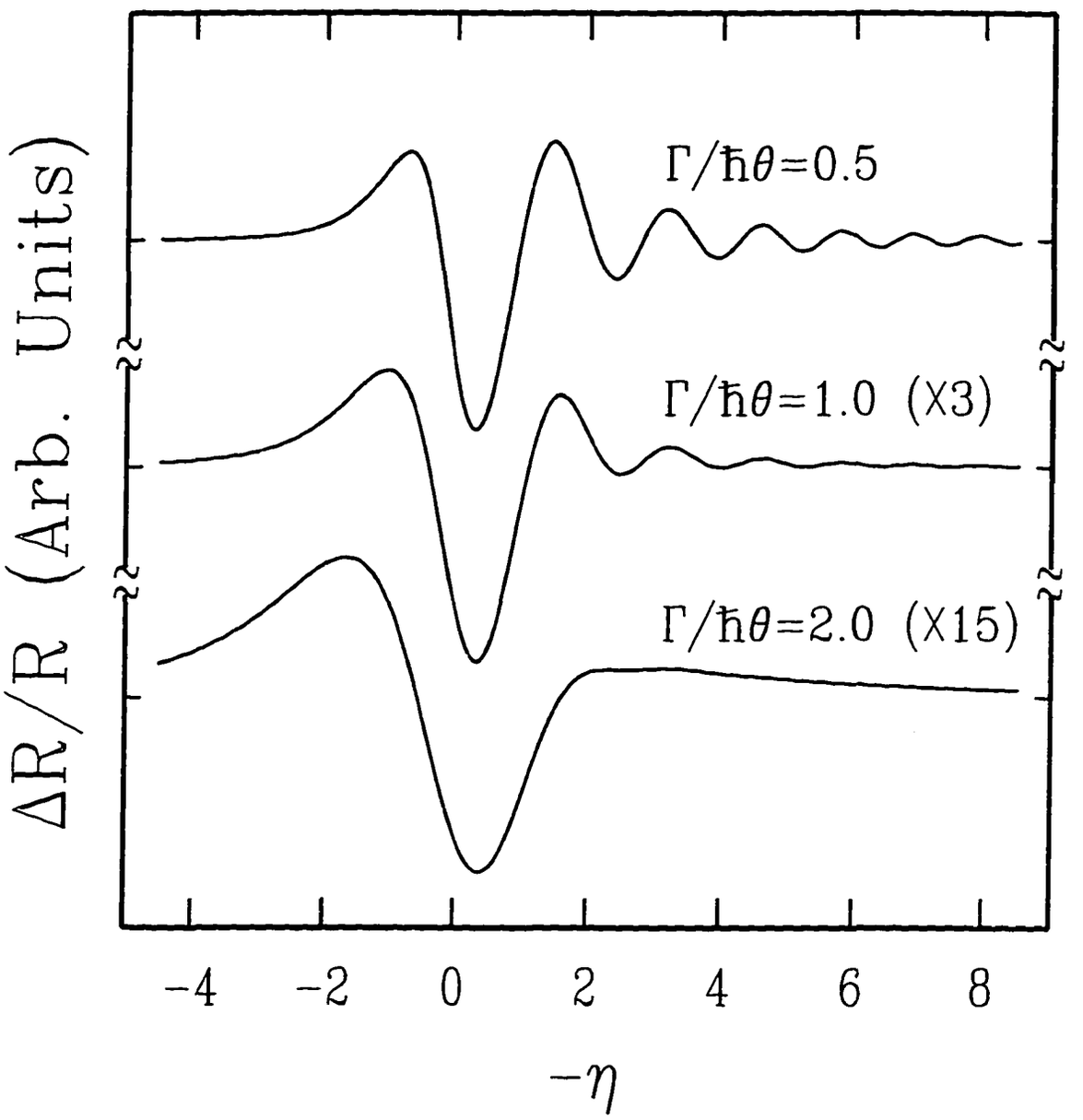

Figure 3. The effects of broadening on the FKOs.

The treatment of FKOs discussed above has assumed a uniform electric field. However, in many situations this is not the case. For example, in the space-charge region (SCR) of a doped semiconductor the field is non-uniform and varies linearly with distance (z) from the surface. For non-uniform fields the effective change in the

dielectric function $<\Delta\varepsilon>$ can be expressed as [5,17,18]:

$$<\Delta\varepsilon> = -2i\kappa_p(E)\int_0^\infty \exp[2i\kappa_p(E)z']\Delta\varepsilon[E-E_g,F(z')]dz' \qquad (60)$$

where $\kappa_p(E)$ (= $N\omega/c$) is the complex propagation vector of the light in the solid [see Eq.(12) for N].

The period of the FKOs is determined by the dominant field in the structure. In the expression for $\varepsilon(E,F)$ [see Eq.(51)] the nature of that field was not specified. There are two limiting cases to be considered. If modulation is from flatband, i.e., no dc field, then the field is clearly the modulating field, F_{ac}. Until recently most FKOs studies were performed in this regime [5]. However, a more interesting situation occurs when there exists a large dc electric field, F_{dc}, in the material and a small modulating field is applied, i.e., $F_{ac} << F_{dc}$. A built-in electric field can be present in a sample due to surface/interface Fermi level pinning, space charge distribution and piezoelectric effects [18,20]. The strength of such fields can easily reach the intermediate-field regime defined previously.

If the electric field is modulated by $\pm F_{ac}$ about F_{dc} the variation in the dielectric function $\delta\varepsilon(E,F_{dc},F_{ac})$ can be expressed as [17,18]:

$$\begin{aligned}\delta\varepsilon(E,F_{dc},F_{ac}) &= \varepsilon(E,F_{dc}+F_{ac})-\varepsilon(E,F_{dc}-F_{ac}) \\ &= \Delta\varepsilon(E,F_{dc}+F_{ac})-\Delta\varepsilon(E,F_{dc}-F_{ac})\end{aligned} \qquad (61)$$

where

$$\Delta\varepsilon(E,F)=\varepsilon(E,F)-\varepsilon(E,0) \qquad (62)$$

By neglecting broadening effects we are in the regime where $\Gamma << \hbar\theta$, where Γ is a

phenomenological broadening parameter.

Let us consider the case in which $F_{ac} << F_{dc}$. We referred to this situation as the low modulation field (LMF) criterion. Several approximations will be made. We denote as z the distance into the SCR as measured from the surface and ρ ($=e\ |\ N_D-N_A\ |$) as the net charge density, where N_D and N_A are the donor and acceptor concentrations, respectively. We assume that no significant free carriers are created in an EM experiment, i.e., ρ remains a constant. For the SCR the abrupt junction approximation is made so that F(z) is a linear function of z given by [18]:

$$F(z)=F^s_{dc}[(W-z)/W]=\frac{\rho}{\varepsilon_0}(W-z) \tag{63}$$

where F^s_{dc} is the surface dc electric field, W is the width of the SCR and ε_0 is the static dielectric constant.

In the nonuniform field regime the quantity $\delta\varepsilon(E,F_{dc},F_{ac})$ can be expressed as:

$$\delta\varepsilon^{ER}(E,F_{dc},F_{ac}) = -2i\kappa_p \left\{ \int_0^{W+\Delta W} \Delta\varepsilon[E,F(z-\Delta W)]\exp[i2\kappa_p z]dz - \int_0^{W-\Delta W} \Delta\varepsilon[E,F(z+\Delta W)]\exp[i2\kappa_p z]dz \right\} \tag{64}$$

The quantities $W+\Delta W$ and $W-\Delta W$ are the widths of the SCR for the case of $F_{dc}+F_{ac}$ and $F_{dc}-F_{ac}$, respectively. In Eq.(64) we have made use of the linear relation between F and z.

By making an appropriate change of variables in Eq.(64) we can write:

$$\delta\varepsilon^{ER}(E,F_{dc},F_{ac}) = -2i\kappa_p \left\{ \exp[i2\kappa_p\Delta W] \int_{-\Delta W}^{W} \Delta\varepsilon[E,F(z)]\exp[i2\kappa_p z]dz \right. \\ \left. -\exp[-i2\kappa_p\Delta W] \int_{\Delta W}^{W} \Delta\varepsilon[E,F(z)]\exp[i2\kappa_p z]dz \right\} \tag{65}$$

By making the LMF approximation, i.e., $\kappa_p\Delta W << 1$ and neglecting terms of order $(\Delta W)^2$ or higher, Eq.(65) can now be written as:

$$\delta\epsilon^{ER}(E,F_{dc},F_{ac}) = -2i\kappa_p \left\{ \int_{-\Delta W}^{\Delta W} \Delta\epsilon[E,F(z)]\exp[i2\kappa_p z]dz \right. \\ \left. +4i\kappa_p\Delta W \int_{0}^{W} \Delta\epsilon[E,F(z)]\exp[i2\kappa_p z]dz \right\} \tag{66}$$

From the linear relationship between F and z, we can write:

$$z=W(1-\chi) \tag{67}$$

where $\chi=F/F_{dc}^{s}$ and W is the width of the SCR for the case of the dc surface electric field F_{dc}^{s}. Also for η we can write:

$$\eta=\frac{\eta_{dc}^{s}}{\chi^{2/3}} \tag{68}$$

where

$$\eta_{dc}^{s}=\frac{(E_g-E)}{\hbar\theta_{dc}^{s}} \tag{69}$$

In addition we define [18]:

$$(\hbar\theta_{dc}^{s})^{3}=\frac{e^{2}\hbar^{2}(F_{dc}^{s})^{2}}{2\mu_{\parallel}} \tag{70}$$

$$\xi=\frac{F_{ac}^{s}}{F_{dc}^{s}}=\frac{\Delta W}{W} \tag{71}$$

Using the above equations and Eq.(51), the expression of Eq.(66) can be rewritten as:

$$\delta\epsilon^{ER}(E,F_{dc},F_{ac}) = [-4i\kappa_{p}(\frac{\epsilon_{0}}{\rho})(F_{dc}^{s})^{\frac{1}{3}}(F_{ac}^{s})](J_{s}+J_{av}) \tag{72}$$

where

$$J_{s}(\eta_{dc}^{s},\xi,0)=G_{s}(\eta_{dc}^{s},\xi,0)+iF_{s}(\eta_{dc}^{s},\xi,0) \tag{73}$$

$$J_{av}(\eta_{dc}^{s},\xi,0)=G_{av}(\eta_{dc}^{s},\xi,0)+iF_{av}(\eta_{dc}^{s},\xi,0) \tag{74}$$

The terms $J_{s}(\eta_{dc}{}^{s},\xi,0)$ and $J_{av}(\eta_{dc}{}^{s},\xi,0)$ represent the contribution of the "surface" (J_{s}) and "average" (J_{av}) electric fields to the FKOs for the unbroadened case ($\Gamma=0$). As it was shown by Shen and Pollak [18] the period of the FKOs from both these terms yields $F_{dc}{}^{s}$ as long as the modulation is in the LMF regime. Complete expressions for G_{s}, F_{s}, G_{av} and F_{av} also can be found in this reference.

2.2.1.3 Confined Systems

For bound states such as excitons, impurities, states of QWs or the uncoupled states of MQWs, the perturbing field does not accelerate electrons and/or holes. These types of particles do not have translational symmetry and are confined in space. Their energy spectrum is discrete and not continuous as in the case of the unbound particles. In this situation the modulating field can alter the binding energy of the particle.

Since for confined systems, the energies (in the confinement direction for microstructures) are discrete and dispersionless, this results in an infinite effective mass (in the confinement direction). An applied electric field (along the confinement direction) adds a linear potential, which tilts the confining potential, changing its shape. The electrons and holes become spatially polarized, but still remain confined. This alters both the electronic energies and the wave function overlap [intensity (I)]. Also the tilting of the potential can result in a change in lifetime Γ as a result of tunneling. In terms of EM, the infinite mass means that Eq.(46) is no longer applicable since $\hbar\theta=0$. Several authors have treated this problem in detail [18,20-29]. They have shown that under these conditions the change in the dielectric function induced by the modulating field, F_{ac}, is first-derivative and not the third derivative as for 3D systems.

We will assume that the confining potential is along the z-direction. The wave function can be written then as the product of an envelope function and a Bloch state representing the unconfined direction. This issue will be discussed in detail later. Because of the confining, k_z is no longer an eigenvalue of the system the expression for the dielectric function has to be modified [29]:

$$\varepsilon(E,\Gamma)=1+\frac{8\pi^2 ie^2\hbar}{m^2E^2L}\sum_{\alpha\beta}\int_{BZ}d^2k\int_0^{\infty}dt\,|\hat{\varepsilon}\cdot\mathbf{p}_{cv}(\mathbf{k})I_{\alpha\beta}|^2 \times\exp\{\int_{-\frac{t}{2}}^{\frac{t}{2}}dt'\frac{i[E+i\Gamma-E_{cv}^{\alpha\beta}(\mathbf{k})]t'}{\hbar}\} \tag{75}$$

where α and β are the subband indices of the conduction and valence bands, L is the width of the confined region, and $I_{\alpha\beta}$ is the overlap integral between the electron and hole envelope functions (subband states). The sum over the subband states replaces the

integral over k_z for unbound particles. For an electric field applied along the direction of confinement, the shape of the confining potential changes, and if the field is small new quasibound states are formed. In addition, the new potential redistributes the electronic charge in such a way that electrons and holes are localized at opposite ends of the confining region. This effect is reflected in both the form of the wave functions and the overlap integral $I_{\alpha\beta}$. Unlike the unbound case, however, the new potential does not accelerate the particles. Thus, at any two times after the field is applied, the energy of the particle is unchanged because it is in a quasibound state. The main effect of the field is just to change the energy level, the functional forms of the wave functions, and the lifetime of the particle. For confined particles the energy changes by a fixed amount rather than in a continuous fashion as it would in the case of a free particle. We cannot replace $\mathbf{k}$ by $\mathbf{k} - e\mathbf{F}t/\hbar$ and we should change the interband energy $E_{cv}^{\alpha\beta}(\mathbf{k})$ and the overlap integral between electrons and holes, $I_{\alpha\beta}$, by some fixed amount that is not dependent on the time t. The new energy is given by $E_{cv}^{\alpha\beta}(\mathbf{k})+\delta E_{cv}^{\alpha\beta}$ and the new overlap integral is $I_{\alpha\beta}+\delta I_{\alpha\beta}$. The quantities $\delta E_{cv}^{\alpha\beta}$ and $\delta I_{\alpha\beta}$ can be calculated from stationary-state perturbation theory.

If $\delta E_{cv}^{\alpha\beta}$ is much smaller than any other energy in the problem and $\delta I_{\alpha\beta}/I_{\alpha\beta} << 1$, we can expand the exponent and the overlap integral to obtain:

$$\varepsilon(E,\Gamma)=1+\frac{iA'}{E^2}\sum_{\alpha\beta}|I_{\alpha\beta}|^2\left(1+\frac{2\delta I_{\alpha\beta}}{I_{\alpha\beta}}\right)\int_{BZ}d^2k\int_0^\infty dt\left(1+\frac{it\delta E_{cv}^{\alpha\beta}}{\hbar}\right)\times\exp\left\{\frac{i[E-E_{cv}^{\alpha\beta}(\mathbf{k})+i\Gamma]t}{\hbar}\right\} \tag{76}$$

where $A' = 8\pi^2e^2\hbar\,|\,\hat{\epsilon}\cdot\mathbf{p}_{cv}\,|^2/m^2L$.

Performing the integral over t and keeping only first order terms in the perturbation leads to:

$$\varepsilon(E,\Gamma)=1+\frac{iA'}{E^2}\sum_{\alpha\beta}|I_{\alpha\beta}|^2\int_{BZ}d^2k\{\frac{i\delta E_{cv}^{\alpha\beta}}{[E-E_{cv}^{\alpha\beta}(\mathbf{k})+i\Gamma]^2}+\frac{(1+2\delta I_{\alpha\beta})/I_{\alpha\beta}}{E+E_{cv}^{\alpha\beta}(\mathbf{k})+i\Gamma}\} \qquad (77)$$

This is the general result for any type of one-dimensional (1D) confining potential with the electric field applied along the confinement direction. The first term under the integral represents changes in ε from electric-field-induced changes in the gap, $E_{cv}^{\alpha\beta}$, while the second term is a combination of the unperturbed dielectric function and a term due to the modulation of the overlap integral. The most important fact is that the modulated terms are first derivatives and not third derivatives as in the bulk case.

If we perform the integrals over the wavevector **k** and we include the possibility that the electric field can modulate the lifetime of the state, as in the case of field-induced tunneling, $\Delta\varepsilon$ can be expressed in a compact manner as a first derivative functional form for the modulated dielectric function [18,20-29]:

$$\Delta\varepsilon = [(\partial\varepsilon/\partial E_g)(\partial E_g/\partial F_{ac})+(\partial\varepsilon/\partial\Gamma)(\partial\Gamma/\partial F_{ac})+(\partial\varepsilon/\partial I)(\partial I/\partial F_{ac})]F_{ac} \qquad (78)$$

where

$\partial E_g/\partial F_{ac}$ is the change in energy due to the Stark effect,

$\partial E_g/\partial F_{ac}$ is the change in broadening parameter due to a variation of the lifetime,

$\partial E_g/\partial F_{ac}$ is the change in intensity due to redistribution of charges.

This equation can be rewritten as [30]:

$$\Delta\varepsilon_j = [A_E f_E^{(j)} + A_\Gamma f_\Gamma^{(j)} + A_I f_I^{(j)}](I/\Gamma)F_{ac} \qquad (j = 1,2) \tag{79}$$

with

$$A_E = (1/\Gamma)(\partial E_g/\partial F_{ac}) \tag{80}$$

$$A_\Gamma = (1/\Gamma)(\partial\Gamma/\partial F_{ac}) \tag{81}$$

$$A_I = (1/I)(\partial I/\partial F_{ac}) \tag{82}$$

and

$$f_E^{(j)} = (\partial\varepsilon_j/\partial E_g) \tag{83}$$

$$f_\Gamma^{(j)} = (\partial\varepsilon_j/\partial\Gamma) \tag{84}$$

$$f_I^{(j)} = (\partial\varepsilon_j/\partial I) \tag{85}$$

This is the most general form of the modulated dielectric function for confined systems. It is important to notice that it applies only when the field is along the direction of confinement. For transverse fields, the third derivative functional form is applicable and for fields along any arbitrary direction, the lineshapes will be combinations of both, the first and third derivative functional forms.

2.2.2. Piezomodulation

Since the piezomodulation method does not destroy the translation symmetry of the material, the lineshape will be the first-derivative expression of Eq.(78). However,

the band gap modulation term is due not to the Stark effect, as in EM, but is created by the stress dependence of the energy gaps. Thus for PzR Eq.(78) is appropriate with F_{ac} replaced by the modulating stress S_{ac}.

2.3 Functional Form of the Dielectric Function

2.3.1 Unbound States

As remarked earlier the structures in modulation spectra are localized in photon energy. Because of this fact, we have the enormously simplifying results that for the purpose of analyzing modulation spectra it is usually entirely adequate to replace the actual complicated dispersion of the energy bands with local parabolic expansions in the neighborhood of the critical points [5]. If the Coulomb interaction between the electrons and holes is neglected, in the one-particle picture for the case in which the linewidth is primarily due to lifetime broadening, the local expression of the dielectric function takes a simple Lorentzian form which is given for a 1D, two-dimensional (2D), and 3D critical points [5] by Eq.(32).

Given the above explicit functional form of the dielectric functions, the low field EM lineshape can be obtained by substituting the 3D expression of Eq.(32) into Eq.(46) and the resulting expression takes a particularly simple form [5]:

$$\Delta R/R = (\hbar\theta)^3 \mathrm{Re}[Ae^{i\phi}(E-E_g+i\Gamma)^{-r}] \tag{86}$$

or

$$\Delta R/R = (\hbar\theta)^3 L(E-E_g,\Gamma) \tag{87}$$

where

$$L(E-E_g,\Gamma) = Re[Ae^{i\phi}(E-E_g+i\Gamma)^{-\nu}] \tag{88}$$

In Eqs. (86) and (88) A is the amplitude, ϕ is a phase angle which accounts for Eq.(33) and the influence of non-uniform electric fields as well as interference and electron-hole interaction effects [4,5]. The lineshape factor $L(E-E_g,\Gamma)$ is independent of the modulating field in the low-field regime.

The parameter ν in the lineshape factor of Eq.(88) depends on critical point type and method of the modulation. For EM, for a 3D M_0 critical point, such as the direct gap of GaAs, $\nu=2.5$. For a 2D critical point $\nu=3$ [5].

The change in the dielectric functions induced by piezomodulation can be obtained by substituting the appropriate dielectric functions from Eq.(32) into the first-derivative expression of Eq.(78). It is straight forward to see that the lineshape function has the same form of Eq.(86) with ν taking a value from that of EM for a given type critical point. For a 3D M_0 critical point, $\nu=0.5$ for PzR.

In arriving at the Lorentzian form of the dielectric function of Eq.(32), the broadening of transitions has been assumed to be predominantly due to the lifetime effects. If the relaxation of the electron-hole pair excitation of the crystal is primarily associated with a large number of weak scattering centers and statistical inhomogeneity, the dielectric function will have a Gaussian form [31-34]. The general form of the Gaussian dielectric function (ε_G) can be expressed as [33,34]:

$$\varepsilon_G(E,\Gamma) = \frac{Const}{E^2}\int_{B.Z.} d^l k \int_0^{\infty} ds\,(-i)\exp\{is[E-E_{cv}(\mathbf{k})] - 2s^2\Gamma^2\} \qquad (89)$$

where the interband transition matrix element has been considered a constant, Γ is a broadening parameter and $E_{cv}(\mathbf{k})$ is the difference between the conduction band and the valence band dispersions. For low-field EM the field induced change in the dielectric function is calculated by substituting Eq. (89) into Eq.(46). Similarly the stress induced change in the dielectric function in the case of piezomodulation is obtained by taking the first derivative of Eq. (89) with respect to the energy gap. The lineshape function is then obtained from Eq.(33) [34].

2.3.2. Bound States

The unperturbed dielectric function for a bound state transition of Eq.(78) or (79) will be either Lorentzian or Gaussian, depending on the broadening mechanism and/or temperature [24,29,35,36].

One extremely important case of bound states is the QW system. The quantum levels in QW structures are bound states with respect to the motion of electrons and holes along the growth direction (assumed to be the z-axis). The carriers in these states are confined in the z-direction, but free to move in the xy-plane, exhibiting a quasi 2D character. The reduction in dimensionality from 3D to 2D changes the absorption profile from a square root dependence on photon energy of bulk material to a 2D form which consists of a series of quantized step functions independent of photon energy. In addition, the 2D character of the system enhances exciton binding energy effects. Shown

in Figure 4 by the dot-dashed line is ε_2 for the 3D case of bulk material while the dashed line is the step-like 2D profile. The solid line shows schematically the influence of the excitons. The energy difference between the exciton peak and the corresponding step in the 2D absorption edge is the exciton binding energy. Therefore, in undoped QW structures, even at 300K, the absorption profile (ε_2) consists of sharp excitonic peaks, superimposed on a step-like two-dimensional joint density of states (2DJDS). In this case $\Delta\varepsilon$ in Eq.(78) or (79) is the first derivative of a Lorentzian (FDLP) or Gaussian profile (FDGP), depending on the nature of the broadening mechanism of the exciton.

In the following we will discuss the first-derivative lineshapes for Lorentzian and Gaussian broadening in detail.

The Lorentzian dielectric function can be written as [5,36-38]:

$$\varepsilon = 1 + \frac{I}{E - E_g + i\Gamma} \tag{90}$$

The various modulation terms of Eqs. (79)-(85) are given by:

$$f_E^{(1)} = (y^2 - 1)/(y^2+1)^2 \tag{91}$$

$$f_E^{(2)} = -2y/(y^2+1) \tag{92}$$

$$f_\Gamma^{(1)} = f_E^{(2)} \tag{93}$$

$$f_\Gamma^{(2)} = -f_E^{(1)} \tag{94}$$

$$f_I^{(1)} = y/(y^2+1) \tag{95}$$

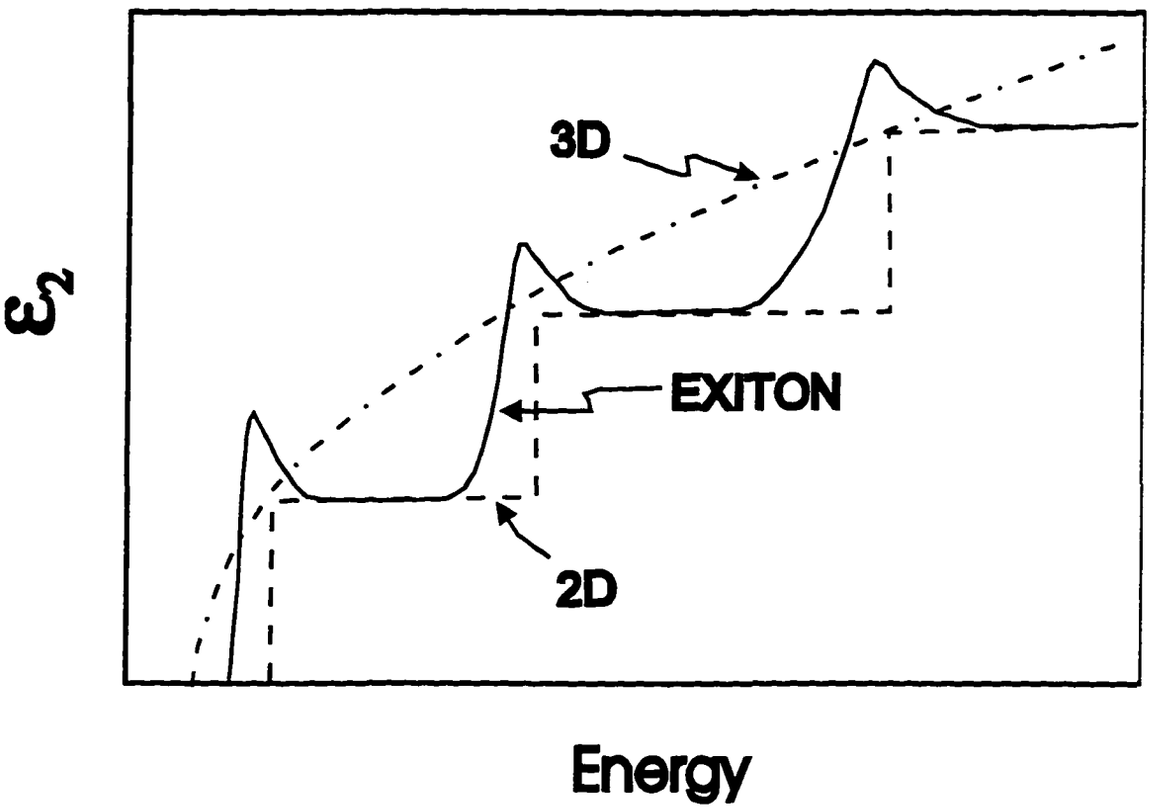

Figure 4. Schematic representation of ε_2 for a three-dimensional M_0 critical point (dot-dashed), two-dimensional joint density of states (dashed) and exciton (solid).

$$f_1^{(2)} = -1/(y^2+1) \tag{96}$$

where

$$y = (E - E_g)/\Gamma \tag{97}$$

The relations between the energy gap and broadening modulation terms of Eqs. (93) and (94) are due to the symmetry of E_g and Γ in Eq. (90).

Plotted in Figure 5 are $f_E^{(1)}$ [$= -f_\Gamma^{(2)}$], $f_E^{(2)}$ [$= f_\Gamma^{(1)}$] and $f_I^{(1)}$, $f_I^{(2)}$ as a function of y for the Lorentzian case. If intensity modulation terms are neglected there are only two independent lineshape factors. The combined spectral dependence can then be analytically expressed by Eq.(88) with $\nu=2$ [5].

If the unperturbed profile is Gaussian the situation is more complicated since E_g and Γ no longer have the same symmetrical relation as in Eq. (90). The unperturbed dielectric function is obtained from Eq (89) and is given by [30]:

$$\varepsilon_G = 1 + I(L_1 + iL_2) \tag{98}$$

where

$$L_1 = -(y/\Gamma)\Phi(1, 3/2, -y^2/2) \tag{99}$$

$$L_2 = -(\pi/2)^{\frac{1}{2}}(1/\Gamma)\exp(-y^2/2) \tag{100}$$

where y is given by Eq.(97) and Φ is the confluent hypergeometric function.

In this case the various modulation terms of Eqs.(79)-(85) can be written as:

$$f_E^{(1)} = -\Phi(1, 1/2, -y^2/2) \tag{101}$$

$$f_E^{(2)} = -(\pi/2)^{\frac{1}{2}} y \exp(-y^2/2) \tag{102}$$

$$f_\Gamma^{(1)} = -2y\Phi(2, 3/2, -y^2/2) \tag{103}$$

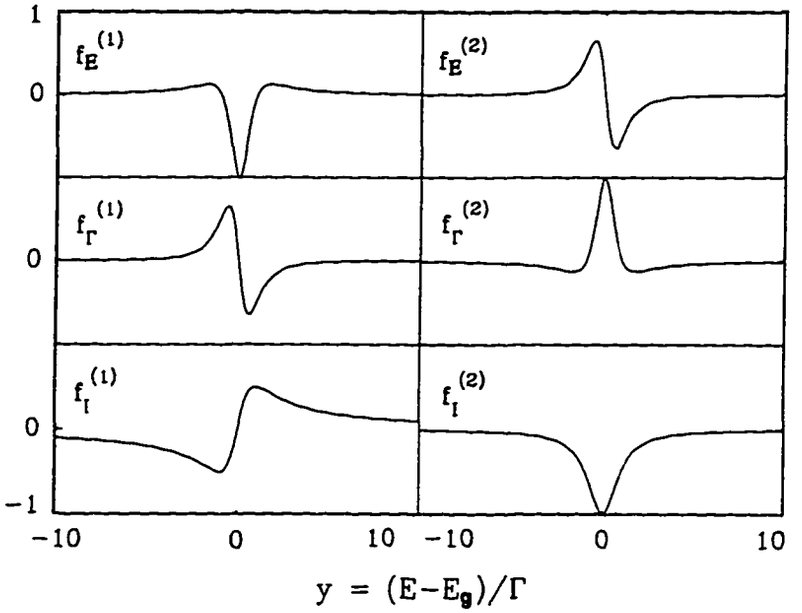

Figure 5. Calculated lineshapes for the first derivatives of ε_1 and ε_2 of a Lorentzian dielectric function given in Eqs. (91)-(97).

$$f_\Gamma^{(2)} = -(\pi/2)^{\frac{1}{2}}(y^2-1)\exp(-y^2/2) \tag{104}$$

$$f_I^{(1)} = y\Phi(1,3/2,-y^2/2) \tag{105}$$

$$f_I^{(2)} = -(\pi/2)^{\frac{1}{2}}\exp(-y^2/2) \tag{106}$$

In contrast to the Lorentzian situation there is no simple, analytical relation between $f_E^{(1)}$ $[f_E^{(2)}]$ and $-f_\Gamma^{(2)}$ $[f_\Gamma^{(1)}]$.

Plotted in Figure 6 are the various modulation terms of Eqs. (101)-(106). Note that although $f_E^{(1)}$ $[f_E^{(2)}]$ and $-f_\Gamma^{(2)}$ $[f_\Gamma^{(1)}]$ are not exactly the same, as in the case of the Lorentzian profile, their lineshapes look very similar, i.e., $f_E^{(1)} \approx -f_\Gamma^{(2)}$ and $f_E^{(2)} \approx f_\Gamma^{(1)}$. Therefore, for many practical applications, if $f_I^{(1)}$ and $f_I^{(2)}$ are neglected, only two lineshape profiles need to be used to fit experimental data. Hence, even for the Gaussian situation an expression similar to Eq. (88) can be used, i.e.,

$$\frac{\Delta R}{R} = \mathrm{Re}\{Ae^{i\phi}[f_E^{(1)} + if_E^{(2)}]\} \tag{107}$$

It should be noted that in high quality bulk materials grown by techniques such as MBE or vapor phase epitaxy, direct gap excitons may be present even at 300K [39]. In such cases the first-derivative lineshape form of Eq.(78) will be appropriate rather than the third-derivative profile of band-to-band transitions.

2.4 Instrumentation

Modulation spectroscopy can be accomplished in several ways, including contact and contactless modes. Contactless EM is particularly useful since it can be employed on wafer-sized material without altering the sample. Contactless EM can be performed

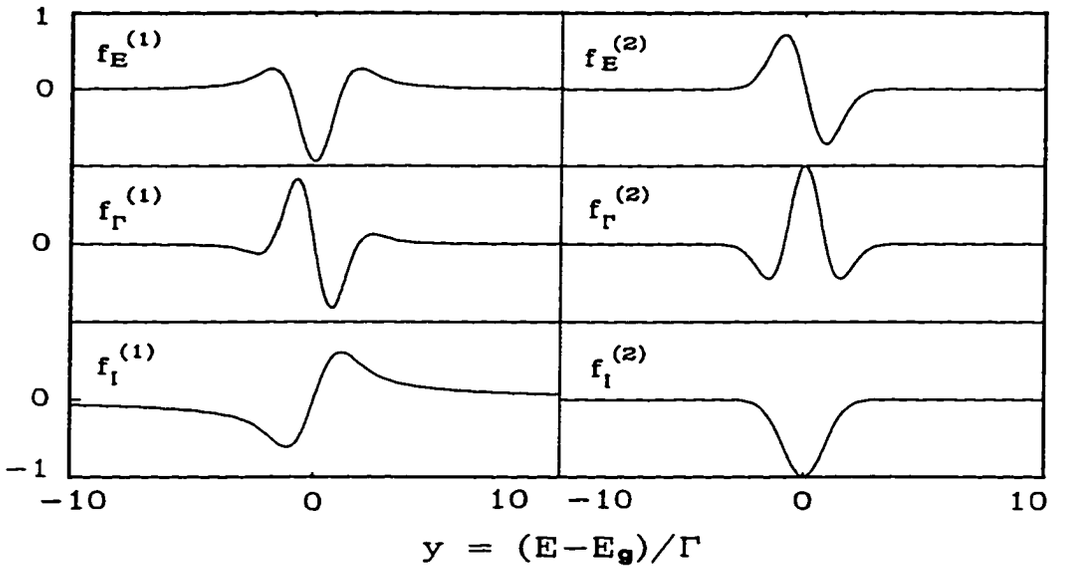

Figure 6. Calculated lineshapes for the first derivatives of ε_1 and ε_2 of a Gaussian dielectric function given in Eqs. (101)-(106).

using PR, which requires no special mounting of the sample [24,38] or contactless electroreflectance (CER), an approach which uses a capacitor-like arrangement [40-43].

Shown in Figure 7 is a schematic drawing of the experimental arrangement for a general "external" modulated reflectance experiment [5,28]. Light from an appropriate light source (Xenon arc or tungsten lamp) passes through a monochromator (probe

monochromator). The exit intensity at wavelength λ, $I_o(\lambda)$, is focussed onto the sample by means of a lens (or mirror). The modulation (electric field, stress, temperature) is applied to the sample at frequency Ω_m. The reflected light is collected by a second lens (mirror) and is focussed onto an appropriate detector (photomultiplier, photodiode, etc.). For the sake of simplicity the two lenses (mirrors) are not shown. For modulated transmission the detector is placed behind the sample. In general, however, reflectance is more useful.

The light striking the detector contains two signals: the dc (or average value) is given by $I_o(\lambda)R(\lambda)$, where $R(\lambda)$ is the dc reflectance of the material while the modulated value (at frequency Ω_m) is $I_o(\lambda)\Delta R(\lambda)$, where $\Delta R(\lambda)$ is the change in reflectance produced by the modulation source. The ac signal from the detector, proportional to $I_o\Delta R$, is measured by a lock-in amplifier (or other signal averaging procedure). Typically $I_o\Delta R$ is 10^{-4}-10^{-6} of I_oR. A servo mechanism is used to maintain a constant dc signal, therefore the ac output from the lock-in amplifier is proportional to the normalized signal $\Delta R/R$.

2.4.1 Photoreflectance

The method of PR is not only contactless but requires no special mounting of the sample. It can be used in any transparent medium under a variety of conditions. It has been demonstrated that PR can be used at temperatures as high as 650°C [28].

Shown in Figure 8 is the schematic representation of a PR apparatus [24,44]. In PR modulation of the electric field in the sample is caused by photo-excited electron-hole pairs created by the pump source (laser or other light source) which is chopped at

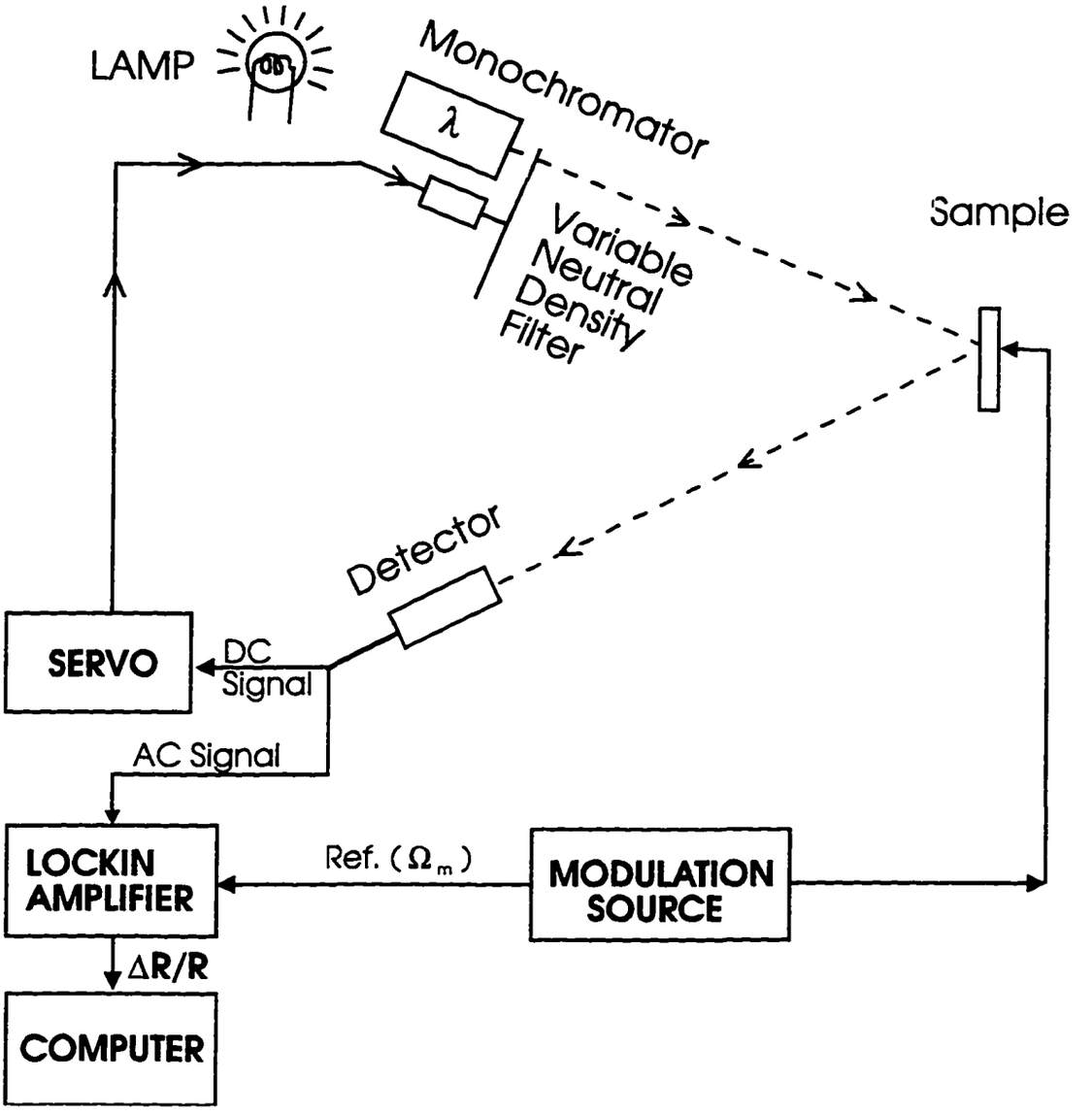

Figure 7. Schematic representation of an "external modulation" experimental apparatus [5,28].

frequency Ω_m. Most PR experiments have utilized a mechanical chopper with maximum $\Omega_m \approx 5$ kHz. To achieve higher modulation frequencies up to about 1MHz an acousto-optic modulator can be used [45]. The photon energy of the pump source should be

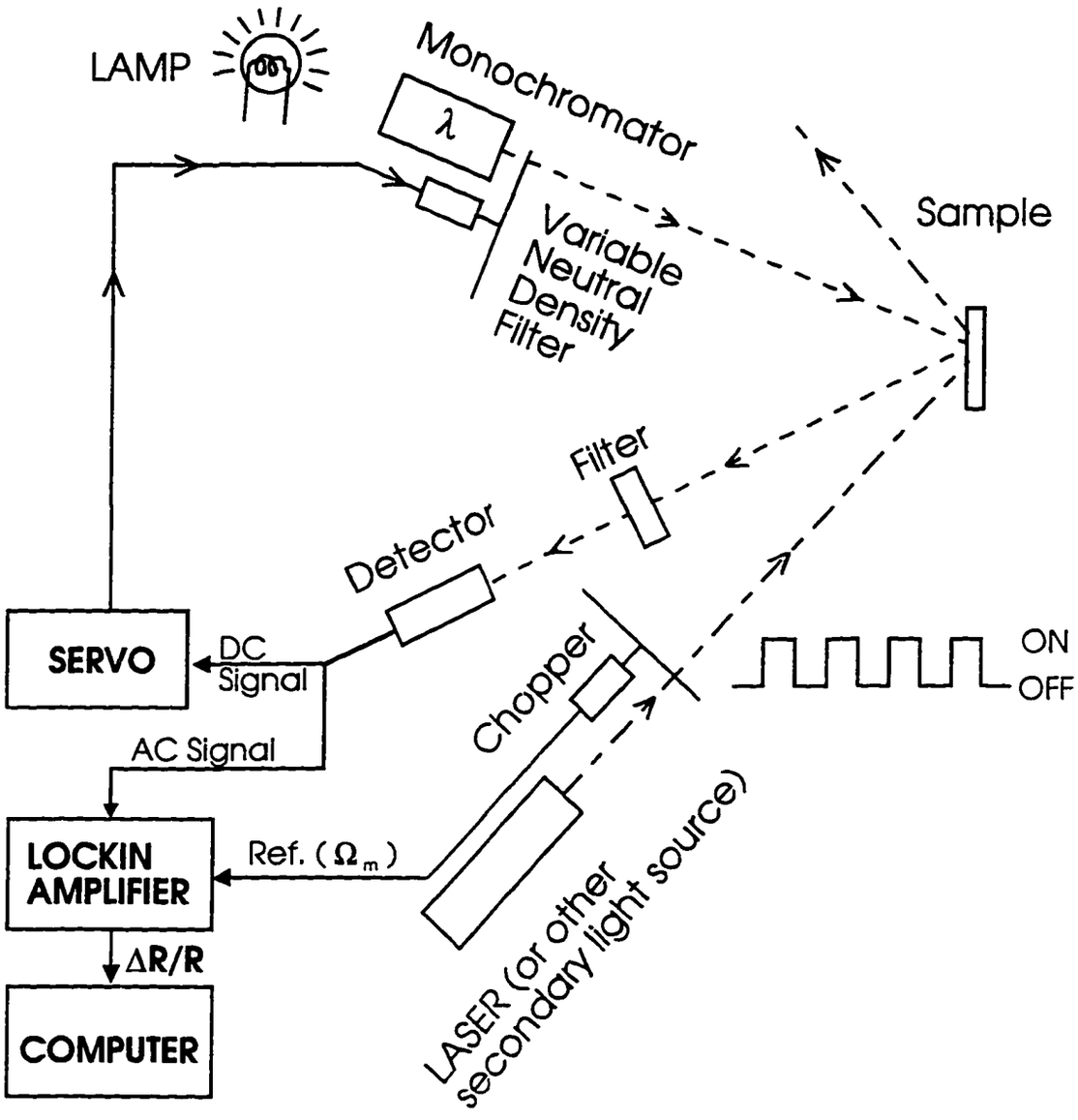

Figure 8. Schematic representation of a PR apparatus [44].

above the band gap of the semiconductor being investigated. The pump creates photo-injected electron-hole pairs which modulate the built-in electric field of the semiconductor or semiconductor microstructure under investigation. A typical pump source is a 5mW He-Ne laser.

A drawback of PR is the spurious modulated background signal reaching the detector because of (a) luminescence from the sample and/or (b) scattered light from the pump source. Luminescence can sometimes be a problem for measurements near the fundamental gap, particularly at low temperatures. Scattered pump light can be reduced by means of an appropriate long pass filter in front of the detector. If the overall spurious background signal is not too large in relation to $\Delta R/R$, it can be subtracted by the normalization method of Figure 8 (the spurious light is not optically dispersed and shows up a large, wavelength-independent background signal).

The spurious background signal also can be reduced or eliminated by approaches such as the use of a double monochromator [46], tuneable dye laser as the probe beam [47], sweeping PR [48], differential PR [49] or a properly phase shifted signal from the reference source that is applied to the lock-in amplifier's input [50].

2.4.2 Contactless Electroreflectance

A CER method utilizes a condenser-like system consisting of a thin, transparent, conductive coating (indium-tin-oxide or 50-60Å of a metal such as Au or Ni) on a transparent substrate (glass, quartz, etc.) which serves as one electrode [40-42]. A second electrode consisting of a metal strip is separated from the first electrode by an insulating spacer. The sample ($\sim$0.5mm thick) is placed between these two capacitor plates. The dimensions of the spacer are such that there is a very thin layer ($\sim$0.1mm) of air (or vacuum) between the front surface of the sample and the conducting part of the first electrode. Thus, there is nothing in direct contact with the front surface of the

sample. Shown in Figure 9 is an illustration of the sample holder and electrode arrangement. The ac modulating (~ 1kV peak-to-peak) and dc bias voltages are applied between the metal strip and the transparent conductor. The probe beam is incident

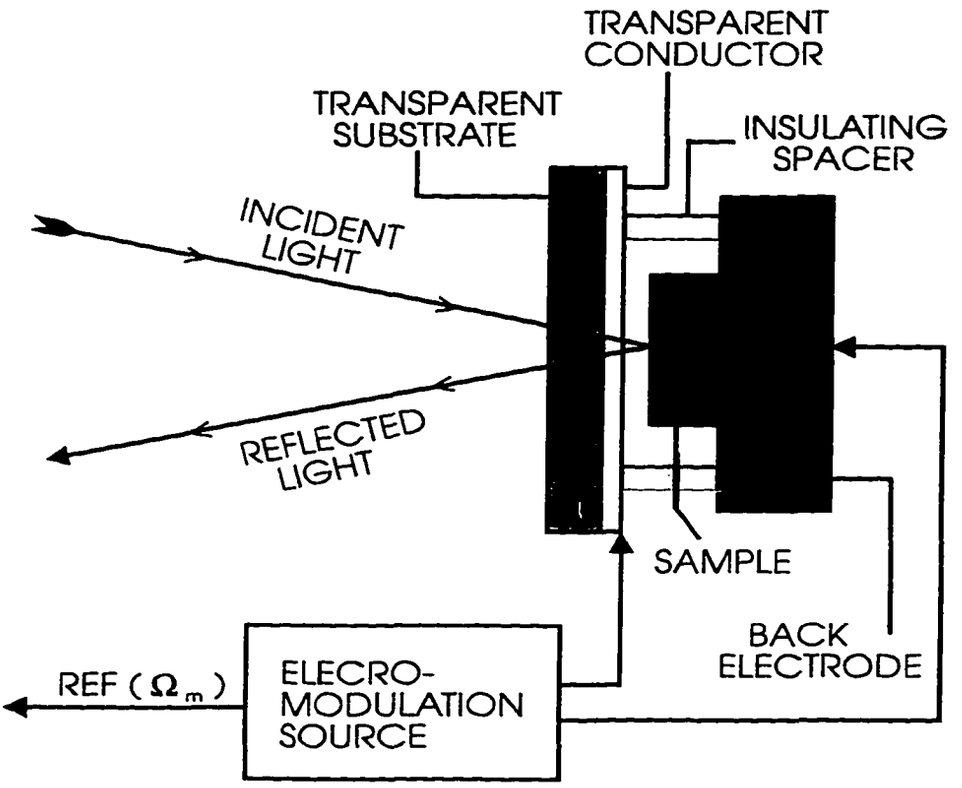

Figure 9. Schematic view of the condenser-like arrangement used in CER experiments.

through the first transparent electrode. This approach can also be employed in the transmission mode by replacing the metal electrode with a second transparent electrode/substrate.

2.4.3 Piezoreflectance

In piezoreflectance (PzR), modulation is achieved by mounting the sample on a piezoelectric transducer which varies the lattice constant of the material producing a band gap modulation. Although PzR is contactless it requires special mounting of the sample.

Chapter 3. II-VI EPILAYERS OF ZnSe AND ZnCdSe

3.1 Introduction

The semiconductor ZnSe and ZnSe-based alloys are important materials from both fundamental and applied perspectives. In recent years, these semiconductors have received considerable attention due to their potential in the fabrication of blue-green laser devices. The only continuous wavelength blue semiconductor lasers reported to date are based on these materials [1,2]. However, some parameters of the operating devices such as lifetime require optimization of the laser structure itself. In particular, for the optimum device design it is necessary to select the materials that provide the desired bandstructure for effective optical and carrier confinement and over-all device performance. A detailed understanding of the nature of these materials is essential in order to make the best selection. The binary semiconductor ZnSe and ternary alloy ZnCdSe are of particular interest since they are presently used in the active region of the reported semiconductor laser.

However, in spite of their significance, very little work has been done on the temperature dependence of the fundamental band gap of these materials. The temperature dependence of the energy and broadening of interband electronic transitions can yield important information about electron-phonon interactions, excitonic effects, etc.[3-6]. The practical aspect of this investigation is related to the control of the operating temperature of the laser structure itself. An increase in temperature leads to a redshift

of the band gaps and an increase in the linewidth.

In this chapter we report a detailed investigation of the temperature dependence of the energy $E_0(T)$ and broadening parameter $\Gamma_0(T)$ of the direct gaps of ZnSe and $Zn_{0.56}Cd_{0.44}Se$ (lattice-matched to InP) using CER in the temperature range $25K < T < 400K$. We have analyzed the temperature variation of the energy gap by both the Varshni equation [7] and a more recent expression containing the Bose-Einstein occupation factor for phonons [3]. By taking into account the thermal expansion contribution to $E_0(T)$ we have obtained revised parameters which are directly related to the electron-phonon interaction. The temperature dependence of the broadening function also has been studied in terms of a Bose-Einstein equation which contains the exciton-longitudinal optical (LO) ($q \approx 0$) phonon coupling constant [3].

3.2 Temperature Dependence of the Energy Gaps and Broadening Parameters

3.2.1 Bose-Einstein Theory

The temperature dependence of energy gaps [$E_g(T)$] and broadening parameters [$\Gamma(T)$] can provide important information about the electron-phonon interaction, exciton effects, etc. For energy gaps, temperature variations are due to both lattice constant variations and interactions with relevant acoustic and optical phonons. Since thermal expansion of the lattice is easy to deal with, let us concentrate first on electron-phonon interaction.

It is well known that the electron-phonon interaction contributes to both the temperature shift of the energy gap and to the increase of the lifetime broadening.

Cardona *et al.* have made extensive microscopic analysis of these temperature dependent shifts and broadening for such semiconductors as Ge [8-10], Si [8-11] and GaAs [3] based on the renormalization of the band energies by the electron-phonon coupling. We illustrate here the treatment presented by Cardona *et al.* [8,11,12], outlining the basic equations and physical implication.

Consider a crystal with atoms of species κ that occupy sites $\mathbf{R}(l, \kappa)$ and have displacements $\mathbf{u}(l, \kappa)$ from equilibrium, where l labels the unit cells. In order to describe the renormalization of the semiconductor band structure by the electron-phonon interaction, the electron-atom interaction $V[\mathbf{r}-\mathbf{R}(l, \kappa)-u(l,\kappa)]$ is Taylor expanded about the position $\mathbf{u}(l, \kappa)=\mathbf{0}$. The zeroth-order Hamiltonian H_0 gives the one-electron states $|\mathbf{k},n>$ and band energies at $T=0$, $E_{kn}(0)$ where $\mathbf{k}$, n are the wave vector and the band index, respectively. The first two terms of the expansion of $V[\mathbf{r}-\mathbf{R}(l,\kappa)-\mathbf{u}(l, \kappa)]$ in powers of $\mathbf{u}(l,\kappa)$ are [11,13]:

$$H_1 = \sum_{l,\kappa} \frac{\partial V}{\partial R_\alpha(l,\kappa)} u_\alpha(l,\kappa) \tag{108}$$

and

$$H_2 = \frac{1}{2} \sum_{l,\kappa,l',\kappa'} \frac{\partial^2 V}{\partial R_\alpha(l,\kappa)\partial R_\beta(l',\kappa')} u_\alpha(l,\kappa) u_\beta(l',\kappa') \tag{109}$$

where H_1 represents the electron-phonon interaction involving absorption or emission of one phonon, and H_2 represents the electron-phonon interaction involving absorption or emission of two phonons. The subscripts α, β denote Cartesian components which are summed when repeated. The adiabatic approximation allows the neglect of time

dependence of $\mathbf{u}(l, \kappa)$. To second order in $\mathbf{u}(l, \kappa)$ we obtain, in standard Rayleigh-Schrödinger perturbation theory [11,13]:

$$E_{kn}[u(l,\kappa)] = E_{k,n}(0) + \langle \mathbf{k},n|H_2|\mathbf{k},n\rangle + \sum{}' \frac{|\langle \mathbf{k}',n'|H_1|\mathbf{k},n\rangle|^2}{E_{k,n}(0) - E_{k',n'}(0) + i\Gamma} \qquad (110)$$

The first and second order correction terms to the unperturbed energy of the initial state $E_{kn}(0)$ are called "Debye-Waller" [14], and "Fan" terms [15,16], respectively. The Feynman diagram is shown in Figure 10. The Debye-Waller term is real. This term will

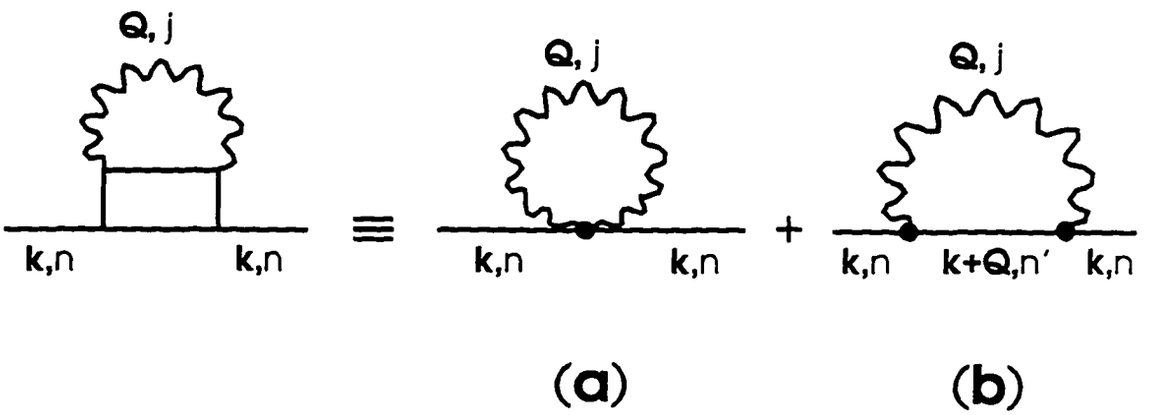

Figure 10. Self-energy graphs which give the temperature renormalization of the band energies to second order in atomic displacement. (a) represents the lowest-order Debye-Waller correction and (b) represents the Fan term.

not contribute to lifetime broadening. In the Fan terms the scattering process involves the electron-phonon interaction which induces transitions from initial state $|\mathbf{k}, n\rangle$ to intermediate state $|\mathbf{k}', n'\rangle$ and to initial state (see Figure 10b). This term not only

contributes to energy shift, but also to lifetime broadening. Equation (110) can be written as:

$$E_{kn}(T) = E_{kn}(0) + \Delta E_{kn} + i\Gamma(T) \tag{111}$$

where

$$\Delta E_{kn}(T) = \sum_j E(Q_j, |\mathbf{k},n\rangle) \left[n_{Qj}(T) + \frac{1}{2} \right] \tag{112}$$

and

$$\Gamma_{kn}(T) = \sum_j \Gamma(Q_j, |\mathbf{k},n\rangle) \left[n_{Qj}(T) + \frac{1}{2} \right] \tag{113}$$

where n_{Qj} is the Bose-Einstein occupation factor:

$$n_{Qj} = \frac{1}{\exp\left[\frac{\hbar\omega_{Qj}}{k_B T} \right] - 1} \tag{114}$$

whereas $E(Q_j, |\mathbf{k},n\rangle)$ is given by:

$$\begin{aligned} E(Q_j, |\mathbf{k},n\rangle) = & \frac{\hbar}{N} \sum \frac{\langle \mathbf{kn} | \partial V/\partial R_\alpha(\kappa) | \mathbf{k}+\mathbf{Qn}' \rangle \langle \mathbf{k}+\mathbf{Qn}' | \partial V/\partial R_\beta(\kappa') | \mathbf{kn} \rangle}{E_{kn}(0) - E_{k+Qn'}(0)} \\ & \times \exp[-iQ(\tau_\kappa - \tau_{\kappa'})] (M_\kappa M_{\kappa'})^{(-1/2)} \epsilon_\alpha(-Q_{j\kappa}) \epsilon_\beta(Q_{j\kappa'}) \\ & - \frac{\hbar}{2N} \sum \frac{\langle \mathbf{kn} | \partial V/\partial R_\alpha(\kappa) | \mathbf{kn}' \rangle \langle \mathbf{kn}' | \partial V/\partial R_\beta(\kappa') | \mathbf{kn} \rangle}{E_{kn}(0) - E_{kn'}(0)} \\ & \times [(M_\kappa M_{\kappa'} \omega_{Qj})^{-1} \epsilon_\alpha(-Q_{j\kappa}) \epsilon_\beta(Q_{j\kappa}) + (M_\kappa \omega_{Qj})^{-1} \epsilon_\alpha(-Q_{j\kappa'}) \epsilon_\beta(Q_{j\kappa'})], \end{aligned} \tag{115}$$

and $\Gamma(Q_j, |\mathbf{k},n\rangle)$ is given by:

$$\Gamma(Q_j, |\mathbf{k},n\rangle) = \frac{\pi\hbar}{N}\sum \langle \mathbf{kn}|\partial V/\partial R_\alpha(\kappa)|\mathbf{k}+\mathbf{Qn}'\rangle \langle \mathbf{k}+\mathbf{Qn}'|\partial V/\partial R_\beta(\kappa')|\mathbf{kn}\rangle \times \exp[-iQ(\tau_\kappa-\tau_{\kappa'})](M_\kappa M_{\kappa'}\omega_{Qj}^2)^{-1/2}\epsilon_\alpha(-Q_{j\kappa})\epsilon_\beta(Q_{j\kappa'})\delta[E_{\mathbf{kn}}(0) - E_{\mathbf{k}+\mathbf{Qn}'}(0)] \quad (116)$$

where M_κ is the mass of the atom κ located in the unit cell at position τ_κ, N is the number of unit cells in the crystal, $\hat{\epsilon}(Q_{j\kappa})$ is the polarization vector for the phonon Q_j of the atom κ. From the expression of $E(Q_j, |\mathbf{k},n\rangle)$, it is found that all wave vectors of phonons (acoustic as well as optical phonons) make a contribution to the temperature shift of the band gap.

In this model, phonon energies were neglected since they are very small compared to the energy of the electronic states. We are dealing only with direct band gap materials. In Eq.(116), there is a $\delta[E_{kn}(0)-E_{k+Q,n}(0)]$ function in the term $\Gamma(Q_j, |\mathbf{k},n\rangle)$. This δ-function means that only Q=0 phonons can contribute to the broadening, due to the conservation of energy. The maximum value of the phonon momentum Q_{max} is π/a_d with a_d being the lattice constant of the crystal, which is of the order of angstroms. Since the wavelength of a typical photon associated with the band gap of semiconductors ($\sim$1 eV) is of the order of 10^4 Å and $k=2\pi/10^4$ Å^{-1}, the photon momentum $k << Q_{max}$. It is obvious that in the process of interband transition induced by an absorption of photons, only small values (near Q=0) of phonon momentum are gained by electrons. From the dispersion curves, at near Q=0, the density of optical phonon modes are at a maximum, while the density of states of the acoustic phonon modes are very small. Therefore, mainly the optical phonons contribute to the broadening of the energy gap.

With this theoretical treatment, if a group of phonons of frequencies close to $k_B\Theta_B/\hbar$ [$k_B\Theta/\hbar$] yields the dominant contribution to $\Delta E_{kn}(T)$ [$\Gamma_{kn}(T)$], respectively, then we have:

$$\Delta E_{kn}(T) = a_B\left[1+\frac{2}{\exp(\frac{\Theta_B}{T})-1}\right] \tag{117}$$

and

$$\Gamma_0(T) = \Gamma_1\frac{2}{\exp(\frac{\Theta}{T})-1} \tag{118}$$

where

$$a_B=\frac{1}{2}\sum E(Q_j,|\mathbf{k},n\rangle),$$

and (119)

$$\Gamma_1=\frac{1}{2}\sum \Gamma(Q_j,|\mathbf{k},n\rangle).$$

To obtain the total shift and broadening at the critical point, the shift and broadening of the valence and conduction band states are added up, respectively. Therefore, we have the expressions for temperature dependence of energy gaps (E_g) due to electron-phonon interactions [3,17]:

$$E_g(T) = E_g(0)-\frac{2a_B}{\left[\exp(\frac{\Theta_B}{T})-1\right]} \tag{120}$$

where $E_g(0)$ corresponds the energy gap at $T=0$, a_B represents the average value of the

strength of electron-phonon coupling and $k_B\Theta_B/\hbar$ corresponds to average phonon frequency.

The temperature shift of E_g contains contributions from both thermal expansion and electron-phonon coupling effects [5,6]. Therefore, in order to obtain parameters directly related to the latter influence, it is necessary to eliminate the contribution of the former. The energy shift $\Delta E_{th}(T)$ due to the thermal expansion can be written as [6]:

$$\Delta E_{th}(T) = 3a\int_0^T \alpha(T')dT' \tag{121}$$

where a is the interband hydrostatic deformation potential and $\alpha(T)$ is the temperature-dependent linear-expansion coefficient.

Taking into account the thermal expansion contribution to $E_g(T)$ Eq.(120) can be rewritten as [6]:

$$E_g(T) - \Delta E_{th}(T) = E_g(0) - \frac{2a_B'}{\left[\exp(\frac{\Theta_B'}{T})-1\right]} \tag{122}$$

Similarly, the temperature dependence of the linewidth of the direct gap of zincblende-type semiconductors can be expressed as [18]:

$$\Gamma_0(T) = \Gamma_0(0) + \gamma_{AC}T + \frac{\Gamma_{LO}}{\left[\exp(\frac{\Theta_{LO}}{T})-1\right]} \tag{123}$$

where the first term of Eq.(123) is due to intrinsic effects (electron-electron interaction,

impurity, dislocation, and alloy scattering) at T=0 while the second term corresponds to lifetime broadening due to the electron-acoustical phonon interaction, where γ_{AC} is the acoustical phonon coupling constant. The third term is caused by the electron (exciton)-LO phonon (Fröhlich) interaction. The quantity Γ_{LO} represents the strength of the electron (exciton)-LO phonon coupling while Θ_{LO} is the Q=0 LO phonon temperature.

Equations (120) and (123) are based on a microscopic approach. They can be used to model the measured temperature dependence data of transition energies and the broadening parameters to obtain important information about electron-phonon interaction.

3.2.2 Varshni Formulation

The temperature variation of $E_g(T)$ can also be described by equations involving three parameters such as the semi-empirical Varshni expression [7]:

$$E_g(T) = E_g(0) - \frac{\alpha T^2}{\beta + T} \tag{124}$$

where α, β are the Varshni parameters.

In order to obtain parameters directly related to the influence of electron-phonon coupling effects, it is again necessary to eliminate the contribution of the temperature shift of E_0 due to thermal expansion from Eq.(124). After taking of the thermal expansion contribution, Equation (124) can be rewritten as:

$$E_g(T) - \Delta E_{th}(T) = E_g(0) - \frac{\alpha' T^2}{\beta' + T} \tag{125}$$

3.3 Experiment

3.3.1 Experimental Details

The ZnSe and ZnCdSe layers were grown by MBE on GaAs(100) and InP(100) substrates, respectively, resulting in near-lattice-matched structures. The desorption of the native oxide on the substrate was carried out under an As flux. Growth was performed using elemental sources, under excess group VI flux. The growth temperature was 270° C. However, the growth of ZnCdSe/InP required that initial growth be performed at low temperature (170° C) during one minute in order to obtain 2D nucleation. The thickness of ZnCdSe epitaxial layer was 6000 Å. The zinc composition of 56% was determined from the low-temperature (5K) band gap data extracted from the composition dependence of the photoluminescence [2]. The details of the CER method, which utilizes a condenser-like system, have already been described [19]. An ac modulating voltage ($\approx$1 kV peak-to-peak) at frequency 200 Hz was employed. The temperature was measured by a thermocouple in contact with the sample surface.

3.3.2 Experimental Results

Plotted by the opened circles in Figure 11 are the experimental CER spectra of the $Zn_{0.56}Cd_{0.44}Se$ sample at 26K, 231K and 383K. Spectral ellipsometry measurements of the dielectric constants shows a sharp excitonic feature for E_0 even at room temperature for both the ZnCdSe [20] and ZnSe [20,21] epilayers. The solid lines in Figure 11 are least-square fits to the FDGP, which is appropriate for an excitonic transition [19]. The obtained values of the energies are designated by arrows in the

figure. Similar results have been obtained for $E_0(T)$ of ZnSe [22].

Plotted by the open squares in Figure 12 and Figure 13 are the experimental values of $E_0(T)$ for $Zn_{0.56}Cd_{0.44}Se$ and ZnSe, respectively. Representative error bars are shown. As it was mentioned before, since the temperature shift of E_0 contains contributions from both thermal expansion and electron-phonon coupling effects [5,6], therefore, in order to obtain parameters directly related to the latter influence, it is necessary to eliminate the contribution of the former. The energy shift $\Delta E_{th}(T)$ due to the thermal expansion is given by Eq.(121) [6]. For ZnSe we have used values of a (-5.4 eV) and $\alpha(T)$ for from Refs. [23] and [24], respectively. For the ZnCdSe a value of a = -4.5 eV was obtained from a linear interpolation between the hydrostatic pressure coefficient of ZnSe and the lowest lying exciton (A-exciton) of wurtzite CdSe [24]. Since we found no data for $\alpha(T)$ for CdSe the ZnSe values of this parameter were used for the alloy. Shown by the solid squares in Figure 12 and Figure 13 are $E_0(T)$-$\Delta E_{th}(T)$ for ZnCdSe and ZnSe, respectively.

The temperature dependence of the direct band gap can be described by a Bose-Einstein-type expression of Eq.(120) [3] and was rewritten as Eq.(122), where the thermal expansion contribution to $E_0(T)$ is taken into account. Shown by the dashed and solid lines in Figure 12 and Figure 13 are least-square fits to Eqs.(120) and (122), respectively. The obtained values of the various parameters are given in Table I. For comparison purposes we also have listed in Table I numbers for some of these parameters for the direct gaps of CdSe (A-exciton) [25], InP [17,26], GaAs [3], $In_{0.06}Ga_{0.94}As$ [6], $In_{0.15}Ga_{0.85}As$ [6] and Ge [27].

Our data have also been fit to the Varshni semiempirical relationship of Eq.(124) and (125) [7]. The obtained values of $E_0(0)$, α, α', β and β' for ZnSe and ZnCdSe are listed in Table II. Also shown in Table II values for some of these parameters for the direct gaps of CdSe (A-exciton) [25], InP [26], GaAs [3,28], $In_{0.06}Ga_{0.94}As$ [6], $In_{0.15}Ga_{0.85}As$ [6] and Ge [24].

The experimental values of the temperature dependence of the linewidth $\Gamma_0(T)$ [half width at half maximum (HWHM)] of the direct gap for the $Zn_{0.56}Cd_{0.44}Se$ and ZnSe samples, as obtained from the lineshape fit, are displayed by the solid circles in Figure 14 and Figure 15, respectively. Representative error bars are shown.

The temperature dependence of the linewidth of the direct gap of zincblende-type semiconductors is expressed by Eq.(123) [18]. As the temperature is raised, the linewidth first increases from it zero temperature value because of acoustical phonon scattering. Above about 60K-70K the LO phonon contribution becomes important and eventually dominates the linewidth. Because of the error bars on our data it was necessary to fix the parameters γ_{AC} and Θ_{LO} in order to obtain the two significant quantities $\Gamma_0(0)$ and Γ_{LO} by means of a least-square fit. The values for γ_{AC} and Θ_{LO} for ZnSe and ZnCdSe (linear interpolation between ZnSe and CdSe) were taken from Ref. [18].

The solid lines in Figure 14 and Figure 15 are least-square fits to Eq.(123) which made it possible to evaluate $\Gamma_0(0)$ and Γ_{LO} for the ZnCdSe and ZnSe samples, respectively. The obtained values of these quantities as well as the numbers for γ_{AC} and Θ_{LO} are listed in Table III. In Figure 14 we also have shown the individual contributions

of the acoustical (dotted line) and LO (dashed) phonons to the total broadening. For comparison we also have displayed in Table III values of Γ_{LO} (in terms of HWHM) for ZnSe [18,29], CdSe (A-exciton) [25], GaAs [3,30-32], $In_{0.06}Ga_{0.94}As$ [6] and $In_{0.15}Ga_{0.85}As$ [6] from other works. Also shown is the parameter related to the broadening of the direct gap of Ge [27]. In this case the interaction is with the $\Gamma - L$ longitudinal acoustical phonon. With the exception of Ref. [30] all previous investigations of $\Gamma_0(T)$ have neglected the acoustical phonon term in the interpretation of the data.

For energy gaps, temperature variations are due to both lattice constant variations and interactions with relevant acoustic and optical phonons. According with the existing theory [3-5] this leads to a value of Θ_B (Θ'_B) significantly smaller than Θ_{LO}. From Tables I and III, it can be seen that our observations are in a good agreement with this theoretical consideration. Also from Tables I and II the trend with alloy composition for the parameters a_B and α are quite reasonable, i.e., the addition of the CdSe makes these values for the alloy smaller than for the binary ZnSe. Also the values of a'_B for the II-VI materials ZnSe and ZnCdSe are larger than for the III-V and group IV semiconductors. This is probably due to the enhanced optical phonon interaction with ionicity.

The parameter α' of Eq.(125) can be related to a'_B and Θ'_B of Eq.(122) by taking the high temperature limit of both expressions. This yields $\alpha' = 2a'_B/\Theta'_B$. Comparison of Tables I and II shows that this relation is indeed satisfied.

Manoogian and Woolley [33] have suggested that after the thermal expansion term

is removed the parameter β' of Eq.(125) is directly proportional to the Debye temperature Θ_D by the relation $\beta' = (3/8)\Theta_D$. For ZnSe and ZnCdSe (linear interpolation between ZnSe and CdSe) Θ_D = 339K and 291K, respectively [24]. Therefore, from Table II for these materials this relation does not hold, in contrast to the results for $In_{0.06}Ga_{0.94}As$ and $In_{0.15}Ga_{0.85}As$ [6].

Our values for Γ_{LO} for ZnSe and ZnCdSe are consistent with the value for this parameter reported for CdSe [25]. References [18] and [29] have given somewhat larger numbers for this quantity for ZnSe but no data was presented. Also our value of this parameter for ZnSe is considerably smaller than the theoretical result (35 meV) of Ref. [18]. There seems to be some ambiguity with regard to ionicity trends. The Fröhlich interaction should be stronger for II-VI materials in relation to III-V semiconductors, as clearly indicated in the theoretical work of Ref. [18]. However this trend is not apparent from the results listed in Table III. Gammon et al have recently reported an experimental and theoretical value of $\Gamma_{LO} \approx 8$ meV for GaAs [32]. This number is considerably smaller than the experimental value of Ref. [30] (23 meV) and the theoretical value (21 meV) of Rudin et al. [18] Gammon et al have suggested that the theoretical results of Ref. [18] may be in error since certain interactions were not taken into account properly. Therefore, more work is needed in both experiment and theory in order to clarify this situation.

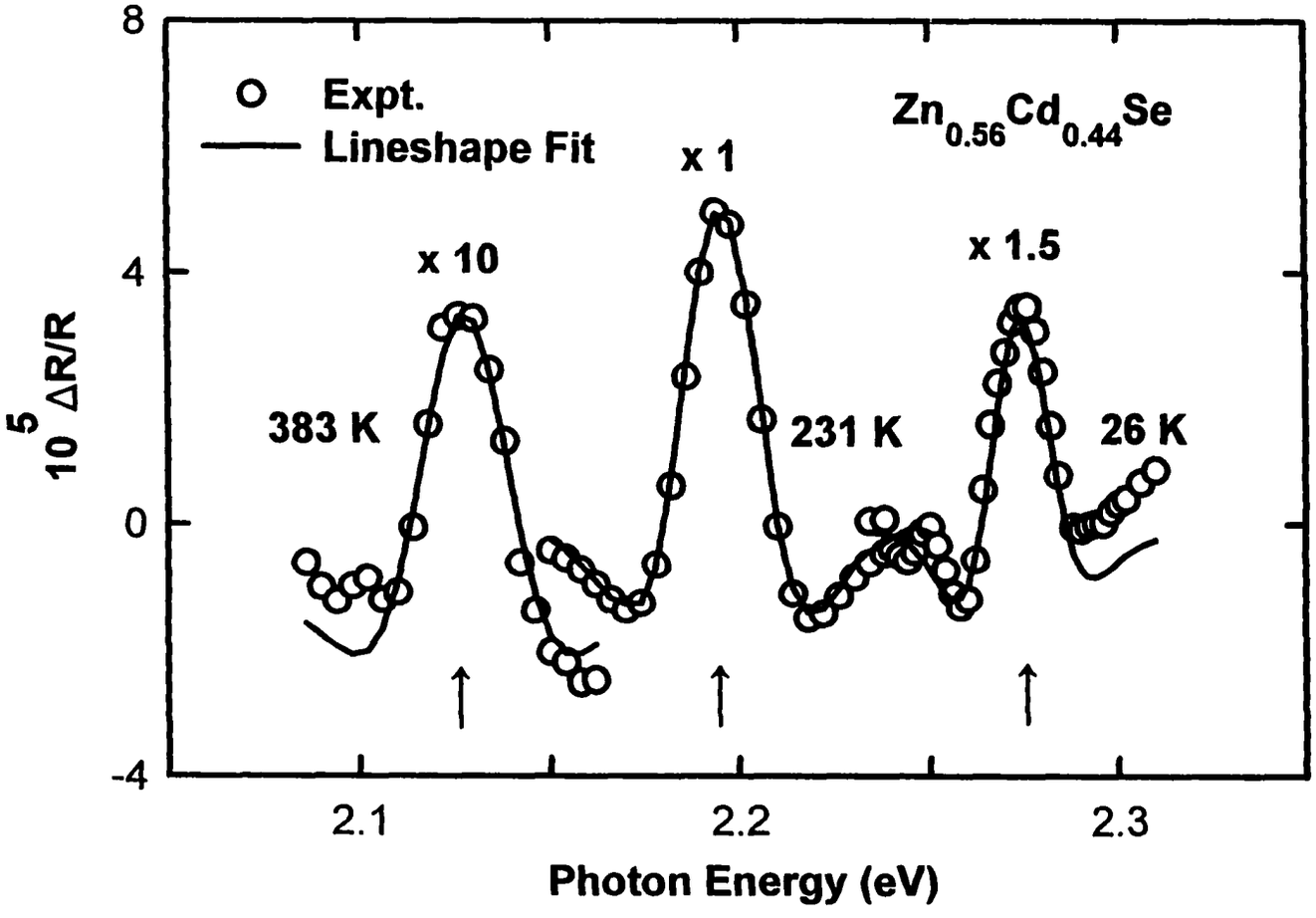

Figure 11. Experimental CER spectra of the direct gap of $Zn_{0.56}Cd_{0.44}Se$ (open circles) at 383K, 231K and 26K. The solid lines are fits to a first-derivative of a Gaussian profile. The obtained values of the energies are indicated by the arrows.

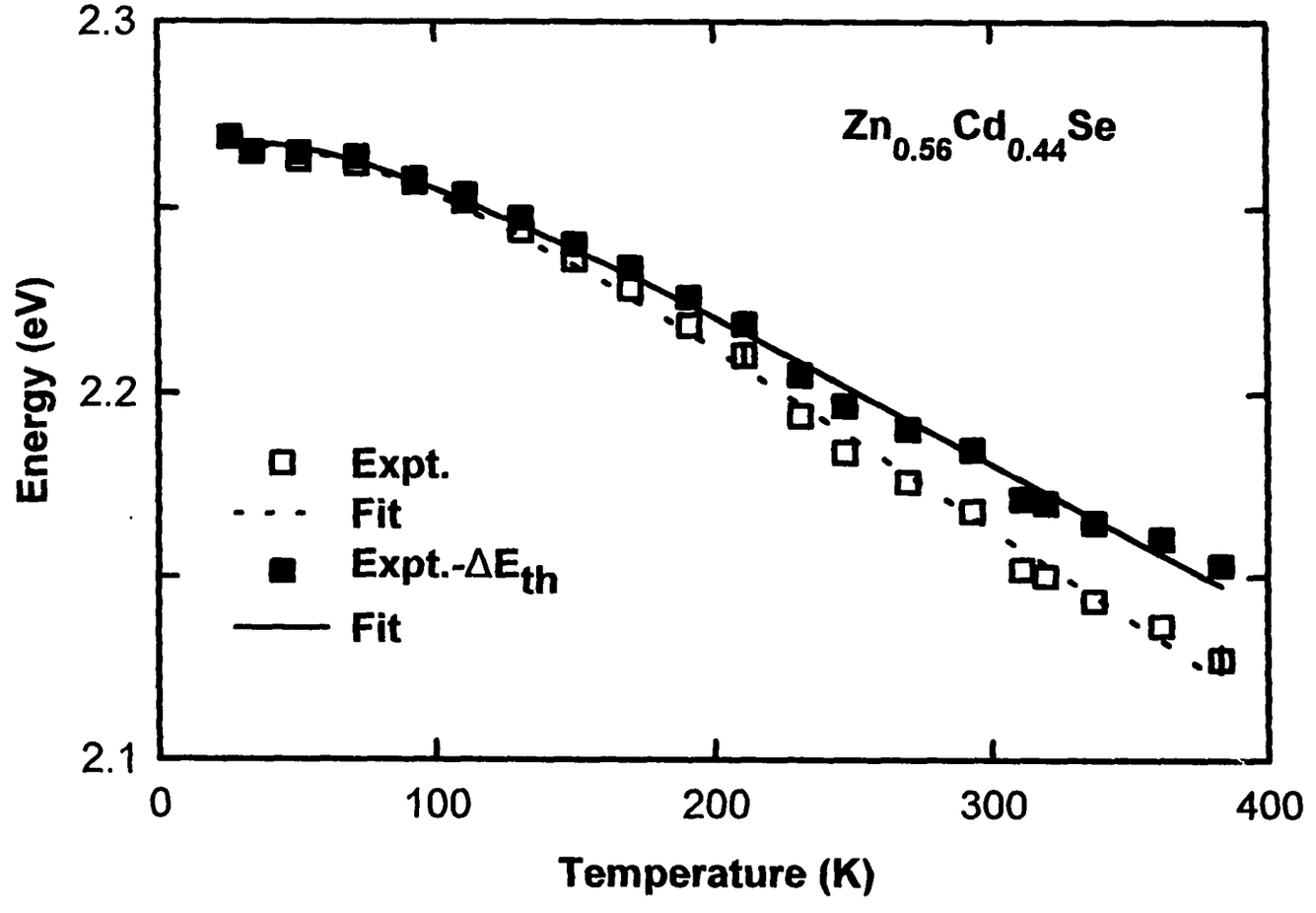

Figure 12. The experimental temperature dependence of the direct gap of $Zn_{0.56}Cd_{0.44}Se$ (open squares). The closed squares are the data minus the thermal expansion contribution, $\Delta E_{th}(T)$. The dashed and solid lines are least-square fits to Eqs.(120) and (122), respectively.

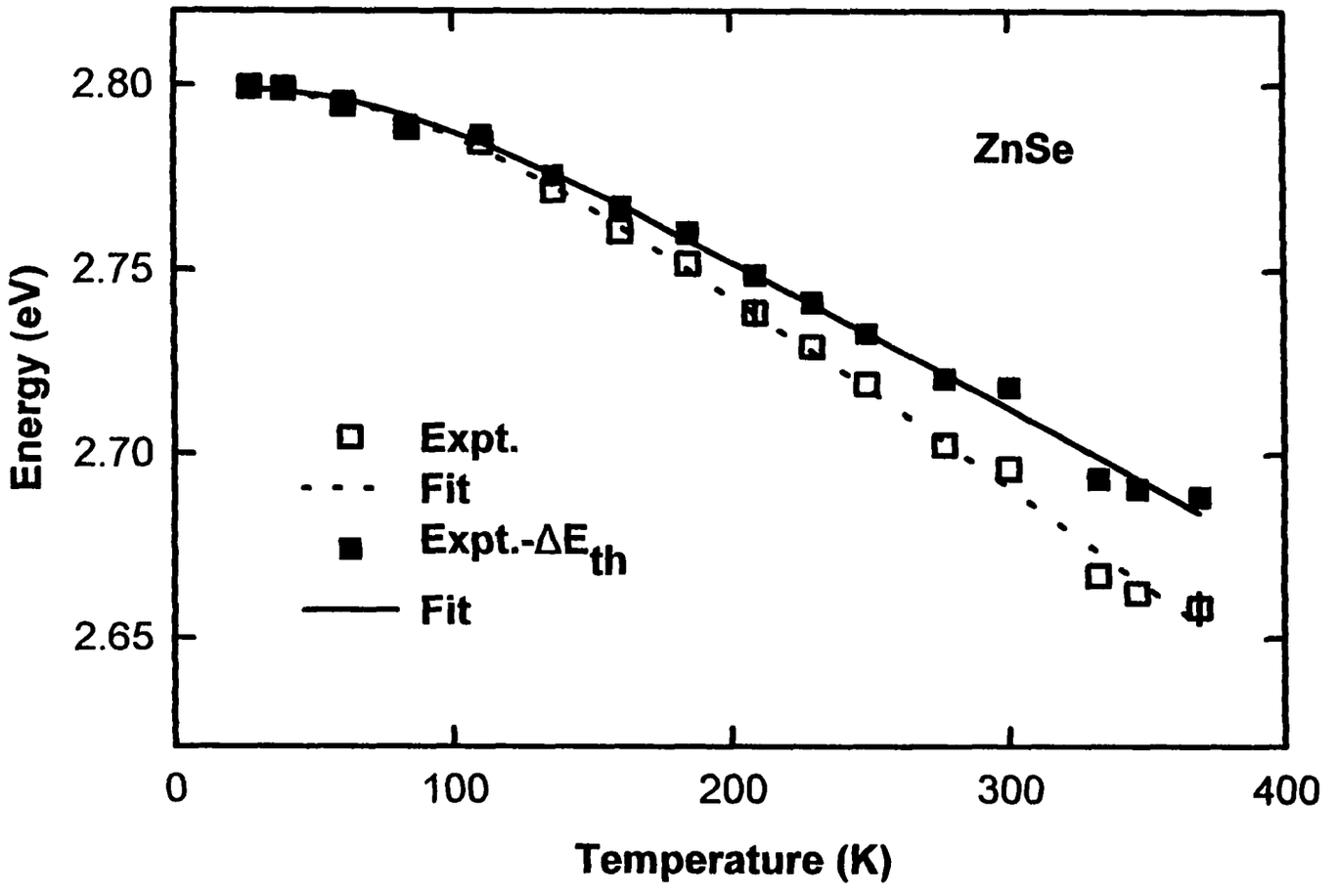

Figure 13. The experimental temperature dependence of the direct gap of ZnSe (open squares). The closed squares are the data minus the thermal expansion contribution, $\Delta E_{th}(T)$. The dashed and solid lines are least-square fits to Eqs.(120) and (122), respectively.

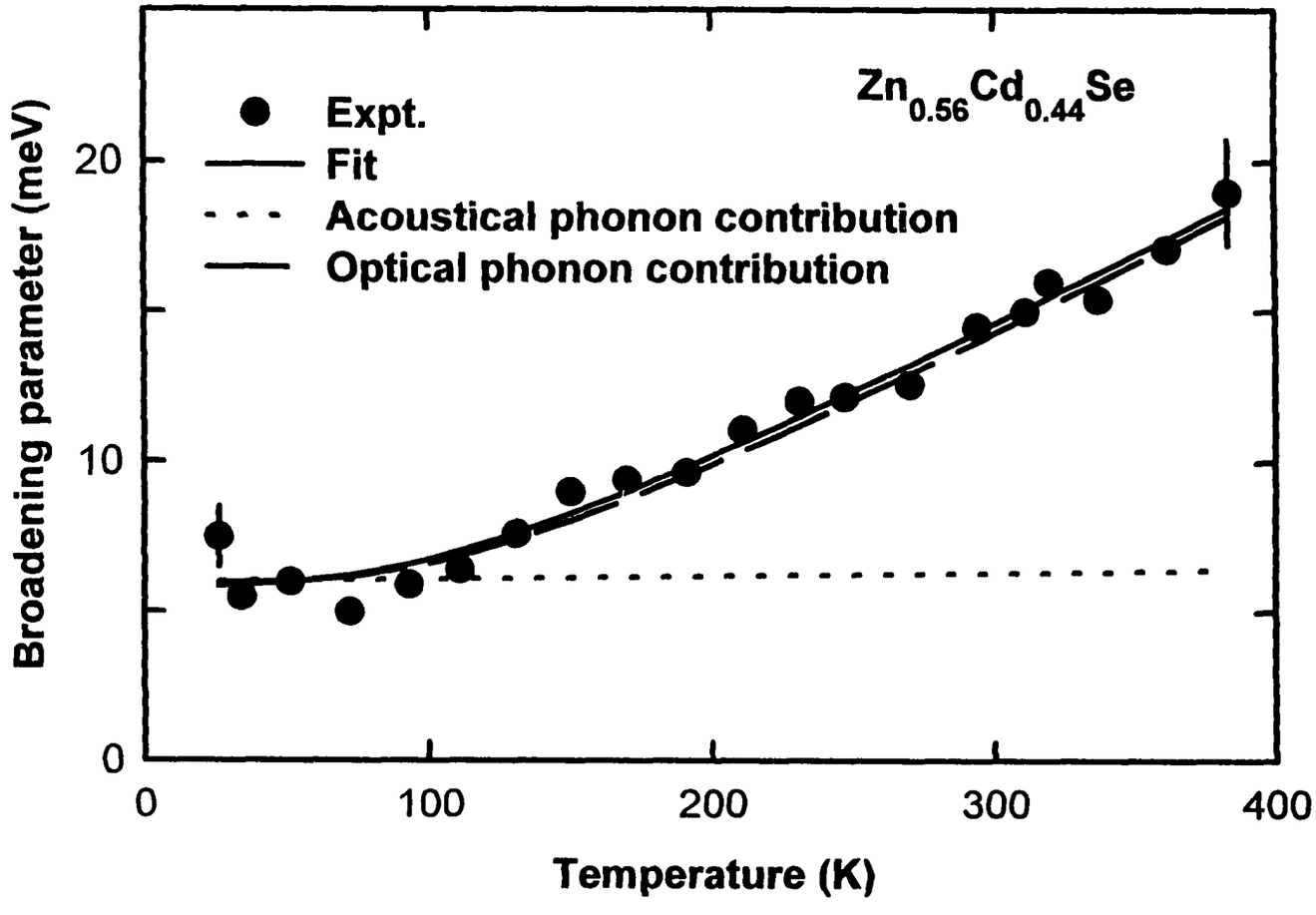

Figure 14. Experimental variation of the broadening parameter (HWHM) for the direct gap of $Zn_{0.56}Cd_{0.44}Se$ (closed circles). The solid line is a least-square fit to Eq.(123). The dotted and dashed curves show the individual contributions of the acoustical and LO phonons, respectively, to the total broadening.

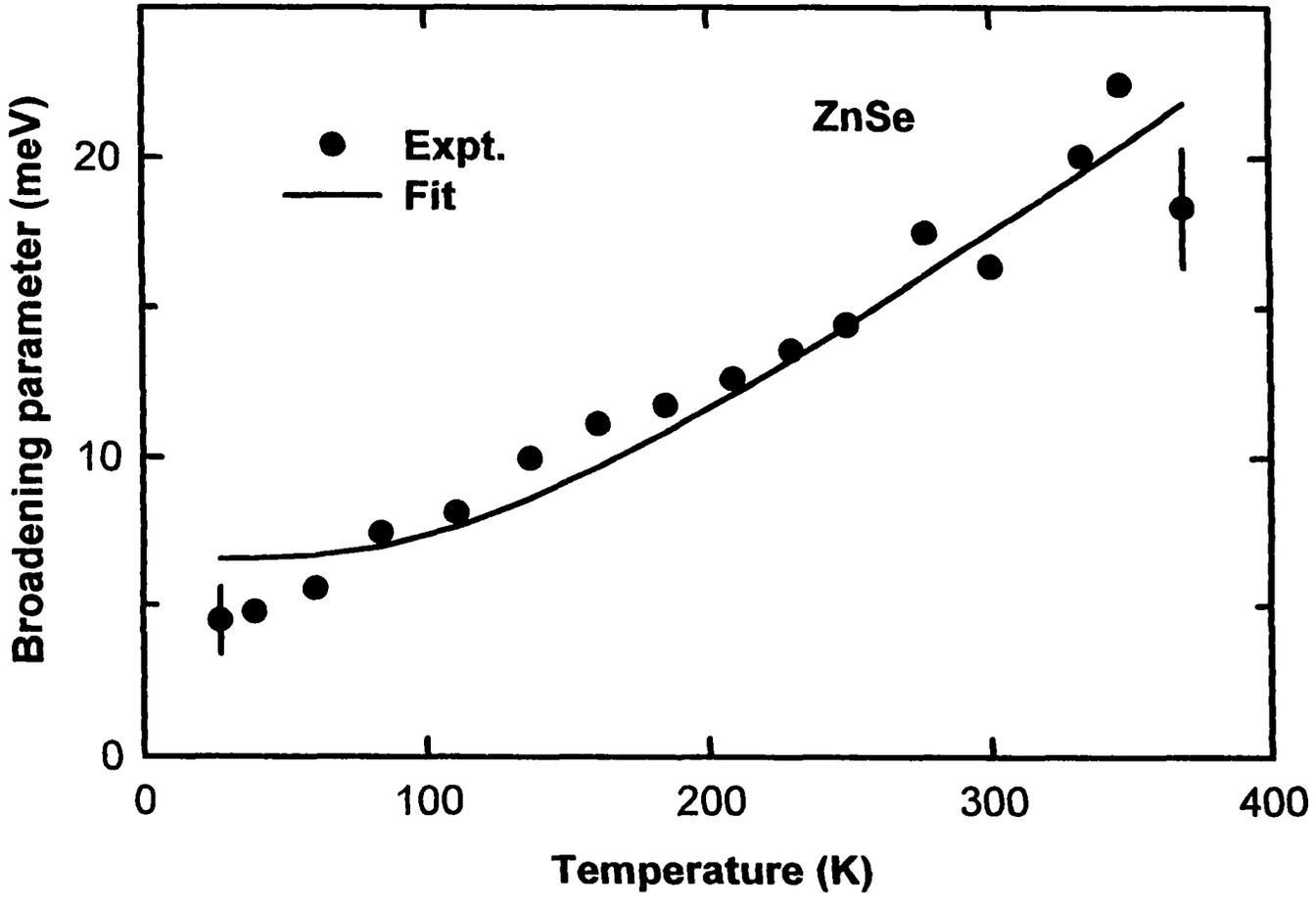

Figure 15. Experimental variation of the broadening parameter (HWHM) for the direct gap of ZnSe (closed circles). The solid line is a least-square fit to Eqs.(123).

TABLE I. Values of the Bose-Einstein-type fit parameters which describe the temperature dependence of the direct band gaps of ZnSe and $Zn_{0.56}Cd_{0.44}Se$ obtained in this experiment. For comparison purposes the relevant parameters for CdSe (A-exciton), InP, GaAs, $In_{0.06}Ga_{0.94}As$, $In_{0.15}Ga_{0.85}As$ and Ge also are listed.

Material	$E_0(0)$ (eV)	a_B (meV)	Θ_B (K)	a_B' (meV)	Θ_B' (K)
ZnSe	2.800±0.005	73±4	260±10	47±4	220±10
$Zn_{0.56}Cd_{0.44}Se$	2.267±0.004	62±4	236±10	43±4	201±10
CdSe[a]	1.830 (5)	36 (5)	179 (40)		
InP	1.423±0.01[b] 1.421 (111)[c]	51±2[b] 217[c]	259±10[b] 697 (117)[c]		
GaAs[d]	1.512±0.005	57±29	240±102		
$In_{0.06}Ga_{0.94}As$[e]	1.420±0.005	44±9	203±45	33±7	280±45
$In_{0.15}Ga_{0.85}As$[e]	1.285±0.005	53±10	238±50	39±8	300±50
Ge[f]	0.8853±0.002[g] 0.8836±0.003[h]	70±10[g] 65±15[h]	302±35[g] 290±45[h]	36±5[g] 34±10[h]	255±35[g] 255±46[h]

(a) Ref. 25. The numbers in parentheses are error margins in units of the last significant digit; (b) Ref. 26; (c) Ref. 17. The numbers in parentheses are error margins in units of the last significant digit; (d) Ref. 3; (e) Ref. 6; (f) Ref. 27; (g) Band-to-band transition; (h) Excitonic transition.

TABLE II. Values of the Varshni-type fit parameters which describe the temperature dependencies of the direct energy band gaps of ZnSe and $Zn_{0.56}Cd_{0.44}Se$ obtained in this experiment. For comparison purposes the parameters for CdSe (A-exciton), InP, GaAs, $In_{0.06}Ga_{0.94}As$, $In_{0.15}Ga_{0.85}As$ and Ge also are listed.

Material	$E_0(0)$ (eV)	α (10^{-4}eV/K)	β (K)	α' (10^{-4}eV/K)	β' (K)
ZnSe	2.800±0.005	7.3±0.4	295±35	5.0±0.4	206±35
$Zn_{0.56}Cd_{0.44}Se$	2.272±0.004	6.1±0.5	206±35	4.5±0.5	153±45
CdSe[a]	1.834 (3)	4.24 (20)	118 (40)		
InP[b]	1.432±0.007	4.1±0.3	136±60		
GaAs	1.512±0.005[c] 1.517 (8)[d]	5.1±0.5[c] 5.5 (1.3)[d]	190±82[c] 225 (174)[d]		
$In_{0.06}Ga_{0.94}As$[e]	1.420±0.005	4.8±0.4	200±50	2.5±0.4	140±40
$In_{0.15}Ga_{0.85}As$[e]	1.285±0.005	5.0±0.4	231±40	2.6±0.4	150±40
Ge[f]	0.885±0.002[g] 0.884±0.003[h]	6.5±0.7[g] 8.2±1.0[h]	410±100[g] 590±150[h]	3.5±0.5[g] 3.9±0.7[h]	290±80[g] 370±120[h]

(a) Ref. 25. The numbers in parentheses are error margins in units of the last significant digit; (b) Ref. 26; (c) Ref. 28; (d) Ref. 3. The numbers in parentheses are error margins in units of the last significant digit; (e) Ref. 6; (f) Ref. 27; (g) Band-to-band transition; (h) Excitonic transition.

TABLE III. Values of the parameters which describe the temperature dependence of the broadening parameter (in terms of HWHM) for the energy gaps of $Zn_{0.56}Cd_{0.44}Se$ and ZnSe. For comparison purposes the phonon coupling parameters for ZnSe, CdSe, GaAs, $In_{0.06}Ga_{0.94}As$, $In_{0.15}Ga_{0.85}As$ and Ge from other works also are listed.

Material	$\Gamma_0(0)$ (meV)	Γ_{LO} (meV)	Θ_{LO} (K)	γ_{AC} (μeV/K)
ZnSe	6.5±2.5	24±8 30±7[c] 30[d]	360[a]	2.0[a,b]
$Zn_{0.56}Cd_{0.44}Se$	6.0±2.0	17±6	334[a]	1.1[a]
CdSe[e]	2.3 (3)	23 (1)	300[a]	
GaAs		23±1.5[f] 8.2[g] 7[h] 46 (58)[i]	417[a] 417[a] 417[a] 337 (259)	7[a]
$In_{0.06}Ga_{0.94}As$[j]	7.5±0.5	23±6	370±122	
$In_{0.15}Ga_{0.85}As$[j]	10.5±0.5	23±6	380±120	
Ge[k]	1.06±0.15[l] 3.30±0.35[m]	4.2±0.8[l] 4.0±1.2[m]	324[a] 324[a]	

(a) Parameter fixed; (b) In Ref. 22 γ_{AC} was taken to be 7 μeV/K; (c) Ref. 18; (d) Ref. 29. In this paper the listed value of Γ_{LO} = 70 meV is in terms of the full width at half maximum; (e) Ref. 25. The numbers in parentheses are error margins in units of the last significant digit; (f) Ref. 30; (g) Ref. 32; (h) Ref. 31; (i) Ref. 3. The numbers in parentheses are error margins in units of the last significant digit; (j) Ref. 6; (k) Ref. 27. The relevant phonon is the Γ - L longitudinal acoustical phonon; (l) Band-to-band transition; (m) Excitonic transition.

Chapter 4. QUANTUM WELLS AND QUANTUM WELL LASERS

4.1 Quantum Well Structures

An extremely significant development in semiconductor research has been the fabrication of synthetic semiconductor microstructures such as QWs and HJs. These structures can be grown by a variety of thin film epitaxial techniques such as MBE, MOCVD, gas phase MBE, etc. They can be composed of ultrathin layers of thicknesses varying from several atomic layers to several hundred Å (typical thickness $\sim$100Å) of alternating composition (e.g., GaAs/$Ga_{1-x}Al_xAs$, $In_xGa_{1-x}As$/GaAs), of alternating doping (e.g., n-GaAs/p-GaAs), or a combination of alternating composition plus doping. Heterointerfaces can be either lattice-matched (e.g., GaAs/$Ga_{1-x}Al_xAs$) or strained layer (e.g., $In_xGa_{1-x}As$/GaAs). These artificial materials produce a 1D potential along the growth (z) direction such that the electronic bands of the bulk are split into quasi 2D quantized subbands.

A SQW is produced by fabricating a thin layer (L_z) of a semiconductor A with band gap E_g^A (e.g., GaAs) sandwiched between two thick layers of material B with band gap $E_g^B > E_g^A$ (e.g., $Ga_{1-x}Al_xAs$). One of the most important issues when two semiconductors are brought together abruptly to form an interface is how the bandedges of two materials line up at the interface. Generally several possibilities could exist. The electrons and holes can have the same spatial confinement (type I heterostructures) or electrons can be localized in material A and the holes in semiconductor B (type II

heterostructures). The materials A and B can be either lattice-matched (e.g., GaAs/GaAlAs) or strained layer (InGaAs/GaAs). The valence quantum potential removes the heavy- (HH) and light-hole (LH) degeneracy of cubic materials such as diamond- and zincblende-type semiconductors. Also, strain alters band structure by moving HH and LH bands relative to the unstressed valence band. This generally can change the type of the spatial confinement.

QW laser structures employ complex sequences of thin layers of single crystal materials, where a few light-emitting QWs are embedded in waveguide regions and enclosed by *p*- and *n*-doped confining layers. Analysis of the active region, buried under much thicker layers, is difficult after the sequence of layers is completed. Commonly photoluminescence (PL) and electroluminescence are used to analyze the positions of energy levels and quality of the wells. During their lifetime, however, excited electrons and holes may migrate to defects or to wider portions of the wells and the emission spectrum may not be representative of the sample. More direct access to the density of states by absorption is difficult since the absorption of light by a few wells buried under thick conducting layers may be too weak to be resolved.

In spite of the proven utility of PR and CER in evaluating device structures, to date little work has been performed on QW laser structures. Low temperature (19K) electroabsorption (EA) measurements have been performed on InGaAs/InGaAsP QW lasers grown lattice matched on InP substrates [1]. A comprehensive study comparing lasing frequency with room temperature PR and PL has been performed for 24 samples of $Ga_{0.9}Al_{0.09}As/Ga_{0.6}Al_{0.4}As/Ga_{0.2}Al_{0.8}As$ QW lasers [2]. Moneger et al have reported a

room temperature CER study on a InGaAs/GaAs/GaAlAs VCSEL structure [3] while Berger et al have performed a PR study of the GaAs/GaAlAs VCSEL system [4]. Amirtharaj has reported double modulation and selective excitation PR for characterizing QW laser structures [5] and Chandler-Horowitz et al have investigated a GaInP/AlGaInP/AlInP SQW laser structure using the double beam modulation PR technique to eliminate the PL background often encountered in PR [6]. Krystek et al have recently performed a room temperature CER study of a pseudomorphic InGaAs/GaAs/InGaP 0.98 μm laser structure [7].

In this chapter we report a room temperature CER study of a pseudomorphic InGaAs/GaAs/GaAlAs 0.98 μm GRINSCH laser configuration. These structures are of considerable interest as pumping sources for both Erbium-doped optical fiber amplifiers [8] and solid state lasers. CER, which uses no pump beam, was employed to eliminate PL problems and also to minimize the amount of light on the sample and hence any photovoltaic effects. Signals were detected from the InGaAs SQW, GaAs inner cladding layers and GaAlAs graded regions of the sample. Six quantum transitions were observed from the InGaAs SQW section including *11H*, which is closely related to the lasing frequency. The notation $\tilde{m}\tilde{n}H(L)$ denotes an intersubband transition between the $\tilde{m}^{th}$ conduction and $\tilde{n}^{th}$ HH(LH)-like valence subbands. From a comparison of the energies of these SQW features with an envelope function calculation, including the effects of strain and the electric field, the In composition and width of the SQW (L_W) were evaluated [9] . The derivative nature of the spectrum and the narrow linewidth made it possible to easily determine the energy position of *11H* to less than ± 1 nm at room

temperature. From the period of the observed FKOs from the graded GaAlAs region we directly evaluated the built-in electric field in the structure.

4.2 Envelope Function Approximation in Semiconductor Microstructures

The quantum levels in semiconductor microstructures can be calculated in a number of ways. The simplest and most frequently used methods are based on the envelope function approximation [10,11].

In the one-electron approximation, the Schrödinger equation for the motion of an electron in an unperturbed crystal is:

$$H_0\psi_{nk}(\mathbf{r}) = E_n(\mathbf{k})\psi_{nk}(\mathbf{r}) \tag{126}$$

where n is the band index, $\mathbf{k}$ is the in-plane wave vector which is restricted to the first Brillouin zone, H_0 is the one-electron Hamiltonian of the crystal with a periodic potential V(r):

$$H_0 = \left[-\frac{\hbar^2}{2m_0} \right] \nabla^2 + V(\mathbf{r}) \tag{127}$$

where $\psi_{nk}(\mathbf{r})$ is the Bloch function with energy eigenvalue $E_n(\mathbf{k})$, and

$$\psi_{nk}(\mathbf{r}) = u_{nk}(\mathbf{r})e^{i\mathbf{k}\cdot\mathbf{r}} \tag{128}$$

where $u_{nk}(\mathbf{r})$ is a periodic function with the periodicity of the crystal lattice.

In the presence of some perturbation potential $U(\mathbf{r})$, the Schrödinger equation of the system becomes:

$$[H_0 + U(\mathbf{r}) - E]\Psi(\mathbf{r}) = 0 \tag{129}$$

where E is the energy, and $\Psi(\mathbf{r})$ is the one-electron wave function. $U(\mathbf{r})$ is assumed to be slowly varying compared to the crystal periodicity. When $U(\mathbf{r})=0$ Eq.(129) reduces to Eq.(126). Assuming that the energy eigenvalues $E_n(\mathbf{k})$ and the Bloch wave functions $\psi_{n\mathbf{k}}(\mathbf{r})$ are given, it can be shown that [12,13], if:

(a) $U(\mathbf{r})$ is slowly varying on the scale of the lattice parameter a_d of the semiconductor, i.e., its Fourier transform $U(\mathbf{k})$ is appreciably non-zero only in a region around $\mathbf{k}=\mathbf{0}$ of extension Δk, with $\Delta k \ll 2\pi/a_d$,

(b) $U(\mathbf{r})$ is weak, i.e., $|\langle\psi_{n\mathbf{k}}|U|\psi_{n'\mathbf{k}}\rangle| \ll |E_n(0)-E_{n'}(0)|$ $(n \neq n')$,

(c) we are considering eigenvalues in the neighborhood of a simple parabolic band edge n, well separated from all others. At $\mathbf{k}\simeq 0$:

$$E_n(\mathbf{k}) = E_n(0) + \frac{\hbar^2 k^2}{2m^*} \tag{130}$$

where m* is the effective mass of the electron (or hole), then the problem of Eq.(129) can be reduced to solving the following effective-mass equation:

$$\left[-\frac{\hbar^2}{2m^*}\nabla^2 + U(\mathbf{r})\right]\varphi(\mathbf{r}) = [E-E(0)]\varphi(\mathbf{r}), \tag{131}$$

$$\Psi(\mathbf{r}) = \varphi(\mathbf{r})u_0(\mathbf{r}) \tag{132}$$

where $\varphi(\mathbf{r})$ is the so-called envelope function.

As can be seen from Eqs.(131)-(132), the unperturbed properties of the bulk semiconductor enter the calculation via two parameters: the effective mass m* and the

band edge energy $E_n(0)$. Eq.(132) shows that the wave function in the presence of $U(\mathbf{r})$ is a slowly varying "envelope" function modulating the rapidly varying unperturbed Bloch function.

Semiconductor microstructures in general contain more than one constituent material. Assuming the growth direction to be along the z-axis, the effective masses and band gaps will vary as a function of z. The z-dependent $E_n(0)$ can be considered as $U(\mathbf{r})$, i.e., $U(\mathbf{r})=E_n(0,z)$. Depending on how the bands in the host materials are lined up, such potentials for a specific pair of conduction-valence bands (for example, the electron-HH bands) in the microstructure may have either a type I profile, which means the potentials for electrons and holes have their minimum values in the same layer of material, or a type II profile, which means the electrons and holes have their minimum potentials in different host layers. Shown in Figure 16 is an illustration of the two types of potential profile in the case of a QW.

In the case of semiconductor microstructures Eq.(131) is generalized to read:

$$\left[-\frac{\hbar^2}{2}\frac{d}{dz}\left(\frac{1}{m^*(z)}\frac{d}{dz}\right)+E_n(0,z)\right]\varphi_{n,s}(z) = E_s\varphi_{n,s}(z), \qquad (133)$$

where the index s is used to label the quantized levels of envelope function φ_n. The kinetic energy term in Eq.(133) has been rewritten, for a z-dependent mass, in a way which restores the Hermitian character of the Hamiltonian [14,15]. The boundary conditions at the heterointerfaces are given by:

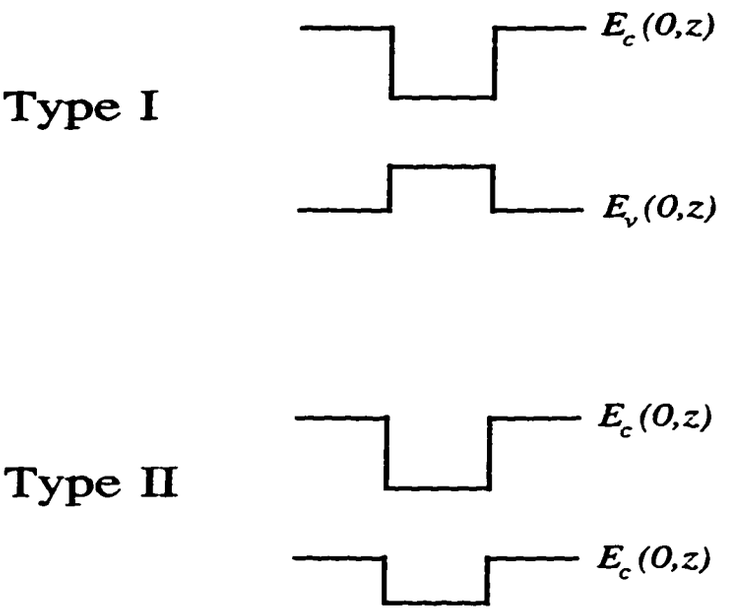

Figure 16. Illustration of type I and II potential profiles in the case of a quantum well.

$$\varphi_{n,s}(z) \text{ continuous at interface,}$$
$$\frac{1}{m^*}\frac{\partial \varphi_{n,s}(z)}{\partial z} \text{ continuous at interface} \tag{134}$$

These boundary conditions require that the periodic factor u_{n0} of the Bloch wave function on both sides of the heterointerface be approximately the same, and ensure the current

density conservation. Eqs.(133) and (134) serve as the starting point for the calculation methods to be discussed in this section. Their solutions give a series of subband energy levels E_s, s=1,2..., and the wave (envelope) functions φ of the relevant levels. Eq.(133) and the boundary conditions Eq.(134) are also known as the Ben-Daniel-Duke model.

For an infinite potential well, only confined transitions (CT) between the $\tilde{m}^{th}$ conduction and $\tilde{n}^{th}$ valence subbands with $\tilde{m} \equiv \tilde{n}$ are allowed ("symmetry-allowed" transitions). This is a consequence of the nodal structure at the interface and the simple relationship between the number of nodes in the wavefunction and the energy of that state. For finite wells, there is no longer a node at the interface and hence "symmetry-forbidden" but "parity allowed" features with $\tilde{m}=\tilde{n}\pm2, \pm4$, etc. may be observed, although they are generally weak. The presence of transitions with $\tilde{m}=\tilde{n}\pm1, \pm3$, etc., may be induced by electric fields.

4.3 Strain Effects on the Biaxially Compressed InGaAs/GaAs SQW System

4.3.1 Introduction

Strain has very significant effects on the electronics states of semiconductor materials [16-18]. It produces changes in the lattice parameter and in some cases, in the symmetry of the material. These in turn produce significant changes in the electronic band structure. The vibrational modes in the crystal will be affected also [18], but will not be discussed in this thesis.

All configurations of homogeneous strain can be divided into two contributions: the isotropic or hydrostatic component, which gives rise to a volume change without

disturbing the crystal symmetry, and the anisotropic component, which in general reduces the symmetry present in the strain-free lattice. The energy gaps are altered, and in some cases, degeneracies are removed. Effective masses are affected by the variations in energy gaps as well, but these changes are small and we have neglected them. The strain dependence of electronic levels can be characterized by deformation potentials, i.e., the energy shift per unit strain, which are typically from 1 to 10 eV. In strained microstructures, the effects of strain can be used to produce desired effects. This greatly increases the ability to control the electronic and optical properties of such structures.

To fully describe the electronic energy levels of such strained microstructures, it is important to have information about the effects of strain on the properties of the host materials. These include strain-induced changes in the energy gaps and splittings due to the lowering of symmetry.

Below the main results of the strain effects on bulk electronic band structure will be presented.

4.3.2 Strain dependence of energy gaps

Without strain or spin-orbit splitting, the valence-band edge at $\mathbf{k}=0$ in diamond- and zincblende-type materials is a sixfold degenerate multiplet with orbital symmetry $\Gamma_{25'}$ (diamond) or Γ_{15} (zincblende). The spin-orbit interaction lifts this degeneracy into a fourfold degenerate (including spin) $P_{3/2}$ multiplet ($J=3/2$, $M_J=\pm 3/2,\ \pm 1/2$ in spherical notation) and a $P_{1/2}$ multiplet ($J=1/2$, $M_J=\pm 1/2$) as shown in detail in Figure 17. Also given in Figure 17 is the double group notation for the spin-orbit bands as well as the

lowest conduction bands [$\Gamma_{2'}(\Gamma_1)$] in diamond- and zincblende-type semiconductors. Because of the J=3/2 degeneracy, the valence bands have warped energy surfaces [18,19].

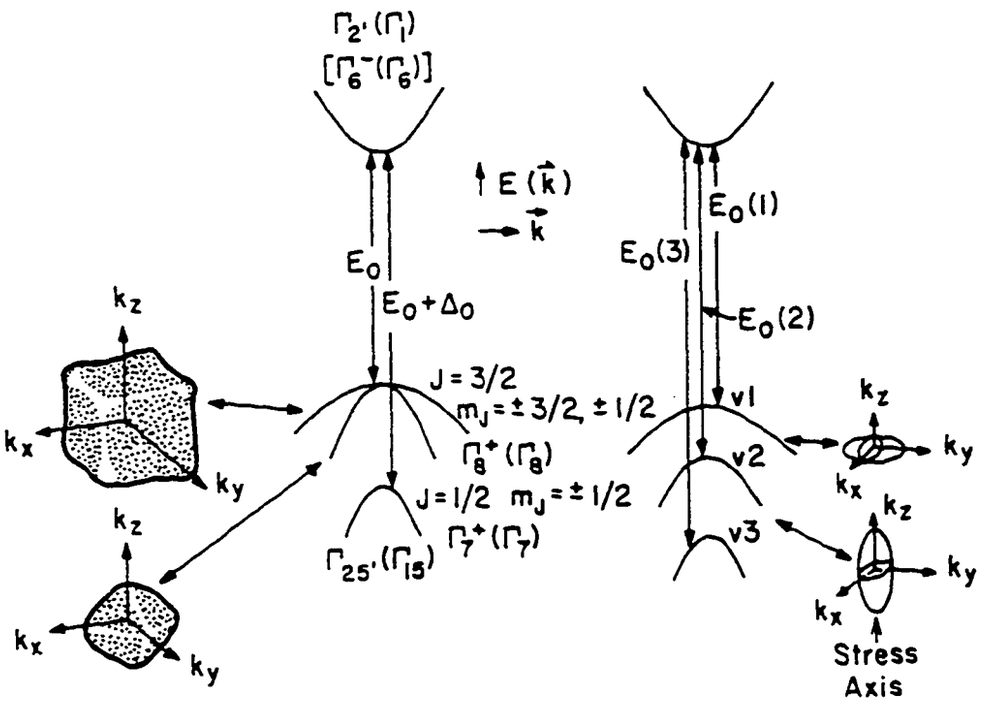

Figure 17. Valence bands and lowest conduction band in diamond- and zincblende-type semiconductors for unstrained (left-hand) and strained (right-hand) crystal.

The fundamental direct gap, i.e., the energy difference between the $\Gamma_6^-(\Gamma_6)$

conduction and $\Gamma_8^-(\Gamma_8)$ valence bands, is denoted as E_0. The spin-orbit splitting is Δ_0, and $E_0+\Delta_0$ is the transition energy between $\Gamma_6^-(\Gamma_6)$ and the spin-orbit split $\Gamma_7^+(\Gamma_7)$ bands.

A strain with a uniaxial component splits the J = 3/2 multiplet into a pair of degenerate Kramers doublets [16-20]. The three valence bands for the case of compressive uniaxial stress along (001) is shown schematically in Figure 17, where the bands are labelled v_1, v_2, and v_3. In addition, the hydrostatic component of the strain will shift the energy gap between valence bands and the lowest lying conduction band. The transition between the conduction band and the v_i valence band is denoted $E_0(i)$, where i=1, 2, 3. The removal of the J=3/2 degeneracy produces energy surfaces that are ellipsoids of revolution around the k_z axis as shown in Figure 17 [19].

It has been shown that strain Hamiltonian $H_\varepsilon^{(v)}$ for a P-like valence-band multiplet can be expressed as [17,18]:

$$H_\varepsilon^{(v)} = H_\varepsilon^{(1,v)} + H_\varepsilon^{(2,v)} \tag{135}$$

where $H_\varepsilon^{(1,v)}$ is the orbital-strain Hamiltonian and $H_\varepsilon^{(2,v)}$ is the strain-dependent spin-orbit Hamiltonian.

The orbital-strain Hamiltonian $H_\varepsilon^{(1,v)}$ of the valence bands can be written as [17,18]:

$$\begin{aligned} H_\varepsilon^{(1,v)} = & -a_1 \mathrm{Tr}(\varepsilon) - 3b[(L_x^2 - \frac{1}{3}L^2)\varepsilon_{xx} + \mathrm{cp}] \\ & -\sqrt{3}\, d[(L_x L_y + L_y L_x)\varepsilon_{xy} + \mathrm{cp}] \end{aligned} \tag{136}$$

where ε_{ij} denotes the components of the strain tensor, $\mathbf{L}$ is the angular momentum operator and cp denotes cyclic permutation with respect to the indices x, y, z. The

quantity a_1 represents the intraband (absolute) shift of the orbital valence bands due to the hydrostatic component of the stress (intraband or absolute hydrostatic deformation potential), while b and d are orbital uniaxial deformation potentials appropriate to strains of tetragonal and rhombohedral symmetries, respectively.

The contribution from strain-dependent spin-orbit Hamiltonian $H_\varepsilon^{(2,v)}$ is very small compared to that of $H_\varepsilon^{(1,v)}$. It will be ignored in the following discussion [18].

At $\mathbf{k}=\mathbf{0}$ the conduction-band minima for the diamond- and zincblende-type solids (except for Si and "zero" bandgap materials such as α-Sn and HgTe) is an antibonding s-state with symmetry $\Gamma_{2'}(\Gamma_1)$. The effects of a strain is to produce a hydrostatic shift given by:

$$H_\varepsilon^{(c)} = a_c \mathrm{Tr}(\varepsilon) \tag{137}$$

where a_c is the intraband (absolute) hydrostatic deformation potential of the $\Gamma_{2'}(\Gamma_1)$ conduction band.

To explore the structure of the conduction and valence bands near $\mathbf{k}=\mathbf{0}$, we shall use the $\mathbf{k}\cdot\mathbf{p}$ perturbation approach where the Hamiltonian is given by [21]:

$$H_k = H_0 + \left[\frac{\hbar^2 k^2}{2m_0}\right] + \left[\frac{\hbar}{m_0}\right]\mathbf{k}\cdot\mathbf{p} \tag{138}$$

where H_0 is given in Eq.(127), and $\mathbf{p}$ is the momentum operator. Therefore, the total Hamiltonian including the spin-orbit interaction H_{so} can be written as:

$$H = H_k + H_{so} + H_\varepsilon^{(c)} + H_\varepsilon^{(1,v)} \tag{139}$$

We choose the set of wave functions that make H_{so} diagonal. These are functions

that have the same transformation properties as the eigenfunctions of the total angular momentum operator **J** (=**L**+**S**), i.e., $|J, M_J\rangle$. For the s-like $\Gamma_{2'}$ (Γ_1) conduction band these wave functions are [21]:

$$|1/2,1/2\rangle_c = |S\uparrow\rangle \tag{140}$$

$$|1/2,-1/2\rangle_c = |S\downarrow\rangle \tag{141}$$

while for the P-like Γ_8^+ (Γ_8), Γ_7^+ (Γ_7) valence bands, they can be written as:

$$|3/2,3/2\rangle = (1/\sqrt{2})(X+iY)\uparrow \tag{142}$$

$$|3/2,1/2\rangle = (1/\sqrt{6})(X+iY)\downarrow -(\sqrt{2/3})Z\uparrow \tag{143}$$

$$|3/2,-1/2\rangle = -(1/\sqrt{6})(X-iY)\uparrow -(\sqrt{2/3})Z\downarrow \tag{144}$$

$$|3/2,-3/2\rangle = -(1/\sqrt{2})(X-iY)\downarrow \tag{145}$$

$$|1/2,1/2\rangle = (1/\sqrt{3})(X+iY)\downarrow +(1/\sqrt{3})Z\uparrow \tag{146}$$

$$|1/2,-1/2\rangle = (1/\sqrt{3})(X-iY)\uparrow -(1/\sqrt{3})Z\downarrow \tag{147}$$

Using these basis wave functions, the 8×8 matrix of the Hamiltonian Eq.(139) can be written down explicitly [18]. By solving the eigenvalue problem of this Hamiltonian matrix, the strain-dependent dispersion relation of the band structure near **k**=**0** and the corresponding eigenfunctions can be found.

For (001) built-in biaxial strain of magnitude ε, which is the case of strained-layer microstructures involved in this thesis, the 8×8 strain Hamiltonian becomes two

decoupled identical 4×4 matrices [17,18]:

$$
\begin{array}{c}
\quad |S\uparrow> \quad |3/2,3/2> \quad |3/2,1/2> \quad |1/2,1/2> \\
[H_\epsilon]= \begin{bmatrix}
E_0+\delta E_H^c & 0 & 0 & 0 \\
0 & -\delta E_H^v-\delta E_s & 0 & 0 \\
0 & 0 & -\delta E_H^v+\delta E_s & \sqrt{2}\,\delta E_s \\
0 & 0 & \sqrt{2}\,\delta E_s & -\Delta_0-\delta E_H^v
\end{bmatrix}
\end{array}
\tag{148}
$$

where δE_H^c, δE_H^v, δE_S are defined as:

$$
\begin{aligned}
\delta E_H^c &= a_c(2-\lambda)\varepsilon \\
\delta E_H^v &= a_l(2-\lambda)\varepsilon \\
\delta E_s &= b(1+\lambda)\varepsilon
\end{aligned}
\tag{149}
$$

with

$$
\lambda = 2C_{12}/C_{11} \tag{150}
$$

where C_{12} and C_{11} are the elastic stiffness constants. These constants and the interband hydrostatic pressure deformation potential a $(=a_l+a_c)$ of E_0 and the shear deformation potentials can be found in the literature [18,22]. The strain-dependent transition energies between the conduction band the valence bands can be written as [18]:

$$E_0(2) = E_0 + \delta E_H + \delta E_s \tag{151}$$

$$E_0(1) = E_0 + \delta E_H + \frac{\Delta_0 - \delta E_s}{2} - \frac{1}{2}\sqrt{\Delta_0^2 + 2\Delta_0 \delta E_s + 9(\delta E_s)^2} \tag{152}$$

$$E_0(3) = E_0 + \delta E_H + \frac{\Delta_0 - \delta E_s}{2} + \frac{1}{2}\sqrt{\Delta_0^2 + 2\Delta_0 \delta E_s + 9(\delta E_s)^2} \tag{153}$$

where

$$\delta E_H = (a_1 + a_c)(2 - \lambda)\varepsilon = a(2 - \lambda)\varepsilon \tag{154}$$

$$\delta E_s = \varepsilon = -b(1 + \lambda)\varepsilon \tag{155}$$

where a is the interband hydrostatic pressure deformation potential of E_0 and b is the shear deformation potential. The strain-dependent wave functions for the three valence bands are given by [23]:

$$|v_2\rangle = |3/2, \pm 3/2\rangle \tag{156}$$

$$|v_1\rangle = \alpha\,|3/2, \pm 1/2\rangle + \beta\,|\pm 1/2\rangle \tag{157}$$

$$|v_3\rangle = -\beta\,|3/2, \pm 1/2\rangle + \alpha\,|1/2, \pm 1/2\rangle \tag{158}$$

where

$$\alpha = 2\sqrt{2}\,|\delta E_s|/q \tag{159}$$

$$\alpha = \frac{(n-p)\delta E_s}{q\,|\delta E_s|} \tag{160}$$

with

$$p = \Delta_0 + \delta E_s$$
$$n = \sqrt{p^2 + 8(\delta E_s)^2} \qquad (161)$$
$$q = \sqrt{2n(n-p)}$$

4.3.3 Effects of Built-in Strain on Semiconductor Microstructures

The most important effect of built-in strain in the strained layer microstructures is to change the 1D SL potential profiles. The built-in biaxial strain will shift and split the energy bands [18]. Depending on magnitude and sign of the strain the ordering of HH and LH levels can be switched. One can even have a type I potential profile for the HH band and a type II potential profile for the LH band, or vice versa. Therefore, depending on the strain in each material and on the band discontinuity, a large number of band alignment configurations may be obtained [24,25].

Pseudomorphic microstructures are coherently grown such that the in-plane lattice constants of the thin layers composing the system are forced to match that of the substrate (or buffer) lattice constant. Usually only one type of the host materials is strained. For example, in the pseudomorphic InGaAs/GaAs QW structures grown on GaAs substrate, only the InGaAs layer is under a biaxial strain. Assume a_S to be the bulk lattice constant of the substrate (or buffer) and a_T to be the bulk lattice constant of strained thin layer material, the biaxial strain ε present in the thin layer is given by:

$$\varepsilon = \frac{a_S - a_T}{a_T} \tag{162}$$

Since the stain effects are easily comparable with the level spacing due to size quantization, it is clear that they should be taken into account for quantitative interpretations of the electronic properties of strained layer heterostructures. For microstructures with built-in [001] biaxial strain, which is the case in this thesis, the approach is quite straight forward. It is accomplished by using the envelope function approach, with the strain-effects incorporated by using the input material parameters modified by the built-in strain [24,26-29].

4.4 Quantum Confined Stark Effect

Effect of electric field on QW structures was described, among others, by J. Singh [30], C. Weisbuch and B. Vinter [31]. There are generally two possible cases: the electric field can be applied in the growth direction of quantum structure or in the plane of the well. The latter case is similar to the 3D case and excitons dissociate at quite small fields (below 10 kV/cm). The former is more interesting since the exciton can exist up to fields of 100 kV/cm and above. This is due to electron and hole wave function confinement in the potential well.

The dominant effect under influence of electric field in QWs is intersubband separation change. The field pushes the electron and the hole wavefunctions to opposite sides decreasing the ground state intersubband separation. The second smaller effect due to separation of the electron and hole wavefunction is the decrease of the exciton binding

energy.

The exact solutions for the wavefunction inside the well in the presence of an electric field can be expressed in terms of Airy functions. The equations obtained from the matching of the continuity conditions at the edges of the well are transcendental but can be solved numerically.

For the quantum well of height V_w and width L_w the potential varies as:

$$\begin{aligned} U(z) &= e|\mathbf{F}_w|z \qquad && \text{for} |z| < \frac{L_w}{2} \\ U(z) &= V_w + e|\mathbf{F}_0|z \qquad && \text{for} |z| > \frac{L_w}{2} \end{aligned} \tag{163}$$

where F_w (F_o) is field inside (outside) of the well

and the Schrödinger equation must be solved in three separate regions:

$$-\frac{\hbar^2}{2m^*}\frac{d^2\psi_1(z)}{dz^2} = \{E-[e|\mathbf{F}_0|z+V_w+e(|\mathbf{F}_0-\mathbf{F}_w|)\frac{L_w}{2}]\}\psi_1(z) \quad z \le -\frac{L_w}{2} \tag{164}$$

$$-\frac{\hbar^2}{2m^*}\frac{d^2\psi_2(z)}{dz^2} = \{E-[e|\mathbf{F}_w|z]\}\psi_2(z) \qquad |z| \le -\frac{L_w}{2} \tag{165}$$

$$-\frac{\hbar^2}{2m^*}\frac{d^2\psi_3(z)}{dz^2} = \{E-[e|\mathbf{F}_0|z+V_w-e(|\mathbf{F}_0-\mathbf{F}_w|)\frac{L_w}{2}]\}\psi_3(z) \quad z \ge -\frac{L_w}{2} \tag{166}$$

Wavefunctions $\psi(z)$ and of $1/m^*(z)d\psi/dz$ must be continuous at the interfaces. To comply with these requirements, linear combinations of Airy functions (Ai and Bi) have to be used.

4.5 GRINSCH Lasers

4.5.1 Experimental Details

The sample used in this study was grown by MBE on a GaAs (001) substrate. The basic unit of the structure consisted of (1) a pseudomorphic InGaAs SQW surrounded on each side by (2) 100Å of GaAs sandwiched between (3) linearly graded $Ga_{1-y}Al_yAs$ GRINSCH regions ($0.1<y<0.4$) and (4) heavily-doped $Ga_{0.6}Al_{0.4}As$ *n*-and *p*-type confining layers. From the growth conditions the intended value of the In composition was 15% and well width (L_W) was 80Å. The CER apparatus was similar to one already described [32]. The ac modulating voltage of 1 kV peak-to-peak was applied in a capacitor-like arrangement at a frequency of 200 Hz. The intensity of the probe beam was 50 $\mu W/cm^2$.

4.5.2 Experimental Results

Displayed by the solid line in Figure 18 is experimental room temperature CER spectrum of the 0.98 μm InGaAs/GaAs/GaAlAs GRINSCH laser structure. We have obtained signals from all three relevant sections of the sample, i.e., InGaAs SQW, GaAs and GaAlAs regions. The signals below the GaAs band (1.422 eV) originate in the InGaAs SQW while in the region from 1.568 eV ($y = 0.1$) to 2.004 eV ($y = 0.4$) the spectrum is from the graded $Ga_{1-y}Al_yAs$ portion of the laser structure [33]. The signals between 1.422 eV and 1.568 eV originate in the GaAs region. These regions are indicated in the figure.

Shown by the dotted line in Figure 19 is the experimental CER data in the

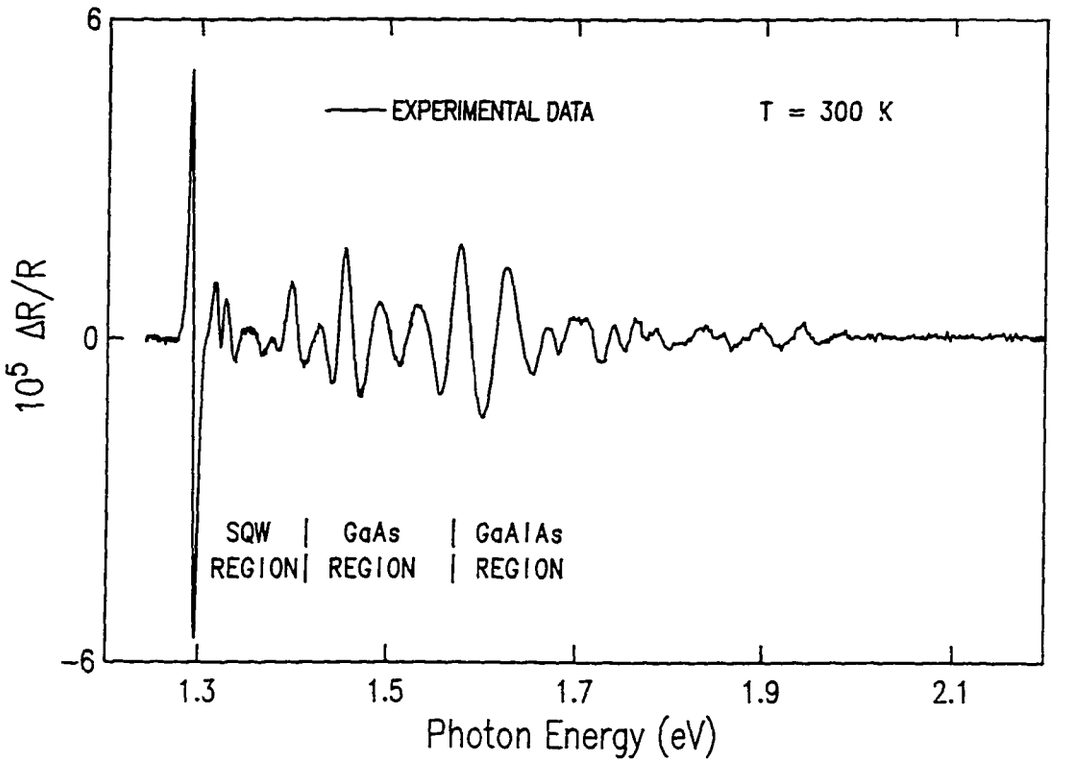

Figure 18 The solid line is the experimental room temperature CER spectrum of InGaAs/GaAs/GaAlAs GRINSCH laser structure.

spectral region of the InGaAs SQW. The strong, lowest lying feature is *11H*. Above about 1.42 eV the signal is from the GaAs. The solid line is a least-squares fit to the FDLP, which is appropriate for excitonic transitions [32,34-35]. The obtained values of the various intersubband energies are shown at the bottom of the figure by arrows, denoted *A-F*, and also are listed in Table IV.

The figure also shows that the position of *11H* can easily be determined to ± 1 meV. This is because (a) *11H* is sharp with a linewidth of 4.5 meV (half-width at half maximum) and (b) the derivative-like nature of CER with ability to fit the lineshape.

In order to evaluate L_W and the In composition of the SQW we have compared the

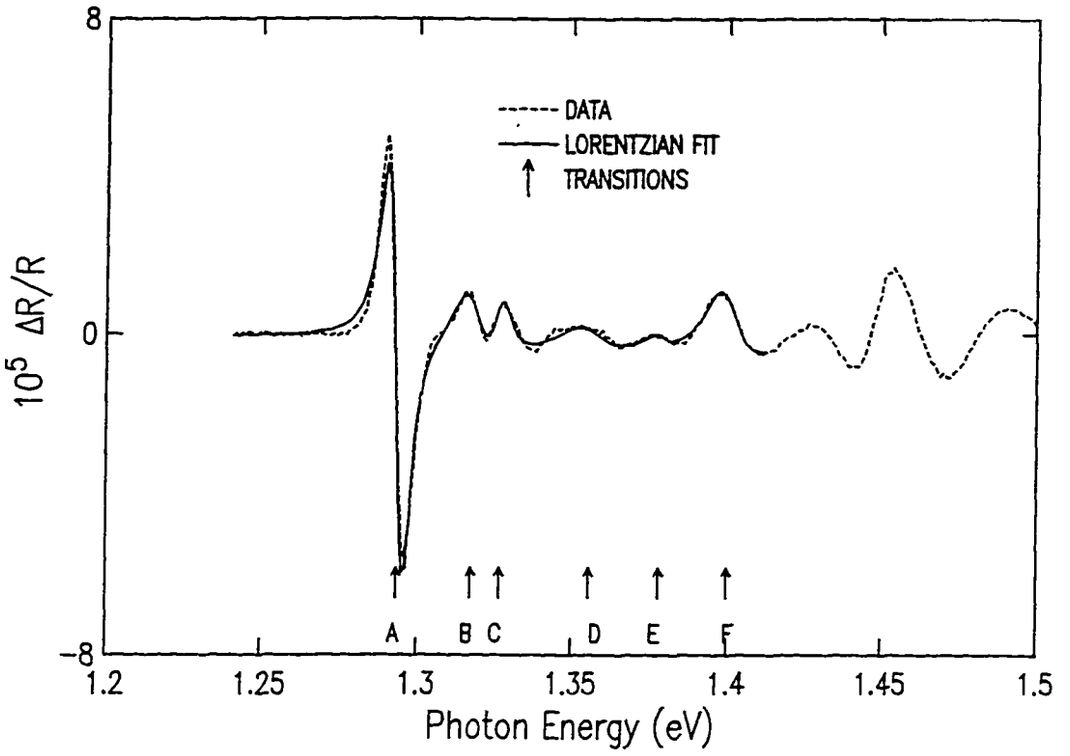

Figure 19. Experimental CER spectrum (dashed line) from the InGaAs SQW at 300K. The solid line is a fit to a FDLP, yielding values of the energies designated by arrows.

experimentally observed energies of the features *A-F* with a theoretical model [9]. We have calculated the energy eigenvalues by solving Schrödinger equation in an envelope function calculation [36], including the effects of strain and electric field, to determine the band-to-band energies of the various transitions. The electron and hole masses, band offset (before strain) and deformation potentials listed in Ref. [37] were employed. Exciton binding energies of 8 meV were used for the transitions [36].

The theoretical calculation of the potential [9], displayed on Figure 20, Figure 21, and Figure 22 , including strain effect due to a lattice mismatch between $In_xGa_{1-x}As$ and GaAs and electric field effects, shows that HHs are confined in the $In_xGa_{1-x}As$ layer (type

I heterostructure) while the LHs are confined in the GaAs region (type II heterostructure). This is a direct result of the presence of a GaAs well.

TABLE IV. Comparison of experiment and calculation for the energy levels of the InGaAs SQW of a laser structure based on an In composition of 15.5% and a well width of 80Å

Spectral Feature	Experiment (eV)	Calculation [a] (eV)	Transition
A	1.293	1.293	*11H*
B	1.317	1.321	*13H*
C	1.327	1.329	*12L*
D	1.356	1.349 / 1.354	*21L / 13L*
E	1.378	1.377	*23H*
F	1.400	1.391	*31H*

(a) Taking into account 8 meV exciton binding energy

Listed in Table IV are the calculated values of a number of $\tilde{m}\tilde{n}H(L)$ transitions using an In composition of 15.5% and L_W = 80Å, including exciton binding energy effects. There is good overall agreement with the feature *A* being identified with *11H*,

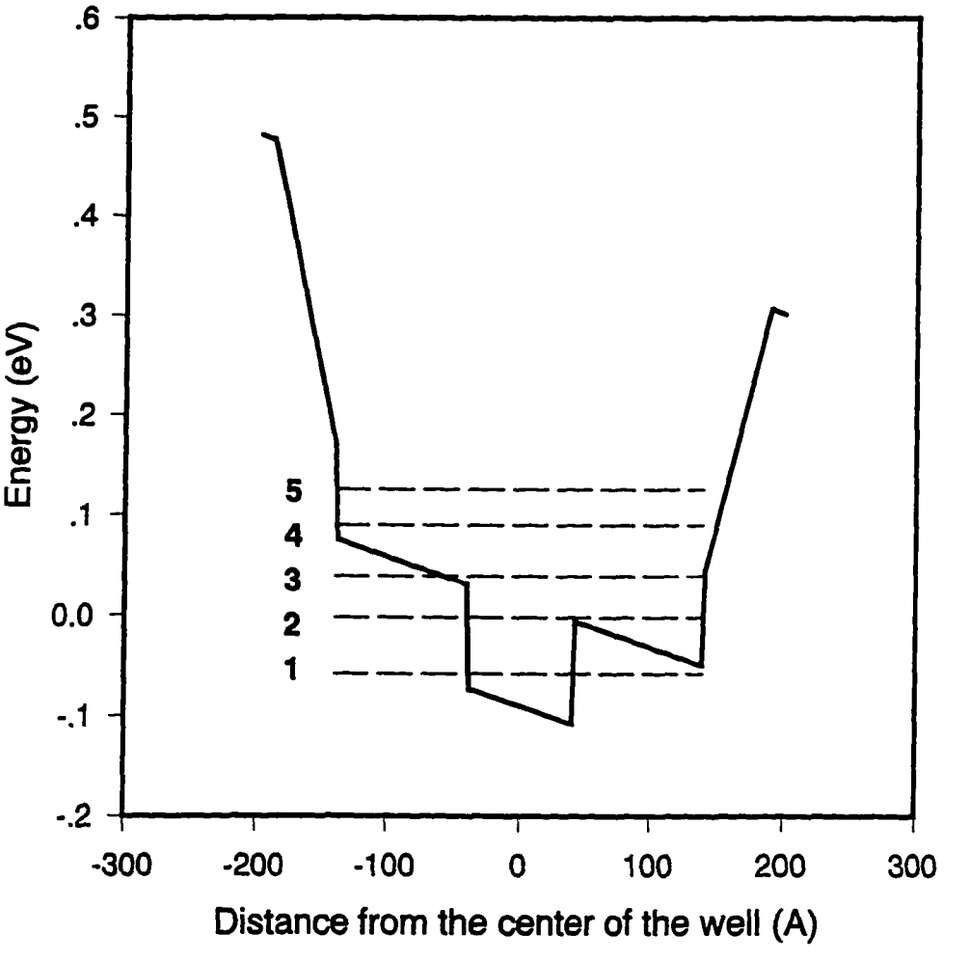

Figure 20. Electron potential profile with built-in field F = 45 kV/cm, In=15.5%, L_w = 80Å, dotted lines show the first few energy levels.

B with *13H*, *C* with *12L*, *D* with *13L/21H*, etc. The *D* peak also was identified as a LH transition by a comparison of PzR and CER spectra. The former showed an enhancement of the ratio of the amplitudes of *D/A* in relation to the later [32]. The similar enhancement of the ratio of the amplitudes of *C/A* was not observed and this fact is under

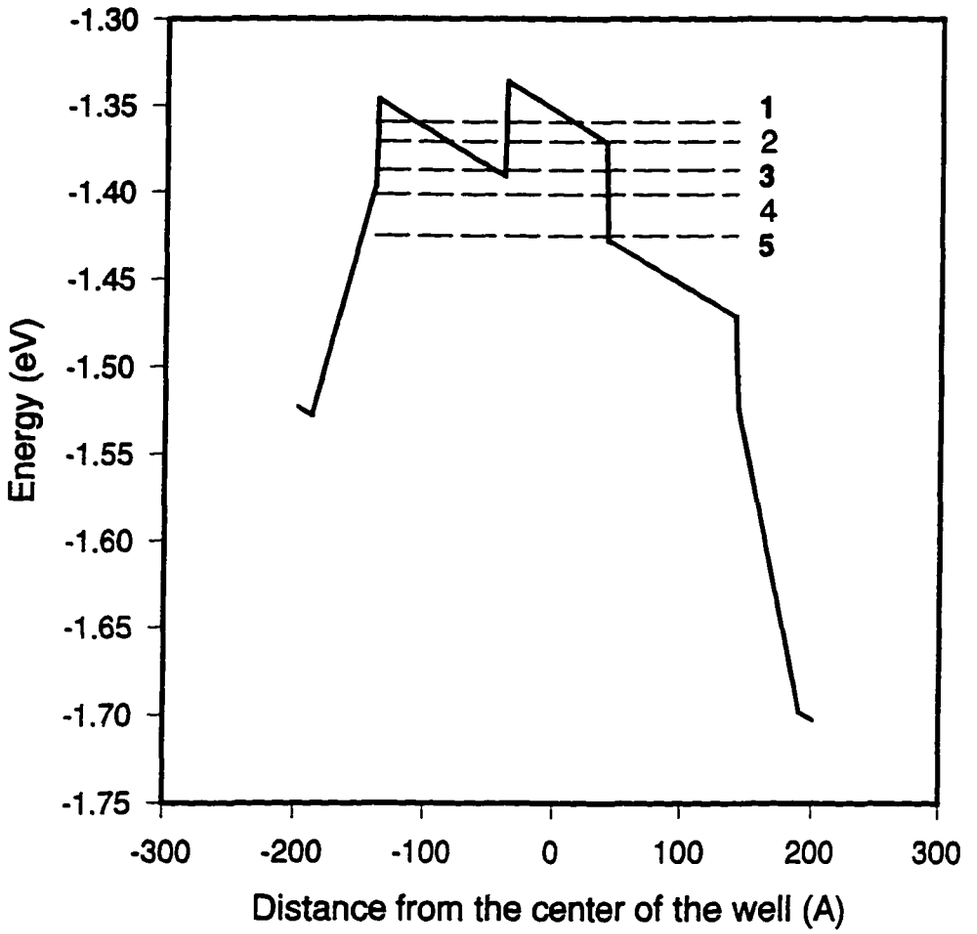

Figure 21. Heavy hole potential profile with built-in field F = 45 kV/cm, In=15.5%, L_w = 80Å, dotted lines show the first few energy levels.

further investigation. The presence of the symmetry-forbidden transitions *21H* and *23H* is due to the built-in electric field. The *11L*, *12H* and some other transitions are very weak due to very small overlap of electron and hole wavefunction and are not visible in our experiment. This phenomena becomes evident when behavior of electrons, HHs and

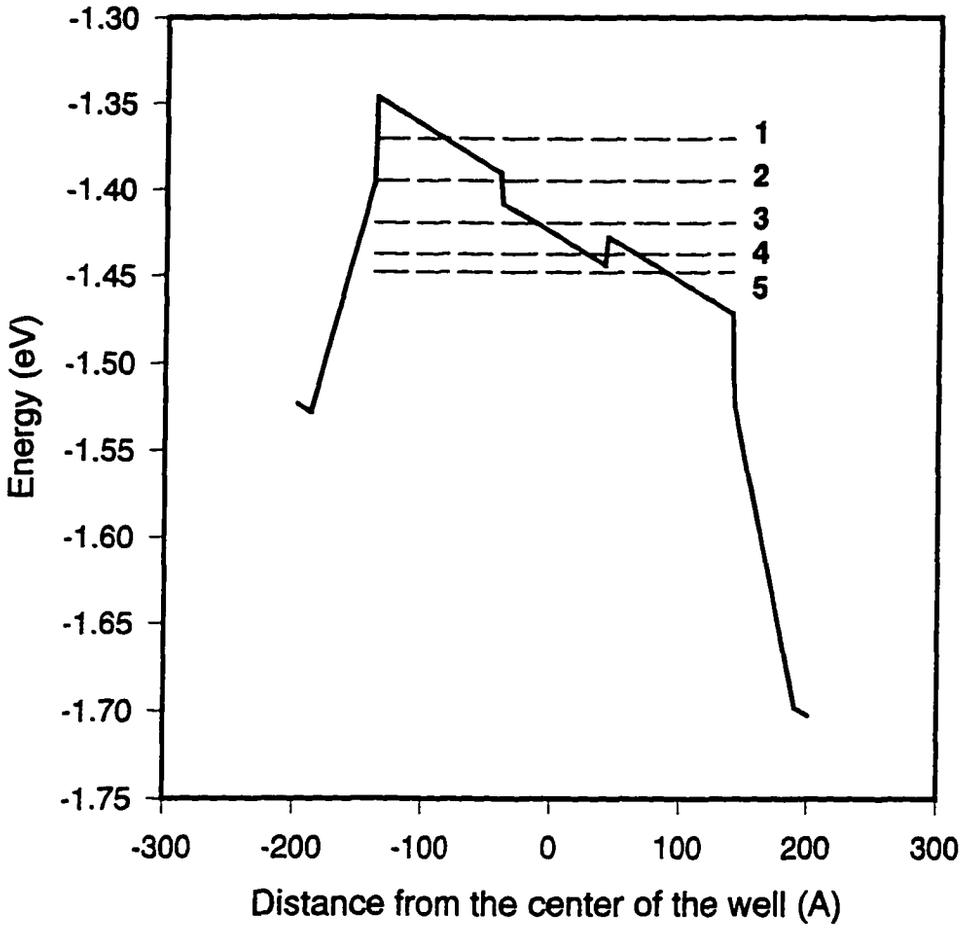

Figure 22. Light hole potential profile with built-in field F = 45 kV/cm, In=15.5%, L_w = 80Å, dotted lines show the first few energy levels.

LHs under influence of the electric field is examined closer. Square of electron, HH and LH wavefunctions is shown in Figure 23. As can be seen the field pushes the electron and hole wavefunctions to opposite sides, significantly decreasing the overlap for some transitions.

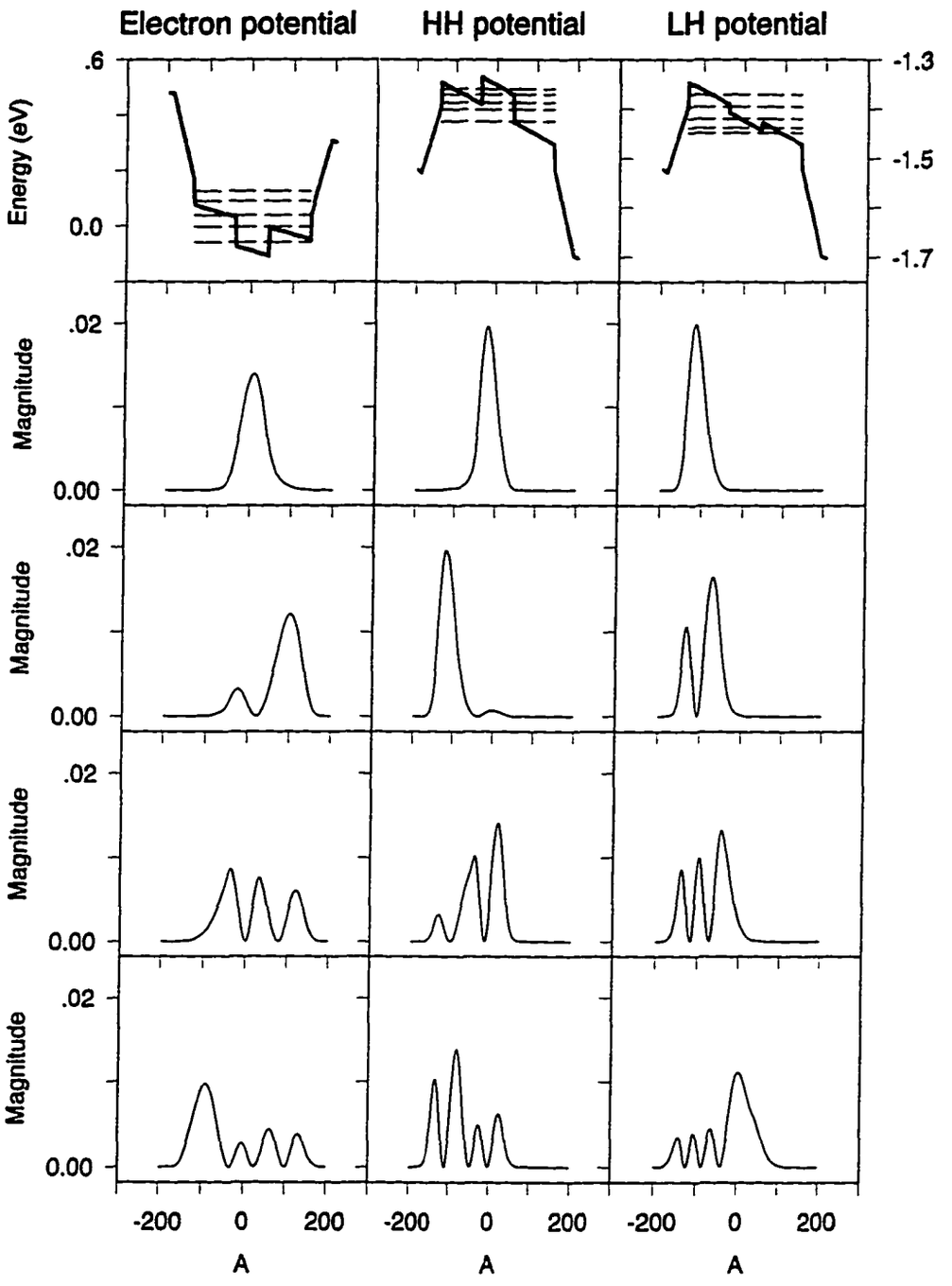

Figure 23. Potential profiles and square of first few wavefunctions for electrons, heavy and light holes.

4.5.3 Electric Field Effect - Franz-Keldysh Oscillations in GRINSCH

The oscillatory features in the GaAlAs graded region in Figure 18 are the FKOs. From the period of these FKOs it is possible to directly evaluate built-in field by this nondestructive optical approach. The positions of the N^{th} extrema in the FKOs are given by Eq.(56) [32,34-35].

Plotted in Figure 24 by open squares is $4/3\pi(E_N-E_g)^{3/2}$ as a function of FKOs index N for graded GaAlAs region. The solid line is a least-squares fit to a linear function which makes it possible to evaluate F = 47 kV/cm. The electron and HH masses for an Al composition of 10% listed in Ref. [38] were employed. Small variations of masses, due to the grading, produced a change in the field value by only a few percent and hence were neglected.

The deduced value F is in a good agreement with the value obtained from a computer simulation of the field profile which we have performed using a comprehensive, self-consistent model with the structure parameters listed above [39].

Even in the absence of the field from the *p*-and *n*-doped confining layers (F_{pin}) one might expect to see FKOs-like features from the insulating (*i*) GaAlAs region because of the potential profile produced by the grading. The period of these oscillations would be given by Eq.(56) with an electro-optic energy expressed as:

$$(\hbar\theta)^3 = q^2\hbar^2\left(\frac{F_{e,grad}^2}{2m_{e,\parallel}^*} + \frac{F_{h,grad}^2}{2m_{h,\parallel}^*}\right) = \frac{q^2\hbar^2F_{grad}^2}{2\mu_\parallel} \qquad (167)$$

where $m_{e,\parallel}^*$ and $m_{h,\parallel}^*$ are the electron and hole effective masses in the direction of the grading, respectively, and

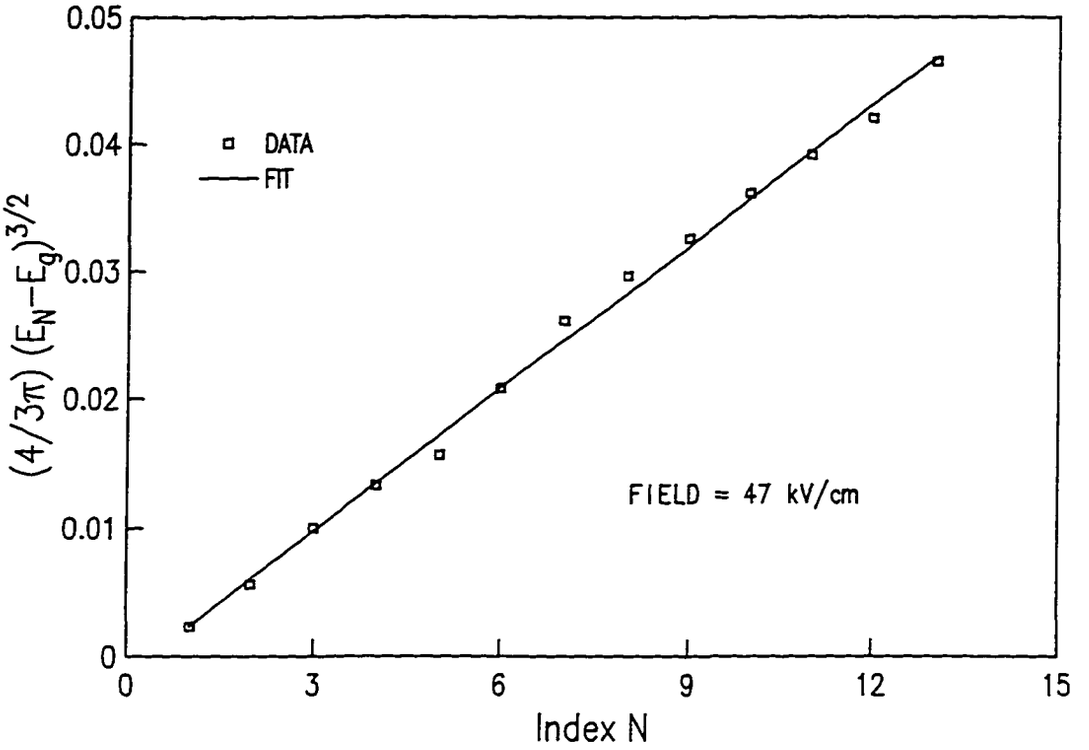

Figure 24. The plot of $(4/3\pi)(E_N-E_g)^{3/2}$ as a function of FKOs index N for the graded GaAlAs region.

$$F_{e,grad} = \frac{qQ_c\Delta E}{L_{grad}}, \quad F_{h,grad} = \frac{q(1-Q_c)\Delta E}{L_{grad}}. \tag{168}$$

In Eq.(168) Q_c is the conduction band offset parameter (0.65), $\Delta E = (E_g^{Ga_{0.6}Al_{0.4}As} - E_g^{Ga_{0.9}Al_{0.1}As})$ and L_{grad} is the width of the graded region (1800Å). Therefore, the total field deduced from the observed FKOs should be a combination of F_{pin} and F_{grad} (= 18 kV/cm). The fact that the experimental FKOs yield a field equal to F_{pin} is probably due to the fact that (a) $F_{grad} << F_{pin}$ and (b) the photovoltaic effect which serves to drive the system towards flat band, i.e., reduce the built-in field.

Chapter 5. GaAs/GaAlAs HETEROJUNCTION BIPOLAR TRANSISTOR

5.1 Introduction

GaAs/GaAlAs HBTs consist of a thin region of p-type material constructed between two n-type regions. The electric potential on the base (p-doped GaAs) controls the number of charges which pass through from the more highly doped emitter (n-doped GaAlAs) to the less highly doped collector (n-doped GaAs). The emitter-base interface forms a doped GaAlAs/GaAs HJ while the collector-base GaAs/GaAs interface is a homojunction. PR and CER signals from the collector and emitter regions are spectrally isolated and can provide many important information.

Measurements of the in-phase and quadrature signals from the collector and emitter regions, as a function of a modulation frequency, made it possible to determine the RC time constants, τ_1 and τ_2, of the equivalent circuits of these regions. From analysis of FKOs in the room temperature spectra it is possible to evaluate the dc electric fields in the GaAlAs emitter (F^{emit}) as well as in the GaAs collector (F^{coll}) region. It has been found earlier that dc electric fields in the GaAlAs emitter have direct relation to actual device performance. However, the field deduced from the FKOs may not necessarily represent the actual field in the emitter/base or collector/base regions of the structure. The built-in electric fields can be reduced by the illumination (pump and/or probe beams) due to the photovoltaic effect. To explore further the influence of the photovoltaic effect we have evaluated the illumination dependence of the fields deduced

from the FKOs.

5.2 Equivalent Circuit Analysis

The contactless EM method of PR has proven to be a valuable experimental method to investigate the properties of semiconductors (bulk/thin film) [1,2], semiconductor microstructures [1,2] (QWs, quantum dots [3], HJs), surfaces/interfaces [1,2] and actual device configurations (HBTs, pseudomorphic high electron mobility transistors, vertical cavity surface emitting lasers, etc.) [2,4]. Not only is PR contactless but it also requires no special mounting of the sample and hence can be performed nondestructively on wafer sized samples. Most of these investigations have used the sharp, derivative-like optical structures produced by this technique, including (FKOs) [1,2]. However, since PR is an ac technique there is also important information in other modulation variables such as phase, modulation frequency (Ω_m), amplitude, etc. [2] in addition to the sharp, derivative-like spectral features. PR is the optical response of the material to the modulating ac electric field and hence can be considered as a contactless optical impedance spectroscopy. However, very little work has been done in this area of modulation spectroscopy. The first report of EM as an optical impedance spectroscopy was by Silberstein et. al. [5], who demonstrated that electrolyte electroreflectance (EER) could be used to obtain the electrical impedance of a semiconductor-electrolyte interface. These authors measured the in-phase and quadrature EER signals as a function of Ω_m in the range 10 Hz $< \Omega_m <$ 10 kHz. Subsequently a number of articles reported the evaluation of trap times by measuring the frequency response of PR signals from various

semiconductors including temperature dependent measurements [2]. Also several investigators have made use of the phase of PR [2,6,7], including a recent study on interference effects from epitaxial layers [6]. Shen et. al. studied the time constants involved in PR from several surface/undoped/n^+-GaAs (001) structures by measuring the rise and fall times of the signals using a digital oscilloscope [8].

In this section we report a room temperature PR study of the signals from the collector and emitter regions of a GaAs/GaAlAs HBT structure. The in-phase and quadrature signals from these spectrally isolated portions of the sample were evaluated in the frequency range 2 Hz $< \Omega_m <$ 100 kHz. These measurements made it possible to determine the RC time constants, τ_1 and τ_2, of the equivalent circuits of the collector and emitter regions, respectively. An analysis of the former reveals that the recombination mechanism in the collector-base region is due to midgap trap states and is dominated by the hole current. This experiment demonstrates a new area of application for this method for the characterization of these devices.

5.2.1 Experimental Details

The GaAs/GaAlAs HBT sample used in this study was fabricated by MBE and had the following characteristics. The collector contact layer, 6000Å of n^+-GaAs ($\approx 5 \times 10^{18}$ cm^{-3}), was grown on an undoped liquid encapsulated Czochralski <001> semi-insulating substrate. This was followed by the collector layer of 7000Å of n^--GaAs ($\approx 7.5 \times 10^{15}$ cm^{-3}) and the 1400Å p^+-GaAs base ($\approx 1 \times 10^{19}$ cm^{-3}). The 1800Å n-GaAlAs ($\approx 5 \times 10^{17}$ cm^{-3}) emitter was graded in Al composition at the top and bottom over 300Å.

The n^+-GaAs ($\approx 7 \times 10^{18}$ cm^{-3}) emitter contact layer was about 750Å thick. The dopants were Si and Be for the *n*- and *p*-type regions, respectively. The PR apparatus has been described in Chapter 2 [1,2]. The pump beam was the 670 nm line of a laser diode modulated by an acousto-optic modulator [9]. The intensities of the pump and probe beams were 600 μW/cm^2 and 100 μW/cm^2, respectively. The phase reference was determined by using the pump beam scattered from the sample with the probe beam blocked.

5.2.2 Experimental Results

Plotted in Figure 25 is the PR spectrum at 300K from the collector and emitter regions of the sample at Ω_m = 500 Hz. The signals occur in the region of the direct band gaps of GaAs [E_0(GaAs)] and GaAlAs [E_0(GaAlAs)], respectively. From the position of the latter we can deduce an Al composition of 28%. Both spectra exhibit pronounced FKOs.

Displayed in Figure 26 and Figure 27 are the normalized in-phase (open circles) and quadrature (closed circles) amplitudes of the collector and emitter PR signals, respectively, as a function of modulating frequency in the range 2 Hz $< \Omega_m <$ 100 kHz.

5.2.3 Analysis

We have analyzed the frequency dependent data of Figure 26 and Figure 27 on the following basis. The photovoltage, $V_p(t)$, induced by the pump beam can be expressed as:

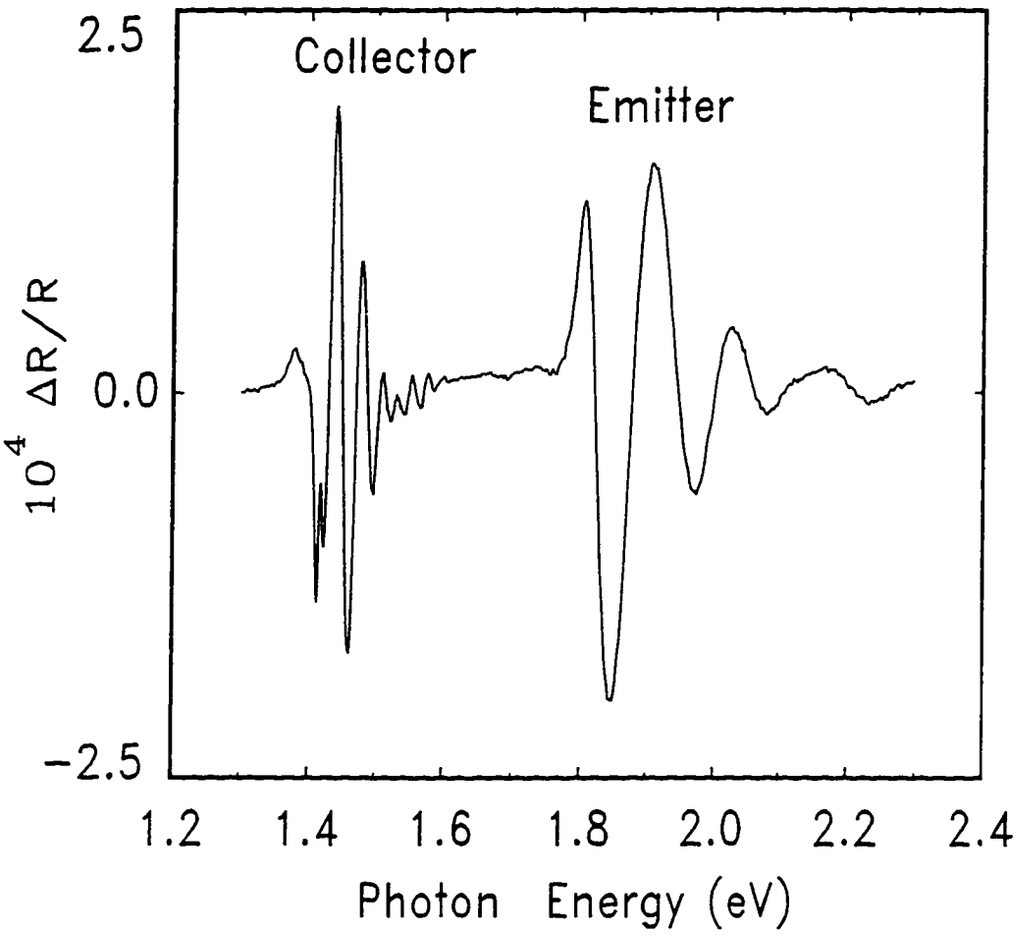

Figure 25. PR spectrum (in-phase component) in the region of E_0 of GaAs (collector) and GaAlAs (emitter) of a GaAs/GaAlAs HBT at 300K.

$$V_p(t) \propto \begin{cases} \dfrac{(e^x-1)}{2\sinh x} e^{-t/\tau} & -1/2f_m < t < 0 \\ 1 - \dfrac{(e^x-1)}{2\sinh x} e^{-t/\tau} & 0 < t < 1/2f_m \end{cases} \tag{169}$$

where $x = 1/2\Omega_m\tau$ and τ is the characteristic time constant of the circuit. In Eq.(169) we have assumed equal rise and fall times for the circuit. By taking the Fourier transform of Eq.(169) it can be shown that the frequency dependence of the first harmonic in-phase and quadrature components of the signal are given by:

$$\text{in-phase} = \frac{1}{[1+(2\pi f_m\tau)^2]}, \qquad \text{quadrature} = \frac{2\pi f_m\tau}{[1+(2\pi f_m\tau)^2]}. \tag{170}$$

Shown by the solid and dashed lines in Figure 26 (GaAs collector) and Figure 27 (GaAlAs emitter) are least-square fits of Eq.(170) to the frequency dependence of the in-phase and quadrature components of the PR signal, respectively. The obtained time constants are $\tau_1 = 1.8 \times 10^{-4}$ sec and $\tau_2 = 3.6 \times 10^{-3}$ sec, respectively. Note that the time constant of the emitter region is more than an order of magnitude greater than that of the collector portion.

In the collector-base *p-n* junction, assuming the saturation current is due to thermionic emission, the resistance times area (RA) can be written as [10]:

$$RA = (kT/q)(1/A^*T^2)\exp(E_b/kT), \tag{171}$$

where A^* is the Richardson constant and E_b is an effective barrier height for the saturation current. The capacitance per unit area (C/A) for an abrupt one-sided *p-n* junction is [10]:

$$C/A = (qn_c\kappa\epsilon_0/2V_{bi})^{1/2}, \tag{172}$$

with n_c being the *n*-type collector carrier concentration (7.5×10^{15} cm^{-3}), κ is the static dielectric constant (= 13 for GaAs), ϵ_0 is the permittivity of free space and V_{bi} is the

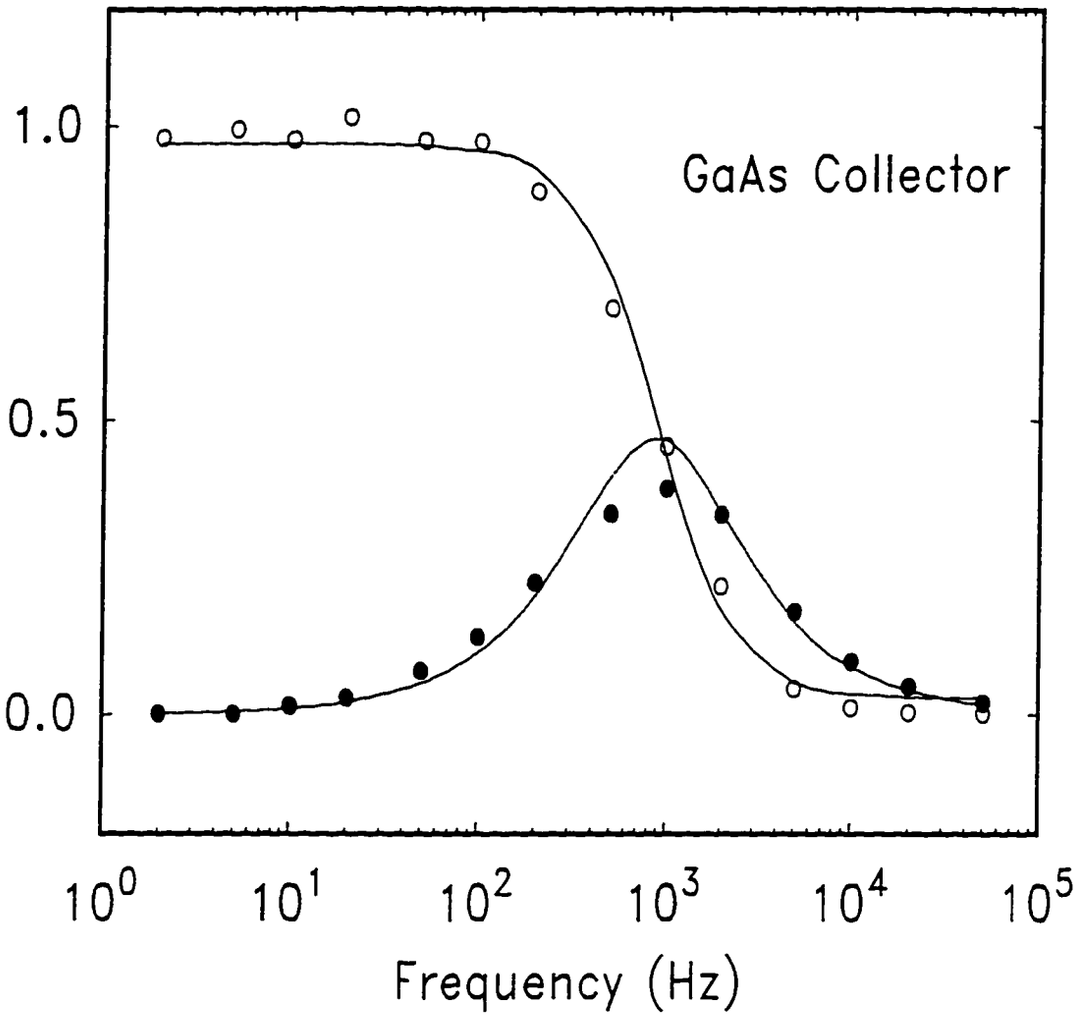

Figure 26. In-phase (open circles)/quadrature (closed circles) signals vs Ω_m for the GaAs collector. The solid/dashed lines are fits to Eq.(170).

built-in potential. For an ideal *p-n* junction V_{bi} can be expressed as [10]:

$$qV_{bi} = E_0 + kT\ln(n_c p_b / N_c P_v), \tag{173}$$

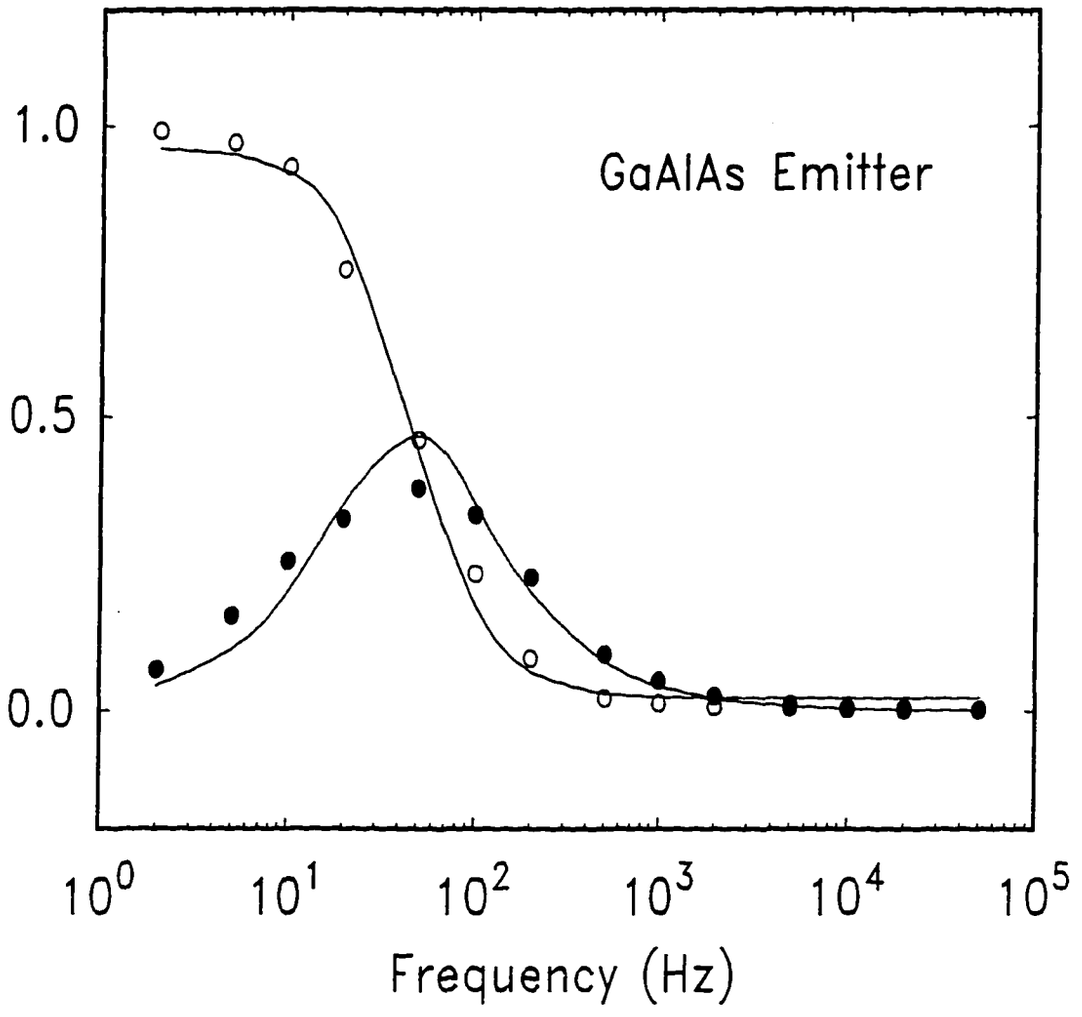

Figure 27. In-phase (open circles)/quadrature (closed circles) PR signals vs Ω_m for the GaAlAs emitter. The solid/dashed lines are fits to Eq.(170).

where p_b is the p-type carrier concentration in the base ($\approx 1 \times 10^{19}$ cm^{-3}) and N_c (4.7×10^{17} cm^{-3}) and P_v (7.0×10^{18} cm^{-3}) are the density-of-states of the conduction and valence bands, respectively. With $E_0 = 1.42$ eV we find $V_{bi} = 1.32$ V for the ideal case.

From Eqs.(171) and (172) the time constant, τ_1, is given by:

$$\tau_1 = RC = (kT/q)(1/A^* T^2)(q n_c \kappa \epsilon_0 / 2V_{bi})^{1/2} \exp(E_b/kT), \qquad (174)$$

so that:

$$E_b = kT \ln[\tau_1 A^* T^2/(kT/q)(q n_c \kappa \epsilon_0/2)^{1/2}] + (kT/2) \ln V_{bi}. \quad (175)$$

The second term in Eq.(175) is small compared to the first term.

With τ_1 = 1.8 x 10^{-4} sec, n_c = 7.5 x 10^{15} cm^{-3} and assuming that the saturation current is due to the holes (A^* = 74 A/cm^2K^2 [10]) we find that E_{bh} = 0.73 eV for hole barrier height in the collector-base region.

Both the collector and emitter signals exhibit pronounced FKOs (see Figure 25). The positions of the N^{th} extrema in the FKOs are given by Eq.(56) [1,2]. With μ_l (in units of the free electron mass) = 0.055 (GaAs) and 0.073 (GaAlAs) we find F = 3.0 x 10^4 V/cm and 1.9 x 10^5 V/cm for the collector and emitter regions, respectively. This issue will be discussed in detail later.

Because of the very short lifetimes the current flowing through the GaAs collector-base SCR under low bias is due primarily to Shockley-Read-Hall (SRH) recombination through deep traps in the SCR. The SRH recombination rate is given by [11]:

$$U_{SRH} = \frac{n_c' p_c' - n_i^2}{\tau_p\{n_c' + n_i \exp[(E_t - E_i)/kT]\} + \tau_n\{p_c' + n_i \exp[-(E_t - E_i)/kT]\}}, \quad (176)$$

where $n_c'(p_c')$ are the nonequilibrium electron (hole) concentration in the collector, n_i is the intrinsic carrier concentration, E_i is the Fermi level for intrinsic material, E_t is the trap level while τ_n and τ_p are the electron and hole lifetimes, respectively. For $\tau_n = \tau_p$, the recombination rate simplifies to:

$$U_{SRH} = \frac{n_c' p_c' - n_i^2}{\tau_n \{n_c' + p_c' + n_i \cosh[(E_t - E_i)/kT]\}}. \quad (177)$$

This expression is maximized when $E_t = E_i$ and the Fermi energy level crosses the trap level, i.e., $E_f = E_t$. To reach the spatial location where $E_f = E_t$, the carriers must be thermionically emitted from the base and undepleted collector region. Since SRH recombination is a two carrier process, the carrier with the lowest emission current will provide the controlling current.

In the collector-base junction, the holes are emitted from the base while electrons emitted from the undepleted collector. Normally the collector region is non-degenerate so the potential barrier for electron emission into the deep trap is from the undepleted region conduction band to the conduction band energy where $E_f = E_t$. Depicted schematically in Figure 28 is the HBT band diagram, in the region of the collector-base, showing the electron and hole barrier heights for SRH recombination in the collector. For mid-gap trapping levels, the majority of the recombination occurs where the Fermi level (E_f) crosses the intrinsic Fermi level (E_i).

Assuming that $E_t = E_i$, the electron barrier (E_{be}) in the collector is given by:

$$E_{be} = (E_c - E_i) - (E_c - E_f)\big|_{\text{undepleted collector}}, \quad (178)$$

which can be rewritten as:

$$E_{be} = (E_0/2) - (kT/2)\ln(P_v/N_c) - kT\ln(N_c/n_c). \quad (179)$$

Using the values of E_0, N_c, P_v and n_c listed above, we find that $E_{be} = 0.57$ eV.

For a non-degenerate base, the potential barrier for hole emission (E_{bh}) into the

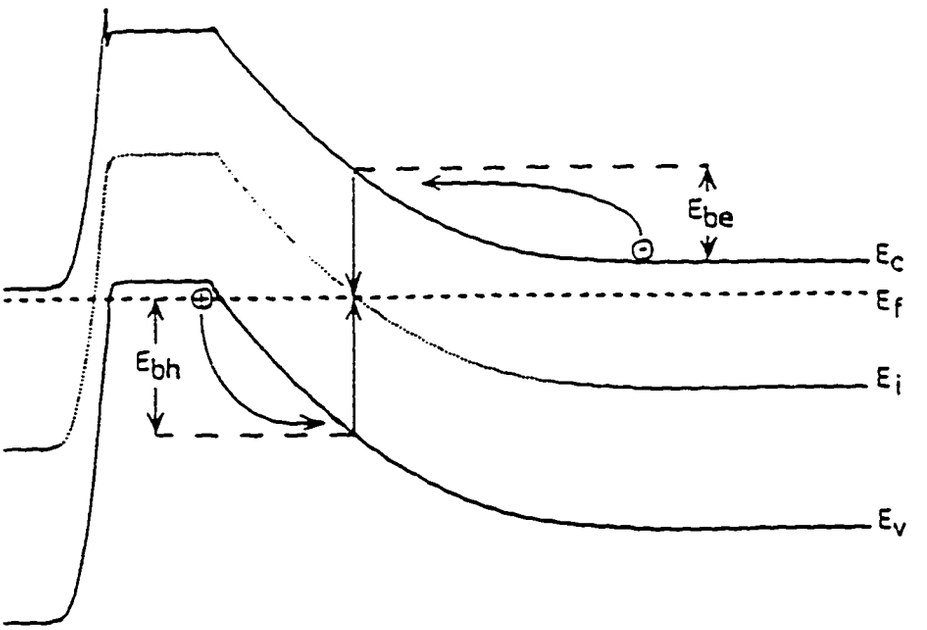

Figure 28. HBT band diagram in the region of the collector-base showing the barrier heights for SRH recombination in the collector.

deep trap is from the base valence band energy to the valence band energy where $E_f = E_t$. This is given by:

$$E_{bh} = qV_{bi} - E_{be}, \tag{180}$$

which yields $E_{bh} = 0.75$ eV. However, because of the heavy doping in the base the Fermi energy level is less than the valence band energy (see Figure 28) and the holes are

emitted from the Fermi level. In our HBT, this correction is 0.03 eV which yields E_{bh} = 0.72 eV. The hole barrier height is sufficiently larger than the electron barrier such that the hole current will limit the recombination process. Therefore, it is the hole barrier that is calculated from τ_1 and the thermionic emission current, i.e., 0.73 eV, which is in excellent agreement with the 0.72 eV value deduced above.

The FKOs from the collector region (see Figure 25) also indicate a barrier height that is considerably less than qV_{bi} (1.32 eV) for the ideal case. From the relation between the field determined from the FKOs (3 x 10^4 V/cm) and the electron barrier height (E_{bc}) [10]:

$$F^2 = (2n_c/\kappa\epsilon_0)(E_{bc} - kT), \tag{181}$$

we find that E_{bc} = 0.46 eV (neglecting any photovoltage effects). This value is in reasonable agreement with that obtained from Eq.(178).

5.3 Electric Field and Photovoltaic Effect

It has been demonstrated that PR can be an effective, nondestructive screening method for HBT structures [12,13]. From an analysis of certain spectral features [FKOs] in the room temperature spectra it has been possible to evaluate the dc electric fields in the GaAlAs emitter (F^{emit}) as well as in the *n*-GaAs collector (F^{coll}) region. The behavior of F^{emit} has been found to have a direct relation to actual device performance; there was a sudden drop in the dc gain when $F^{emit} > 200$ kV/cm. The explanation of this effect is the redistribution of the Be dopant in the *p*-region in these MBE samples. When the redistribution moves the *p-n* junction into the emitter, there is an increase in the electric

field in this region [12].

In this section we report a study of the PR spectra from a GaAs/GaAlAs HBT structure as a function of the intensity of both the probe and pump beams. Our results show that there is a significant photovoltaic contribution to the PR signals. We present new results on the illumination dependence of F^{emit} and F^{coll} deduced from the PR spectra. This experiment demonstrates that (a) doping levels in the emitter/base and collector/base regions can be obtained from the illumination dependence of the observed fields while (b) the fields themselves can be used to evaluate variations in the doping levels.

5.3.1 Experimental Details

The GaAs/GaAlAs HBT sample used in this study was the same as in Section 5.2.1. The pump beams were the 670 nm line of a laser diode (GaAs spectra) or the 543 nm line of a green He-Ne laser (GaAlAs region) modulated at 200 Hz.

5.3.2 Experimental Results

Plotted in Figure 25, in Section 5.2.2, is the PR spectrum at 300 K from the collector and emitter regions of the sample. The intensities of the pump and probe beams were 600 $\mu W/cm^2$ and 100 $\mu W/cm^2$, respectively. The signals occur in the region of the direct band gaps of GaAs and GaAlAs, respectively. Both spectra exhibit pronounced FKOs (see Figure 25). The positions of the N^{th} extrema in the FKOs are given by Eq.(56) [1,2]. With $\mu_{\parallel}$ (in units of the free electron mass) = 0.055 (GaAs) and 0.073

(GaAlAs) we find F = 3.0 x 10^4 V/cm and 1.9 x 10^5 V/cm for the collector and emitter regions, respectively.

It should be noted that for nonuniform fields, such as the ones that exist in *p-n* junctions, it has been shown that the FKOs are a measure of the maximum field in the structure [2].

One of the most important aspects of Figure 25 are the FKOs associated with the emitter region, i.e., GaAlAs band gap. Values of F^{emit}, as deduced from the GaAlAs FKOs, were compared with device parameters of fabricated HBT MBE samples. Below electric field values of about 2 x 10^5 V/cm high current gains were obtained [12]. Shown in Figure 29 is F^{emit} as a function of dc current gain at 1 mA. Note that there is a sudden drop when $F^{emit} > 2 \times 10^5$ V/cm. The explanation of this effect is the redistribution of the Be dopant in the *p*-region in these MBE samples. When the redistribution moves the *p-n* junction into the emitter, there is an increase in the electric field in this region, i.e. the value of F^{emit} becomes greater. The movement of the Be has been verified by secondary ion mass spectroscopy. When the *p-n* junction and the GaAs/GaAlAs HJ are not coincident, carrier recombination occurs, reducing the current and the performance of fabricated HBTs. These observations have made it possible to use PR as a screening technique to eliminate wafers with unwanted characteristics before the costly fabrication step [12].

However, the field deduced from the FKOs may not necessarily represent the actual field in the emitter/base or collector/base regions of the structure. The built-in electric fields can be reduced by the illumination (pump and/or probe beams) due to the

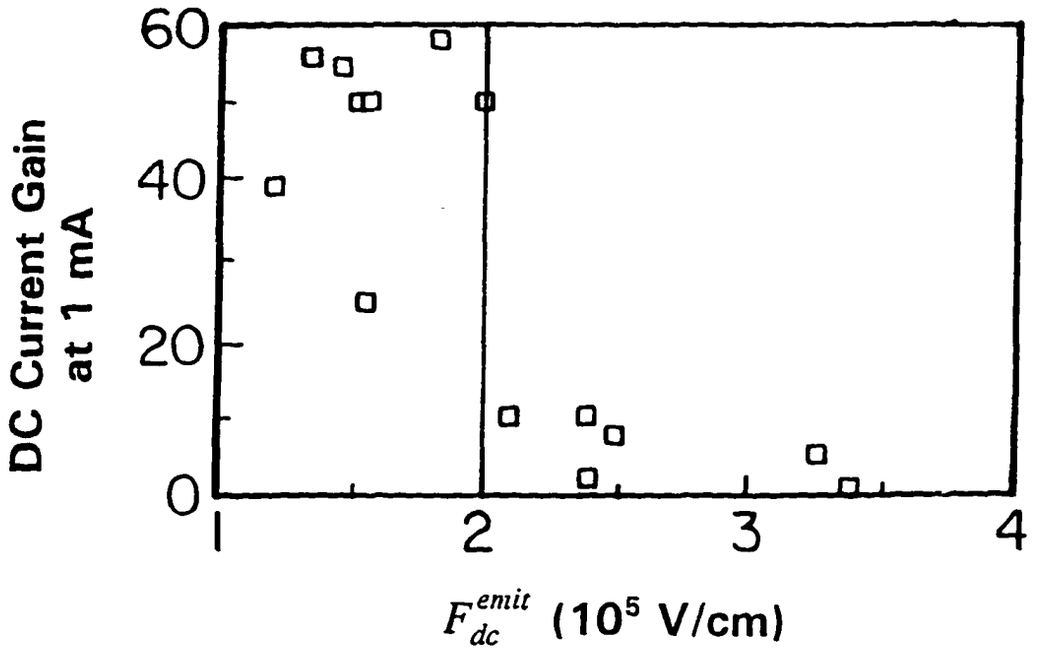

Figure 29. Current gain at 1 mA for GaAs/GaAlAs HBT fabricated devices vs F^{emit} as determined from the GaAlAs FKOs before processing.

photovoltaic effect. In order to compare the fields deduced from the FKOs with the actual fields that exist in the emitter/base and collector/base regions we have performed a computer simulation of the field profiles using a comprehensive, self-consistent model [14] with the structure parameters listed above.

Shown by the solid lines in Figure 30 and Figure 31 are the results of this

calculation for the collector/base and emitter/base regions, respectively. The zero of the spatial ordinate has been taken to be the metallurgical *p-n* homo- or HJ, respectively. Note that both fields are approximately linear over a large spatial region and that the maximum values of the linear portions are about 50 kV/cm and 500 kV/cm, respectively.

To account for this apparent discrepancy in the electric field strengths we also have simulated the field profiles under conditions of illumination. Shown by the dashed lines in Figure 30 and Figure 31 are these results for the collector/base and emitter/base regions, respectively, for a photon flux of $2x10^{14}$ cm^{-2}-sec^{-1}. Note that the maximum fields of the linear portions are now in relatively good agreement with the observed values.

To explore further the influence of the photovoltaic effect we have evaluated the illumination dependence of the fields deduced from the FKOs. Shown by the squares in Figure 32 are the variations in measured values of F^{coll} as a function of probe beam intensity (I_{pr}) in the range 20 -1000 $\mu W/cm^2$ for a pump beam intensity of 150 $\mu W/cm^2$. Note that there is an approximately linear dependence of F^{coll} on the log of I_{pr}.

Using our computer model we also have calculated the intensity dependence of the field. The dashed, solid and dot-dashed lines in Figure 32 show the results of such a simulation for the maximum field in the linear portion of the collector region using the N^{coll}=10, 7.5 and 5.5 (in units of 10^{15} cm^{-3}), respectively, and P^{base} given above. There is very good agreement between experiment and the intended value of N^{coll}. Thus, our experiment and model show that the "slope" of F^{coll} vs log I_{pr} (Figure 32) is sensitive to the doping level. Note that for a given illumination level variations in the doping

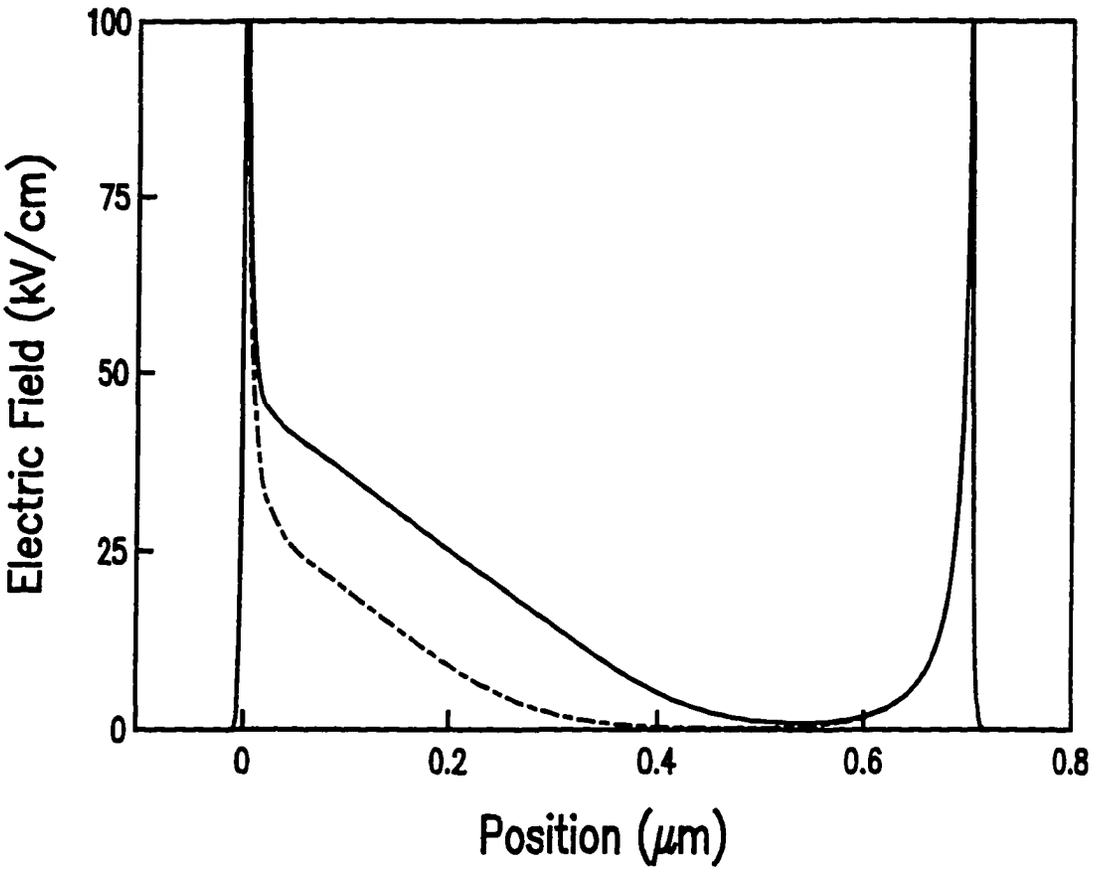

Figure 30. Calculated field profile in the collector/base region in the dark (solid line) and under illumination (dashed line).

concentrations can be evaluated from the changes in F^{coll}.

We have carried out a similar experiment/computer simulation for the emitter/base region. Shown by the solid line in Figure 33 are the values of the "slope" of the illumination dependence of the emitter field, in units of kV/cm-decade (of I_{pr}), as a function of N^{emit} obtained from the computer simulation. The triangle is the experimental determined "slope", yielding $N^{emit} \approx 3.5 \times 10^{17}$ cm^{-3}. This value is in reasonable agreement

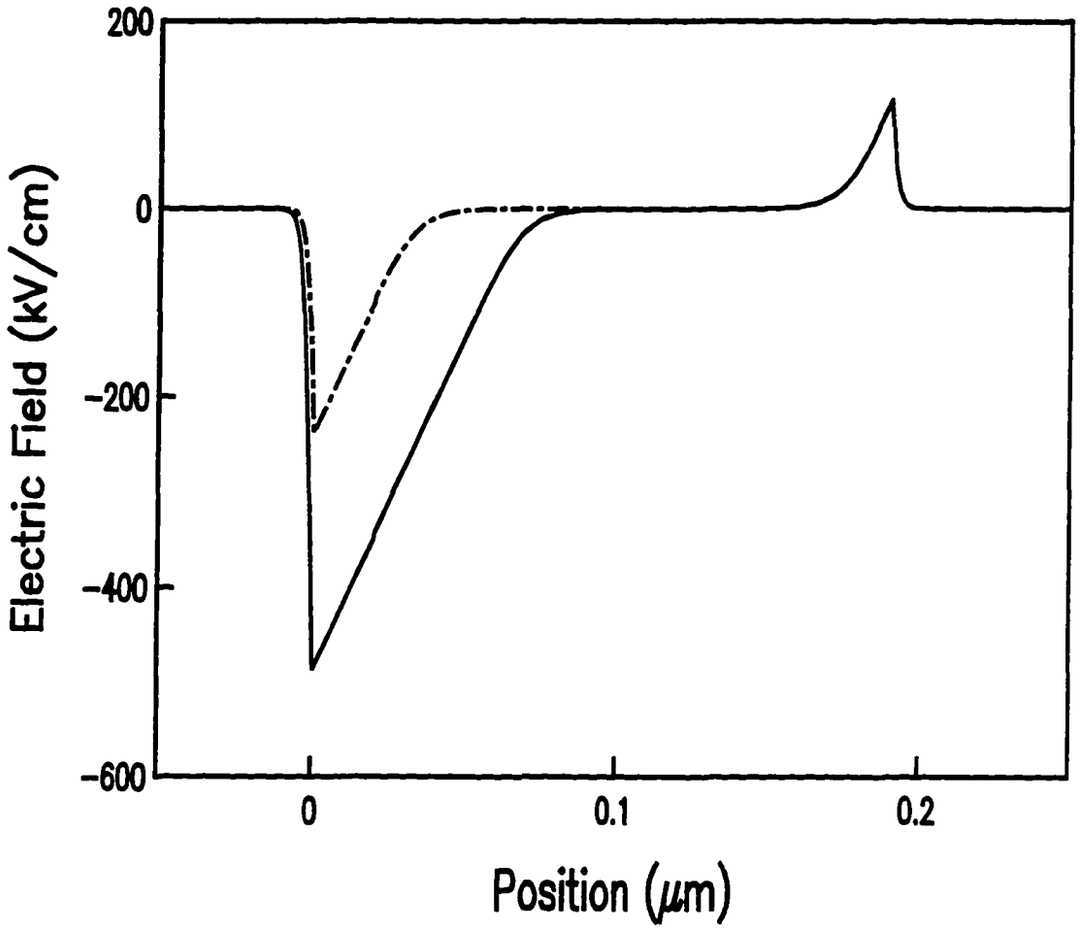

Figure 31. Calculated field profile in the emitter/base region in the dark (solid line) and under illumination (dashed line).

with the intended quantity.

5.3.3 Discussion

The HBT structure contains various hetero- and homojunctions, which govern the distribution of the fields in the device. These fields play a key role in the redistribution of the excess carriers generated by both the probe and pump beams of the PR method.

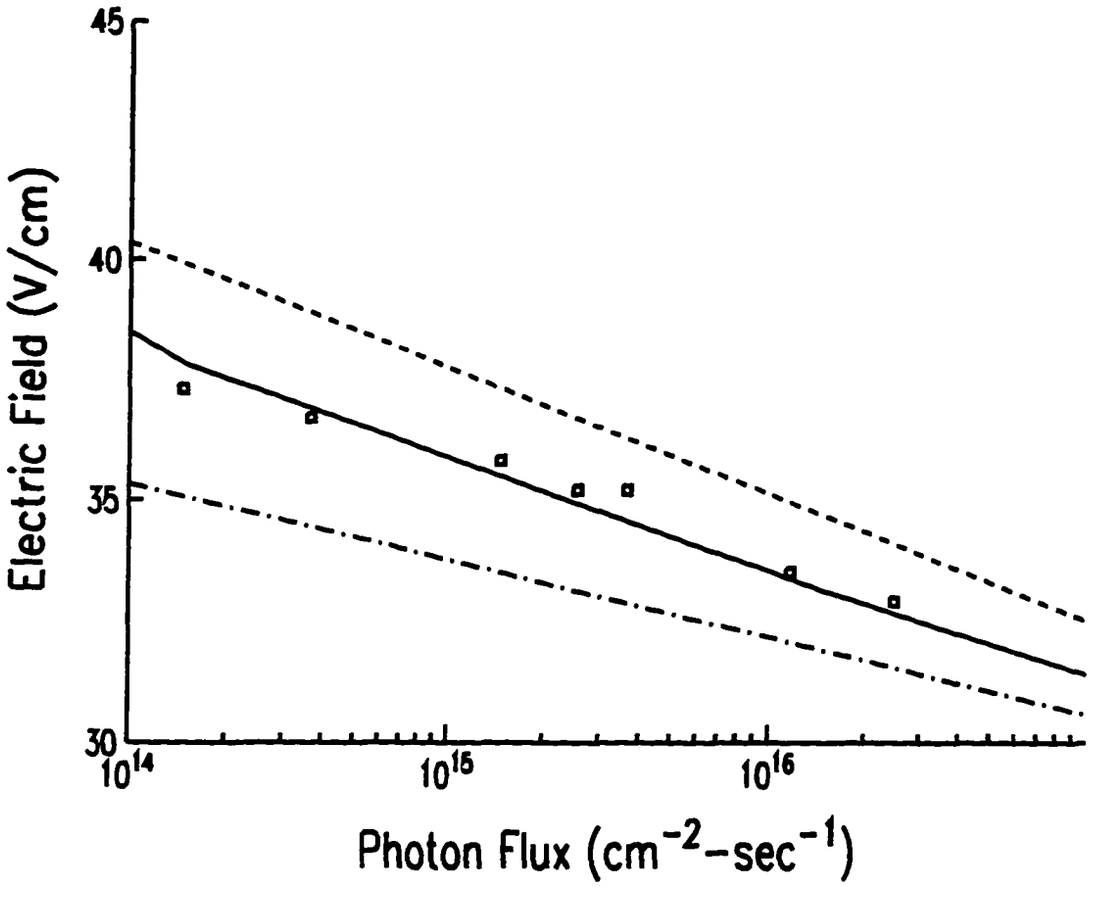

Figure 32. Experimental (square) value and simulation (dashed, solid and dot-dashed lines) of the probe beam intensity dependence of the collector field.

The photogenerated carriers are separated at the junctions and accumulate in the quasi-neutral regions (see Figure 30 and Figure 31) leading to a photo-induced forward bias of the junctions, i.e., photovoltaic effect. Under such conditions the F^{emit} and F^{coll} become illumination-dependent parameters and therefore one cannot simply obtain the "actual" fields in the structure from these quantities alone.

However, as we have demonstrated both experimentally and by computer

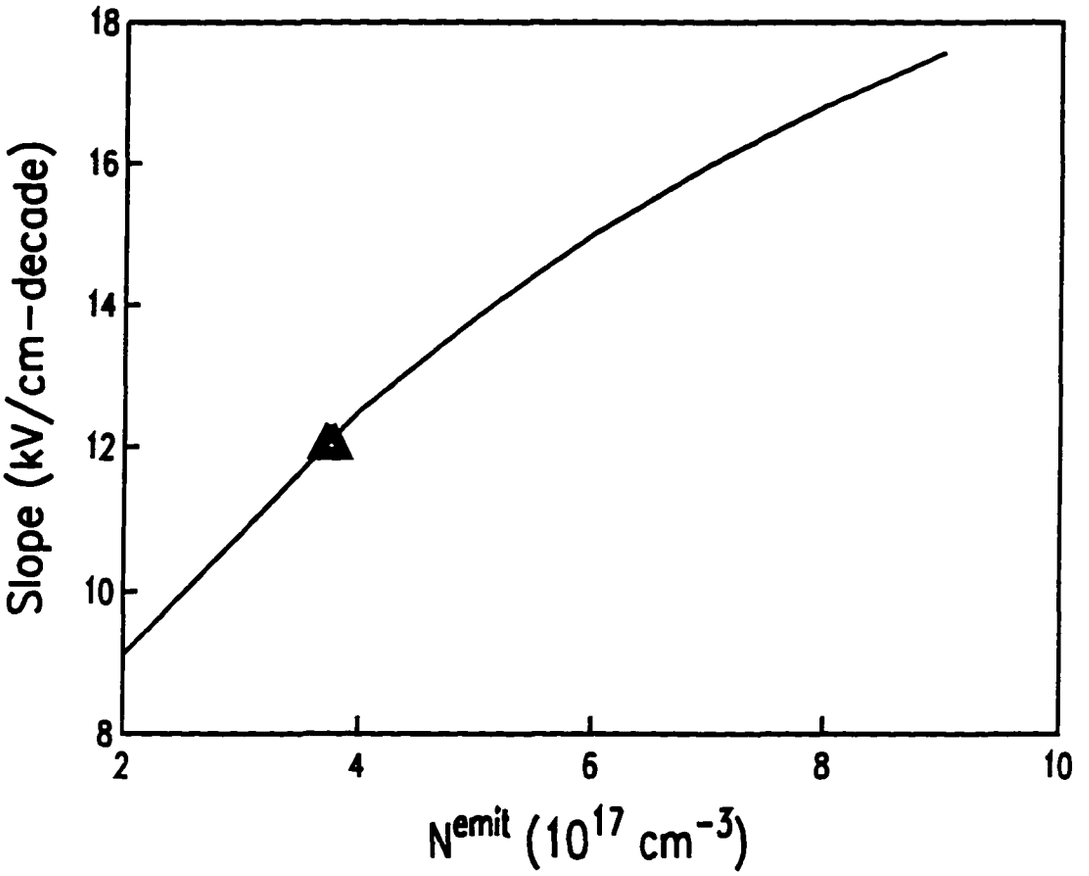

Figure 33. "Slope" of F^{emit} vs I_{pr} as a function of N^{emit}. Simulation-solid line, experiment-triangle.

simulation, the dependence of these fields on illumination intensity is sensitive to the structural parameters of the device. Therefore, the "slope" of F^{emit} or F^{coll} vs the log of intensity can be used to deduce information about doping levels in these regions (see Figure 32 and Figure 33).

Furthermore, for a given light intensity F^{emit} or F^{coll} can still be used to detect changes in the doping profile from sample to sample or over the sample surface. Thus,

the relationship found between F^{emit} and the dc current gain in GaAs/GaAlAs HBTs (see Figure 29) is still valid [12].

Chapter 6. SUMMARY AND CONCLUSIONS

In this thesis we have investigated three types of very important semiconductor microstructures with PR, CER and PzR modulation spectroscopy techniques. The structures used in this work are ZnSe and ZnCdSe layers grown by MBE on GaAs(100) and InP(100) substrates, respectively, pseudomorphic 0.98 μm InGaAs/GaAs/GaAlAs GRINSCH laser structure grown by MBE on a GaAs (001) substrate and GaAs/GaAlAs HBT structure grown by MBE on an undoped liquid encapsulated Czochralski (001) semi-insulating GaAs substrate.

We have demonstrated that modulation spectroscopy is an extremely powerful tool for investigating semiconductor microstructures. Since there are a variety of modulation techniques available, it is possible to choose the one that is most suitable for a particular experiment. The great progress we have made in this thesis work is partial due to our proper choice of modulation techniques for each project.

We have measured the temperature dependence of the direct gaps of ZnSe and $Zn_{0.56}Cd_{0.44}Se$ in the temperature range $25K < T < 400K$ using CER. The quantities that describe the temperature dependence of the energy (including thermal expansion effects) and broadening function of the band gaps were evaluated. Comparison has been made with corresponding parameters of several other II-VI and III-V materials. Our results indicate that there is no clear experimental trend for the ionicity dependence of the Fröhlich interaction and that more work needs to be done in this area.

Using CER at 300K we have characterized the potential profile of a

pseudomorphic 0.98 μm InGaAs/GaAs/GaAlAs GRINSCH laser structure fabricated by MBE. Comparison of the observed transitions from the InGaAs SQW section, including *11H* (which is closely related to the lasing frequency), with an envelope function calculation (including the effects of strain and electric field) made it possible to evaluate the In composition (15.5%) and width (80 Å) of the SQW. These values were in good agreement with the intended parameters. The energy of *11H* can easily be determined to less than $\pm$ 1 nm at 300K. In contrast, photoluminescence, which is an emission process has an intrinsic linewidth of at least 26 meV at 300 K. From the period of the observed FKOs from the graded GaAlAs region we directly evaluated the built-in electric field in the structure.

We have presented the contactless determination of the time constants of the equivalent circuits of both the GaAs collector and GaAlAs emitter portions of a GaAs/GaAlAs HBT structure using the modulation frequency dependence (2 Hz $< \Omega_m <$ 100 kHz) of the in-phase and quadrature photoreflectance signals from these spectrally separated regions. An analysis of the collector time constant has revealed that the recombination mechanism in the collector-base region is dominated by the hole current and is due to midgap trap states. This experiment demonstrates a new area of application for this method for the characterization of these devices.

Finally, we have studied the PR spectra from a GaAs/GaAlAs HBT structure as a function of the intensity of both the probe and pump beams. Our results show that there is a significant photovoltaic contribution to the PR signals. We have presented new results on the illumination dependence of the electric fields deduced from the PR spectra.

We have found that doping levels in the emitter/base and collector/base regions can be obtained from the illumination dependence of the observed fields, while the fields themselves can be used to evaluate variations in the doping levels.

PUBLICATIONS

1. F.H. Pollak, W. Krystek, M. Leibovitch, L. Malikova, M.S. Hybertsen, R. Lum, J.M. Vandenberg and C.L. Reynolds, "Room Temperature, Contactless Electromodulation Investigation of Wafer-Sized Quantum Well Laser Structures", to be published in Vol. **2693** of Proc. SPIE 1996.

2. L. Malikova, W. Krystek, F.H. Pollak, N. Dai, A. Cavus and M.C. Tamargo, "Temperature Dependence of the Direct Gaps of ZnSe and $Zn_{0.56}Cd_{0.44}Se$", Phys. Rev. **B54**, 1819 (1996).

3. W. Krystek, M. Leibovitch, F.H. Pollak, G. Gumbs and T. Konopelski, "Room Temperature Contactless Electromodulation Characterization of a Wafer-Sized InGaAs/GaAs/GaAlAs GRINSCH Laser Structure", Mat. Res. Soc. Symp., Vol. **406**, 241 (1996).

4. F.H. Pollak, W. Krystek, M. Leibovitch, M.L. Gray and W. S. Hobson, "Contactless Electromodulation for the Nondestructive, Room Temperature Analysis of Wafer-Sized Semiconductor Device Structures", IEEE Journal of Selected Topics in Quantum Electronics, Vol. **1**, No. 4, 1002 (1995).

5. F.H. Pollak, W. Krystek, M. Leibovitch, S. Moneger, H. Qiang and D. Yan, "Characterization of Semiconductor Device Structures Using Contactless Electromodulation", Proc. SPIE, **2397**, 92 (1995).

6. W. Krystek, L. Malikova, F.H. Pollak, M.C. Tamargo, N. Dai, L. Zeng and A. Cavus, "Contactless Electroreflectance Study of the Temperature Dependence of the Fundamental Band Gap of ZnSe", Acta Physica Polonica A, **88**, 1013 (1995).

7. F.H. Pollak, W. Krystek, M. Leibovitch, H. Qiang, D.C. Streit, and M. Wojtowicz, "Contactless Room Temperature Analysis of Heterojunction Bipolar Transistor Wafer Structures Using Photoreflectance", *Proceedings of the International Workshop on Semiconductor Characterization*, ed. W.M. Bullis, D.G. Seiler and A.C. Diebold (American Institute of Physics, Woodbury, 1995), p. 669.

8. F.H. Pollak, H. Qiang, D. Yan, W. Krystek and S. Moneger, "Nondestructive, Room Temperature Analysis/Qualification of Wafer-Sized Semiconductor Device Structures Using Contactless Electromodulation Spectroscopy", Solid-State Electronics, **38**, 1121 (1995).

9. W. Krystek, H. Qiang, F.H. Pollak, "Contactless HBT Equivalent Circuit Analysis using the Modulation Frequency Dependence of Photoreflectance", Inst.

Phys. Conf. Ser. **141**, 651 (1994).

10. F.H. Pollak, H. Qiang, D. Yan, Y. Yin, W. Krystek and S. Moneger, "Contactless Electromodulation for the Characterization of Semiconductor Device Structures", *Proceedings of the ECS Symposium on Diagnostic Techniques for Semiconductor Materials and Devices*, (Electrochemical Society, Pennington, 1995) ed. D. Schroder, J. Benton and J. Rai-Choudhury, ECS Proc. **94-33**, p. 228.

11. F.H. Pollak, H. Qiang, D. Yan, Y. Yin and W. Krystek, "Analyzing Semiconductor Devices Using Modulation Spectroscopy", Journal of Metals, **46**, 55 (1994).

12. M.C. Tamargo, N. Dai, A. Cavus, R. Dzakpasu, W. Krystek, F.H. Pollak, F. Semendy, N. Bambha, P. Boyd, D.M. Hwang, and C.Y. Chen, "Growth of Wide Bandgap II-VI Alloys on InP Substrates by Molecular Beam Epitaxy", Proc. SPIE, **2346**, 70 (1994).

BIBLIOGRAPHY

Chapter 2:

1. F.H. Pollak, *Proc. Soc. Photo-Optical Instrum. Engineers* (SPIE, Bellingham, 1981) **276**, p. 142.

2. M. Cardona, *Modulation Spectroscopy* (Academic, New York, 1969) and references therein.

3. M. Cardona, *Festkorperprobleme X* (Pergamon, Oxford, 1970) p. 125.

4. Y. Hamakawa and T. Nishino, Optical Properties of Solids: New Developments ed. B.O. Seraphin (North-Holland, Amsterdam, 1976) p. 255.

5. D.E. Aspnes, in *Handbook on Semiconductors*, Vol. **2**, ed. M. Balkanski (North-Holland, New York, 1980), p. 109.

6. E.E. Mendez, L.L. Chang, G. Landgren, R. Ludeke, L. Esaki and F.H. Pollak, Phys. Rev. Lett. **46**, 1230 (1981).

7. M. Erman, J. B. Theetan, P. Frijlink, S. Gaillard, F. J. Hia and C. Alibert, J. Appl. Phys. **56**, 3241 (1984).

8. C. Alibert, S. Gaillard, J.A. Brum, G. Bastard, P. Frijlink and M. Erman, Solid State Comm. **53**, 457 (1985).

9. O.J. Glembocki, B.V. Shanabrook, N. Bottka, W. T. Beard and J. Comas, *Proc. Soc. Photo-Optical Instrum. Engineers* (SPIE, Bellingham, 1985) **524**, p. 86.

10. O.J. Glembocki, B.V. Shanabrook, N. Bottka, W.T. Beard and J. Comas, Appl. Phys. Lett. **46**, 970 (1985).

11. F. Bassani, G. Pastori-Parravicini, *Electronic States and Optical Transitions in Solids* (Pergamon Press, New York, 1975).

12. D.E. Aspnes and N. Bottka, 1972, in *Semiconductors and Semimetals*, Vol. **9**, ed. R.L. Willardson and A.C. Beer (Academic, New York, 1972), p. 457.

13. F.H. Aymerich, F. Handler, D.F. Blossey, Phys. Rev. **166**, 921 (1968).

14. D.E. Aspnes, Phys. Rev. **153**, 927 (1967).

15. N. Bottka, D.K. Gaskill, R.S. Sillmon, R. Henry and R. Glosser, J. Electron. Materials **17**, 161 (1988).

16. D.E. Aspnes, Phys. Rev. **B10**, 4228 (1974).

17. H. Shen and M. Dutta, J. Appl. Phys. **78**, 2151 (1995).

18. H. Shen and F.H. Pollak, Phys. Rev. **B42**, 7097 (1990).

19. D.E. Aspnes and A.A. Studna, Phys. Rev. **B7**, 4605 (1973).

20. F.H. Pollak, *Encyclopedia of Materials Characterization: Surfaces, Interfaces and Thin Films* , ed. C. Evans, R. Brundle and S. Wilson (Butterworth-Heinemann, Boston, 1992) p. 385.

21. B.V. Shanabrook. and O.J. Glembocki, *Proc. 18th Int. Conf. Phys. Semicond.*, Stockholm, ed. O. Engstrom (World Scientific, Singapore, 1987) p. 565.

22. B.V. Shanabrook, O.J. Glembocki and W.T. Beard, Phys. Rev. **B35**, 2540 (1987).

23. R. Enderlein, D.-S. Jiang and Y. S. Tang, Phys. Stat. Solidi **145(b)**, 167 (1988).

24. F.H. Pollak and O.J. Glembocki, *Proc. Soc. Photo-Optical Instrum. Engineers*, ed. O.J. Glembocki, F.H. Pollak, and F. Ponce (SPIE, Bellingham, 1988), **946**, p. 2.

25. D.S. Jiang, Y.S. Tang, J.-B. Xia and R. Enderlein, Superlattices and Microstructures **6**, 387 (1989).

26. R. Enderlein, in *Proc. Soc. Photo-Optical Instrum. Engineers* (SPIE, Bellingham, 1990) **1286**, p. 188.

27. Y.S. Tang, J. Appl. Phys. **69**, 8298 (1991).

28. F.H. Pollak and H. Shen, Materials Science and Engineering, **R10**, 275 (1993).

29. O.J. Glembocki and B.V. Shanabrook, in *Semiconductors and Semimetals*, Vol. **36**, ed. D.G. Seiler and C.L. Littler (Academic, New York, 1992) p. 221 and references therein.

30. Y.S. Huang, H. Qiang, F.H. Pollak, J. Lee and B. Elman, J. Appl. Phys. **70**, 3808 (1991).

31. S.Y. Toyozawa, Prog. Theor. Phys. **20**, 53 (1958).

32. S.F. Edwards and Y.B. Gulyaev, Proc. Phys. Soc. **83**, 495 (1964).

33. T. Lukes and K. T.S. Somaratna, J. Phys. **C3**, 2044 (1970).

34. J.W. Garland, H. Abad, M. Viccaro and P. M. Raccah, Appl. Phys. Lett. **52**, 1176 (1988).

35. O.J. Glembocki and B.V. Shanabrook, Superlattices and Microstructures **3**, 235 (1987).

36. O.J. Glembocki, in *Proc. Soc. Photo-Optical Instrum. Engineers* (SPIE, Bellingham, 1990) **1286**, p. 2 and references therein.

37. B.V. Shanabrook, O.J. Glembocki and W.T. Beard, Phys. Rev. **B35**, 2540 (1987).

38. O.J. Glembocki, Mat. Res. Soc. Symp. Proc. **160**, 631 (1990).

39. X.L. Zheng, D. Heiman, B. Lax, F.A. Chambers and K.A. Stair, Appl. Phys. Lett. **52**, 984 (1988).

40. X. Yin and F.H. Pollak, Appl. Phys. Lett. **59**, 2305 (1991).

41. X. Yin, X. Guo, F.H. Pollak, G.D. Pettit, J.M. Woodall, T.P. Chin and C. W. Tu, Appl. Phys. Lett. **60**, 1336 (1992).

42. X. Yin, X. Guo, F.H. Pollak, G.D. Pettit, J.M. Woodall, and E-H. Cirlin *Proc. Soc. Photo-Optical Instrum. Engineers* (SPIE, Bellingham, 1992) **1678**, p. 168.

43. S.L. Mioc, P.M. Raccah and J.W. Garland, *Proc. Soc.Photo-Optical Instrum. Engineers* (SPIE, Bellingham, 1992) **1678**, p. 296.

44. H. Shen, P. Parayanthal, Y.F. Liu and F.H. Pollak, Rev. Sci. Instrum. **58**, 1429 (1987).

45. H. Shen, F.H. Pollak, J.M. Woodall and R.N. Sacks, J. Electron. Materials **19**, 283 (1990).

46. W.M. Theis, G.D. Sanders, C.E. Leak, K.K. Bajaj and H. Morkoc, Phys. Rev. **B37**, 3042 (1988).

47. O.J. Glembocki and B.V. Shanabrook, *Proc. Soc. Photo-Optical Instrum.*

Engineers (SPIE, Bellingham, 1987) **794**, p. 74.

48. H. Shen and M. Dutta, Appl. Phys. Lett. **57**, 587 (1990).

49. M. Sydor, A. Badakhshan, James R. Engholm and D.A. Dale, Appl. Phys. Lett. **58**, 948 (1991).

50. D. Yan, H. Qiang, and F.H. Pollak, Rev. Sci. Instrum. **65**, 6 (1994).

Chapter 3:

1. M.A. Haase, J. Qiu, J.M. Depuydt, and H. Cheng, Appl. Phys. Lett. **59**, 1272 (1991); H. Jeon, J. Ding, W. Xie, M. Kobayashi, R.L. Gunshor and A.V. Nurmikko, Appl. Phys. Lett. **59**, 3619 (1991); G.F. Nuemark, R.M. Park and J.M. DePuydt, Physics Today **47**, (6), 26 (1994).

2. M.C. Tamargo, M.J.S.P. Brasil, R.E. Nahory, R.J. Martin, A.L. Weaver and H.L. Gilchrist, Semicond. Sci. Technol. **6**, A8 (1991).

3. P. Lautenschlager, M. Garriga, S. Logothetidis and M. Cardona, Phys. Rev. **B35**, 9174 (1987).

4. S. Gopalan, P. Lautenschlager, L. Vina and M. Cardona, Phys. Rev. **B36**, 4821 (1987).

5. C.K. Kim, P. Lautenschlager and M. Cardona, Solid State Comm. **59**, 797 (1986); S. Zollner, S. Gopalan and M. Cardona, Solid State Comm. **77**, 485 (1991).

6. Z. Hang, D. Yan, F.H. Pollak, G.D. Pettit and J.M. Woodall, Phys. Rev. **B44**, 10546 (1991).

7. Y.P. Varshni, Physica (Utrecht) **34**, 149 (1967).

8. P.B. Allen and M. Cardona, Phys. Rev. **B23**, 1495 (1981).

9. P.B. Allen and M. Cardona, Phys. Rev. **B27**, 4760 (1983).

10. P. Lautenschlager, P.B. Allen and M. Cardona, Phys. Rev. **B31**, 2163 (1985).

11. P. Lautenschlager, P.B. Allen and M. Cardona, Phys. Rev. **B33**, 5501 (1986).

12. S. Gopalan, P. Lautenschlager and M. Cardona, Phys. Rev. **B35**, 2163 (1987).

13. P.B. Allen and V. Heine, J. Phys. **C9**, 2305 (1976).

14. E. Antoncik, Czeck. J. Phys. **5**, 449 (1955).

15. H.Y. Fan, Phys. Rev. **82**, 900 (1951).

16. M.L. Cohen, Phys. Rev. **128**, 131 (1962).

17. P. Lautenschlager, M. Garriga, S. Logothetidis and M. Cardona, Phys. Rev. **B36**, 4813 (1987).

18. S. Rudin, T.L. Reinecke and B. Segall, Phys. Rev. **B42**, 11218 (1990).

19. F.H. Pollak and H. Shen, Materials Science and Engineering **R10**, 275 (1993).

20. P. Ram, J. Freeouf, F.H. Pollak, M.C. Tamargo and N. Dai, private communication.

21. R. Dahmani, L. Salamanca-Riba, N.V. Nguyen, D. Chandler-Horowitz and B.T. Jonker, J. Appl. Phys. **76**, 514 (1994).

22. W. Krystek, L. Malikova and F.H. Pollak, M. C. Tamargo, N. Dai, L. Zeng and A. Cavus, Acta Physica Polonica A, **88**, 1013 (1995).

23. *Semiconductors, Intrinsic Properties of Group IV Elements and III-V, II-VI and I-VII Compounds*, ed. O. Madelung, M. Schulz, Landolt-Börnstein, New Series, Group III, Vol. **22**, Pt. a (Springer, New York, 1987).

24. *Semiconductors*, ed. O. Madelung, M. Schulz and H. Weiss, Landolt-Börnstein, New Series, Group III, Vol. **17** (Springer, New York, 1982).

25. S. Logothetidis, M. Cardona, P. Lautenschlager and M. Garriga, Phys. Rev. **B34**, 2458 (1986).

26. Z. Hang, H. Shen and F.H. Pollak, Solid State Comm. **73**, 15 (1990).

27. Y. Yin, D. Yan and F.H. Pollak, M.S. Hybertsen, J.M. Vandenberg and J.C. Bean, Phys. Rev. **B52**, 8951 (1995).

28. H. Shen, S.H. Pan, Z. Hang, J. Leng, F.H. Pollak, J.M. Woodall and R.N. Sacks, Appl. Phys. Lett. **53**, 1080 (1988).

29. N. T. Pelekanos, J. Ding, M. Hagerott, and A. V. Nurmikko, H. Luo, N. Samarth, and J. K. Furdyna, Phys. Rev. **B45**, 6037 (1992).

30. H. Qiang, F.H. Pollak, C.M. Sotomayor-Torres, W. Leitch, A.H. Kean, M. Stroscio, G.J. Iafrate and K.W. Kim, Appl. Phys. Lett. **61**, 1411 (1992).

31. V.L. Alperovitch, V.M. Zaletin, A.F. Kravechenko and A.S. Terekhov, Phys. Stat. Sol (b) **77**, 465 (1976).

32. D. Gammon, S. Rudin, T.L. Reinecke, D.S. Katzer and C.S. Kyono, Phys. Rev. **B51**, 16785 (1995).

33. A. Manoogian and J. C. Woolley, Can. J. Phys. **62**, 285 (1984).

Chapter 4:

1. K. Satzke, H.G. Vestner, G. Weiser, L. Goldstein and A. Perales, J. Appl. Phys. **69**, 7703 (1991).

2. V.T. Boccio and F.H. Pollak, private communication.

3. S. Moneger, H. Qiang, F.H. Pollak, D.L. Mathine, R. Droopad and G.N. Maracas, Solid State Electronics **39**, 871 (1996).

4. P.D. Berger, C. Bru, T. Benyattou, A Chenevas-Paule and P. Grosse, Proc. SPIE **2397**, 726 (1995).

5. P.M. Amirtharaj, Mat. Res. Soc. Symp., Vol. **406**, 229 (1996).

6. D. Chandler-Horowitz, D.W. Berning, J.G. Pellegrino, J.H. Burnett, P. M. Amirtharaj, D.P. Bour and D.W. Treat, *Proceedings of the International Workshop on Semiconductor Characterization*, ed. W.M. Bullis, D.G. Seiler and A.C. Diebold (American Institute of Physics, Woodbury, 1995), p. 639.

7. W. Krystek, M. Leibovitch, F.H. Pollak, M.L. Gray and W.S. Hobson, IEEE Journal of Selected Topics in Quantum Electronics, Vol. **1**, No. 4, 1002 (1995).

8. J.M. Kuo, Y.K. Chen, M.C. Wu and M.A. Chin, Appl. Phys. Lett. **59**, 2781 (1991).

9. G. Gumbs and D. Huang, Phys. Rev. **B50**, 15148 (1994); G. Gumbs, D. Huang and J.P. Loehr, Phys. Rev. **B51**, 4321 (1995); D. Huang, G. Gumbs and M.O. Manasreh, Phys. Rev **B52**, 14126 (1995); also private communication with G. Gumbs.

10. G. Bastard, Phys. Rev. **B25**, 7584 (1982).

11. C. Weisbuch, *Semiconductors and Semimetals*, Vol. **24**, ed. R. Dingle (Academic, New York, 1987), p. 1.

12 W. Kohn, in *Solid State Physics: Advances in Research and Applications*, Vol. **5**, ed. F. Seitz and D. Turnbull (Academic, New York, 1957), p. 257.

13 M. Altarelli, in *Heterojunctions and Semiconductor Superlattices*, G. Allan, G. Bastard, N. Boccara, M. Lannoo, M. Voos (Springer, Berlin, 1986) p. 12.

14. W.A. Harrison, Phys. Rev. **123**, 85 (1961).

15. D.J. Ben-Daniel and C.B. Duke, Phys. Rev. **152**, 683 (1966).

16. G.L. Bir and G.E. Pikus, in *Symmetry and Strain-Induced Effects in Semiconductors* (John Wiley, New York, 1974).

17. F.H. Pollak, Surface Science **B36**, 863 (1973).

18. F.H. Pollak in *Semiconductors and Semimetals*, Vol. **32**, ed. T.P. Pearsall (Academic, New York, 1990) p. 17.

19. J.C. Hensel and G. Feher, Phys Rev **129**, 1041 (1963).

20. W.H. Kleiner and L. M. Roth, Phys. Rev. Lett. **2**, 334 (1959).

21. E.O. Kane, in *Semiconductors and Semimetals*, Vol. **1**, ed. R. K. Willardson and A. C. Beer (Academic, New York, 1966), p. 75.

22. *Semiconductors*, ed. O. Madelung, M. Schulz and H. Weiss, Landolt-Börnstein, New Series, Group III, Vol. **17** (Springer, New York, 1982).

23. L. Laude., F.H. Pollak and M. Cardona, Phys. Rev. **B3**, 2623 (1971).

24. J.Y. Marzin and J.M. Gérard, *Semiconductors and Semimetals*, Vol. **32**, ed. T.P. Pearsall (Academic, New York, 1990), p. 55.

25. R. People and S.A. Jackson, in *Semiconductors and Semimetals*, Vol. **32**, ed. T.P. Pearsall (Academic Press, New York, 1990), p. 119.

26. G.C. Osbourn, in Proc. Int. Conf. Metastable and Modulated Semiconductor Structures, Pasadena, 1982, ed. F. J. Grunthaner and A. Madhukar, J. Vac. Sci. Technol., Vol. **B1(2)**, 379 (1983).

27. P. Voisin, in *Two-Dimensional Systems, Heterostructures and Superlattices*, ed.

G. Bauer, F. Kuchar, and H. Heinrich (Springer-Verlag, Berlin, 1984), *Springer Series in Solid State Sciences*, Vol. **53**, p. 192.

28. G.C. Osbourn, Superlattices and Microstructures, **1**, 223 (1985).

29. J.Y. Marzin, in *Proc. 85 Les Houches Winterschool Semiconductor Superlattices and Heterojunctions*, ed. G.Allan, G. Bastard, N. Boccara, M. Lannoo and M. Voos (Springer-Verlag, Berlin, 1985), 161.

30. J. Singh, *Physics of Semiconductors and Their Heterostructures* (McGraw-Hill, New York, 1993).

31. C. Weisbuch and B. Vinter, in *Quantum Semiconductor Structures: Fundamentals and Applications* (Academic Press, New York, 1991).

32. F.H. Pollak and H. Shen, Materials Science and Engineering, **R10**, 275 (1993) and references therein.

33. F.H. Pollak in *Properties of Aluminium Gallium Arsenide*, ed. S. Adachi (INSPEC, London, 1993), p. 53.

34. O.J. Glembocki and B. V. Shanabrook, *Semiconductors and Semimetals*, Vol. **36**, ed. D.G. Seiler and C.L. Littler (Academic Press, New York, 1992), p. 222 and references therein.

35. F.H. Pollak in *Handbook on Semiconductors*, Vol. **2**, ed. M. Balkanski (North Holland, Amsterdam, 1994), p. 527 and references therein.

36. G. Bastard and J.A. Brum, IEEE J. Quantum Electron., **QE-22**, 1625 (1986).

37. S.H. Pan, H. Shen, Z. Hang, F.H. Pollak, W. Zhuang, Q. Xu, A.P. Roth, R. Masut, C. LeCelle, and D. Morris, Phys. Rev., **B38**, 3375 (1988).

38. S. Adachi in *Properties of Aluminium Gallium Arsenide*, ed. S. Adachi (INSPEC, London, 1993), p. 58.

39. M. Leibovitch, L. Kronik and Y. Shapira, Phys. Rev., **B50**, 1739 (1994).

Chapter 5:

1. See, for example, O.J. Glembocki and B.V. Shanabrook *Semiconductors and Semimetals*, Vol. **36**, ed. D.G. Seiler and C.L. Littler (Academic, New York, 1992), p. 222 and references therein.

2. See, for example, F.H. Pollak and H. Shen, Materials Science and Engineering, **R10,** 275 (1993) and references therein.

3. H. Qiang, F.H. Pollak, Y.S. Tang, P.D.Wang, and C.M. Sotomayor-Torres, Appl. Phys. Lett. **64**, 2830 (1994).

4. See, for example, F.H. Pollak, H. Qiang, D. Yan, Y. Yin and V.T. Boccio 1993 Photonics Spectra Magazine, **Vol. 27**, Issue 8, 78 (1993) and references therein; H. Qiang, D. Yan, Y. Yin and F.H. Pollak, Asia-Pacific Engineering Journal, Part A: Electrical Engineering, **3**, 167 (1993).

5. R.P. Silberstein, J.K. Lyden, M. Tomkiewicz and F.H. Pollak, J. Vac. Sci. Technol. **19,** 406 (1981).

6. H.K. Lipsanen and V.M. Airaksinen, Appl. Phys. Lett. **63**, 2863 (1993).

7. V.L. Alperovich, A.S. Jaroshevich, E.H. Scheibler and A.S. Terehov, Solid State Electronics **37,** 657 (1994).

8. H. Shen, M. Dutta, R. Lux, W. Buchwald, L. Fotiadis and R.N. Sacks, Appl. Phys. Lett. **59,** 321 (1991).

9. H. Shen, F.H. Pollak, J.M. Woodall and R.N. Sacks, J. Electron. Materials **19**, 283 (1990).

10. See, for example, S.M. Sze, *Physics of Semiconductor Devices*, 2nd edition (New York; Wiley, 1981).

11. See, for example, S. Tawari, *Compound Semiconductor Device Physics*, (New York; Academic, 1992).

12. X. Yin, F.H. Pollak, L. Pawlowicz, T.J. O'Neill and M. Hafizi, Appl. Phys. Lett. **56**, 1278 (1990); also, *Proc. Soc. Photo-Optical Instrum. Engineers* (SPIE, Bellingham, 1990), **1286**, p. 404.

13. N. Bottka, D.K Gaskill, P.D. Wright, R.W. Kaliski, and D.A. Williams, J. Cryst. Growth **107**, 893 (1991).

14. M. Leibovitch, L. Kronik and Y. Shapira, Phys. Rev. **B50**, 1739 (1994).